Quantitative Scanning Transmission Electron Microscopy Characterisation of Size-Selected Gold Clusters

by

HE DONG SHENG

何 东 升

A thesis submitted to

The University of Birmingham

for the degree of

DOCTOR OF PHILOSOPHY

Nanoscale Physics Research Laboratory

School of Physics and Astronomy

The University of Birmingham

November 2013

Acknowledgements

I would like to thank my PhD supervisor, Dr. Ziyou Li, for giving me such a good opportunity to work on the project at the beginning and always being patient and enthusiastic with this project. The successful completion of this thesis is supported by her continuous encouragement and suggestions.

This work cannot be accomplished without collaborating with other colleagues. I appreciate Dr. David Pearmain and Dr. Zhiwei Wang helping with the microscope, Dr. Feng Yin and Prof. Richard Palmer providing me the size selected Au_{887} clusters, Dr. Andrew Logsdail and Prof. Roy Johnston supplying me the atomic coordinates. Some part of this work is inspired by discussions with Prof. Jun Yuan. In addition, the collaborations with Dr. Yisong Han, Dr. John Fennell and Dr. Sarah Horswell are also enjoyable.

I would like to give my special thanks to Dr. Ruth Chantry for her patient, careful and suggestive proof reading of the draft thesis.

I appreciate all the NPRLers and other friends for making my PhD experience great.

Finally I would like to thank my family members and my girlfriend Jingyi Tan, for all their understanding, support and encouragement.

I acknowledge the University of Birmingham and the China Scholarship Council for the studentships throughout my PhD study.

Abstract

This thesis presents a systematic study on the three-dimensional atomic structures of the size-selected gold (Au) using aberration-corrected scanning transmission electron microscopy (STEM), fitted with a high angle annular dark field (HAADF) detector. The work involves experimental quantification of the microscope, HAADF-STEM image modeling and cluster structure identification. The study explores the cluster structure distribution as a function of experimental conditions and investigates their structural stability by electron beam irradiation.

The Au clusters studied were produced by inert gas aggregation, size-selected by a lateral time-of-flight filter and soft-landed on thin amorphous carbon films. A quantitative image analysis methodology has been developed for rapid cluster structure identification, which involves direct comparison of atomic-resolved experimental images with simulated images. Applying the method to over two thousand individually imaged Au_{887} clusters (each containing nominal 887 gold atoms) revealed a distribution of structural isomers including icosahedron, decahedron and FCC structures. It was found that the isomer distribution depended critically on the cluster formation conditions. A quick condensation condition led clusters with icosahedral structure, while the slow condensation was favoured by clusters with FCC structure. In addition, the stability of Au_{887} clusters under the electron beam irradiation was investigated by following electron beam induced structural transformation in situ. The transformation sequence was found to be dominated by icosahedron to decahedron to FCC structure. The results provide insights to the understanding of cluster growth mechanism and dynamic behaviour at atomic scale, enabling the ability to control the three dimensional atomic structures of clusters.

Contents

Abbrevation

ADF Annular Dark Field
BF Bright Field
CCD Charge Coupled Device
CBED Convergent Beam Electron Diffraction
Dh Decahedron
DF Dark Field
EAM Embeded Atom Method
EDX Enegy Dispersive X-ray
EELS Electron Energy Loss Spectroscopy
FCC Face Centred Cubic
FEG Field Emission Gun
FFT Fast Fourier Transform
HCP Hexagonal Close Packed
HAADF High Angle Annular Dark Filed
Ih Icosahedron
MTP Multiply Twinned Particle
PMT Photomultiplier Tube
SEM Scanning Electron Microscopy
STEM Scanning Transmission Electron Microscope
TDS Thermal Diffuse Scattering
TEM Transmission Electron Microscope

Chapter 1

Introduction

Nanoclusters are small aggregations of atoms, usually ranging from 1-10 nm in size. The properties of nanoclusters can be very different from their bulk counterpart and are usually size-dependent. For example, gold is well known as an inert metal with face centred cubic (FCC) crystalline structure. However, nano-gold can be a very good catalyst [1, 2, 3, 4] and they can exhibit five-fold structures such as icosahedron (Ih) or decahedron (Dh) [5]. In addition, when its size is scaled down, gold shows very different dynamic behaviours, such as decreased melting temperature [6], increased instability [7]. In this size regime, every atom counts, hence knowing how atoms are arranged within the clusters becomes increasingly important to understand their properties and is crucial in order to exploit fully their potential applications in fields such as catalysis, optics or drug delivery [8].

However, identification of the atomic structure of ultrasmall clusters in three-dimension is chanlleging. One of the reasons is that ultrasmall clusters are intrinsically unstable and tend to interact with any incident probes used to examine them, limiting the investiga-

tion time duration and the electron beam dose. Benefiting from recent advance in the development of aberration corrected scanning transmission electron microscopy (STEM), single shot imaging of nanoclusters with atomic resolution becomes feasible [9]. The STEM technique involves fast scanning across the cluster with a focused electron beam and collects the scattered electrons to form an image. The contrast of images depends on not only atomic column height but also the atomic number of the elements [10]. The former allows three-dimensional information of nanoclusters to be extracted, while the latter makes the techniques particularly suitable for studying small heavy metal clusters such as gold on light element support such as carbon.

In this thesis, a detailed report is presented on a systematic study of atomic structure of size-selected gold clusters formed through inert gas condensation in gas phase and deposited on carbon support. The clusters are imaged using a current generation aberration-corrected STEM located in Nanoscale Physics Research Laboratory, University of Birmingham. The thesis is organized as follows:

Chapter 2 starts by introducing general background of cluster production methods and cluster structures. This is followed by a critical review of the literature on several topics to be addressed in this research including cluster formation mechanisms and energetics of atomic structures of nanoclusters, with emphasis on the gold cluster structures.

Chapter 3 introduces in depth the basic principle of the STEM technique, which is the main experimental technique used in this work. First, the interaction between electron beam and solid is discussed. This is followed by introducing the main electron optics components in STEM and image formation principles.

The main results are presented in five chapters. In Chapter 4 and 5, the methodology of single-shot imaging has been developed. Chapter 4 illustrates the experimental steps to quantify the microscope JEOL 2100, with the emphasis on the annular dark field detector. Chapter 5 introduces the mathematical modelling of high angle annular dark field (HAADF)-STEM images. It has two aspects: extracting the three dimensional information from HAADF-STEM and simulating the kinematic HAADF-STEM image with known atomic coordinates.

By comparing the experimental image and simulated image, the atomic structure of Au_{887} clusters can be identified. Chapter 6 catergories Au_{887} clusters into different structures: Ih, Dh and FCC. This allows the study of structure distribution as a function of experimental conditions, which is shown in Chapter 7, and the stability of clusters, which is studied by the eletcron beam irradiation and shown in Chapter 8. A brief summary follows in Chapter 9.

Chapter 2

Literature review

2.1 Introduction

Atomic structures of nanocluster have been studied from both experimental and theoretical point of view. Among all types of the clusters, gold clusters are probably the most extensively studied. In this chapter the cluster production techniques, structures, energetics, the growth and stability of nanoclusters will be reviewed.

2.2 Cluster Production

The manufacturing of nanoclusters includes top-down and bottom-up approaches, where the latter approach has the advantages of producing ultrasmall cluster in parallel and at lower cost. Particularly, the cluster beam method produces free clusters in gas phase, which is very good for study the fundamental growth mechanism of the clusters and

employed in this thesis and presented in the later experimental chapters. Thus in this section it focuses most attention on this method. In practice, atomic vapour deposition, chemical synthesis, and self-assembly approaches, are all used for specific applications, which are also included in this chapter, but to a less extent.

2.2.1 Cluster beam production

2.2.1.1 Cluster sources

Reviews of the gas phase cluster sources currently in use can be found in four excellent papers [11, 12, 13, 14]. There are six types of the cluster sources, including seeded supersonic expansion [15, 16], inert gas condensation [17, 18, 19], laser ablation [20, 21, 22, 23, 24], electrical arc discharge [25, 26], ion sputtering [27, 28, 29, 30, 31] and liquid metal ion source [32]. These sources can produce ionised clusters or neutral clusters. The neutral clusters are usually ionised at latter stage which enables the manipulation using electromagnetic fields, such as size-selection or high energy deposition [33]. Figure 2.1 shows the layouts of these six types of cluster sources.

Seeded supersonic expansion cluster source first vaporises the metal and mixes the atoms with inert gas (usually Ar) [12]. The inert gas pressure is several times higher of atmospheric pressure and the metal partial pressure is 10-100 mbar. When this stream of gas passes through a conical shape nozzle into vacuum, the isentropic expansion leads to an adiabatic cooling. Clusters form near the nozzle as the temperature and atom density decrease with distance from the nozzle. This technique is suitable for metals with low

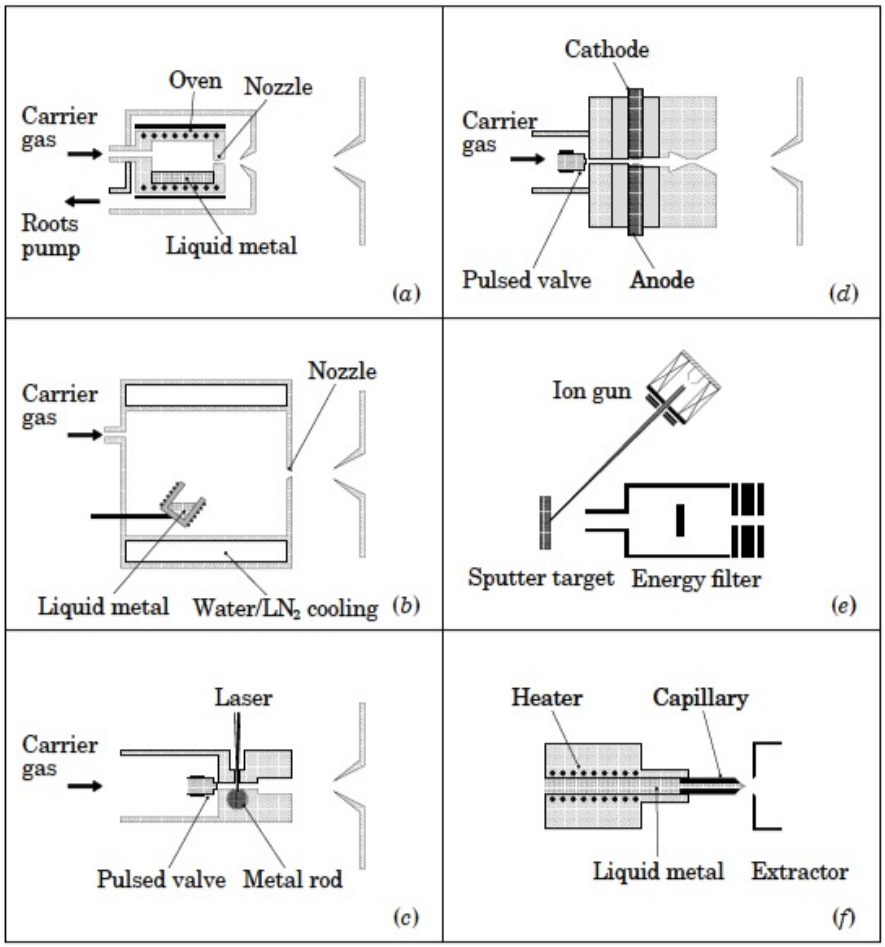

Figure 2.1: (a) Seeded supersonic nozzle source. (b) Gas condensation source. (c) Vaporisation source. (d) Pulsed arc cluster ion source. (e) Ion sputter source. (f) Liquid metal ion source. This figure is adapted from reference [11].

boiling point and can generate an abundant number of clusters [12].

The inert gas condensation cluster source also involves vaporising metal into cold inert gas. The metal vapour becomes supersaturated and condenses into clusters, then the mixture passes through the nozzle. The difference between this cluster source and the seeded supersonic expansion cluster source is that in this case clusters form before the nozzle [11]. Normally the temperature is very low, so the re-evaporation rate of the atoms

on the surface of cluster is negligible and clusters formation primarily by successive single atom addition [12]. Thus the thermodynamic stability of clusters, or in another words, the abundance of clusters, is mainly dependent on the collision statistics, and the mass spectrum usually shows a smooth curve [12].

In contrast to the continuous sources mentioned above, laser pulses can also be used to produce the metal vapour. The metal vapour is ejected out of the nozzle by the cold inert gas, which causes cluster condensation. This technique is applicable to almost any metal, even for those that are refractory.

The pulsed arc cluster ion source is based on the laser ablation source [11, 25]. It uses an electric arc to vaporise the material instead of a laser pulse. It has advantages of being cheaper and producing a more intense beam than the laser ablation source [12].

The ion sputtering source uses inert gas ions with high momentum to sputter off the target material non-thermally [34]. There are two types of ion sputtering source: ion beam bombardment and plasma sputtering. In the ion beam bombardment source, the ions are created using plasma discharge or heating and accelerated through a few keV towards the targets [34]. The plasma sputtering source makes use of ignited inert gas plasma in the vicinity of the target surface [35, 36] and a magnetron is placed behind the target to stabilize the plasma and promote sputtering. This type of cluster source has very high rate of ionisation [37] and can produce negative, positive and neutral clusters.

The liquid metal ion source includes a capillary filled with the liquid metal with a large electric field applied to it. The electric field pulls the liquid metal out from the needle into vacuum to induce ion injection [38]. This technique is simple but limited to

low melting point materials and is only capable of producing small clusters (tens of atoms [32]).

2.2.1.2 Mechanisms of gas-phase cluster formation

The cluster production in a gas phase usually involves two steps: (1) nucleation and (2) growth.

Generally speaking, nucleation can happen both heterogeneously and homogeneously, distinguished by the place the nucleation occurs. Heterogeneous nucleation is more frequently observed. For simplified models, the classical nucleation theory [11] is extensively used, which considers the Gibbs free energy, ΔG, of the system. The change of Gibbs free energy includes both surface and volume contribution and can be written as

$$\Delta G = 4\pi r^2 \sigma + \frac{4\pi r^3}{3} \Delta G_V, \tag{2.1}$$

where σ and ΔG_V are the surface tension and Gibbs energy per volume, respectively. The nucleus is assumed as a perfect sphere with radius r and atomic volume V_L. In the case of gas, $\Delta G_V = -k_B T \ln(P_V/P_S)/V_L$, where P_V is the vapour pressure, P_S is the saturation vapour pressure at the temperature T and k_B is the Boltzmann constant. When the system reaches the equilibrium, $d\Delta G/dr = 0$, which gives the critical radius [13],

$$r_c = \frac{2\sigma V_L}{k_B T \ln(P_V/P_S)}. \tag{2.2}$$

The critical diameter is $d_c = 2r_c$. When the nucleus is smaller than the critical diameter,

it reduces the free energy by evaporation. If it exceeds the critical diameter, it reduces the free energy by growing [11]. As can be seen in Equation 2.2, increasing the supersaturation leads to smaller critical diameter. The classical nucleation theory is useful in many ways, however there are some debate as to whether it is applicable to nanoclusters with only a few atoms as it is considered that surface tension may not be an appropriate way of modelling the unfavourability of surface sites on an atomic scale [11].

In principle, once the size of cluster overcomes the critical radius the cluster can grow through two body collision, which is forbidden during cluster nucleation because the atoms in vapour have much higher kinetic energy than the bonding energy. There are two mechanisms for cluster growth: adsorption of atoms (surface growth) and the coalescence of colliding [14]. The surface growth starts with atoms approaching the surface of an already-formed cluster and undergoing a chemical reaction or phase change at the cluster surface. Surface growth can be very important at the early stage of cluster formation and can contribute to the entire cluster growth process in a system with sufficient vapour [13]. Coalescence describes cluster-cluster collisions due to Brownian motion or other mechanisms. Hihara and Sumiyama simulated computationally plasma sputtering and showed that the adsorption of atoms is the dominant process [30]. The growth continues until when either the clusters exit the condensation chamber or the surrounding atomic vapour is exhausted [34]. The size distribution is an asymptotic self-preserving distribution and remains invariable with growth time if the cluster size and concentration are scaled with the average particle volume [39].

2.2.2 Atomic vapour deposition

The atomic vapour deposition is usually used in thin film growth where atomic vapour is produced by plasma sputtering or heating, and is deposited and aggregated on the substrate. The size distribution is usually wide and can be controlled by lithographic masks. The deposition rate and the surface temperature of the substrate are very important in controlling cluster size and shape [41]. For example, in Figure 2.2 the Au clusters were produced by thermal evaporation and were found to be hemispherical in morphology with size from 2 to 5.5 nm, due to aggregation of the clusters deposited on amorphous carbon [40].

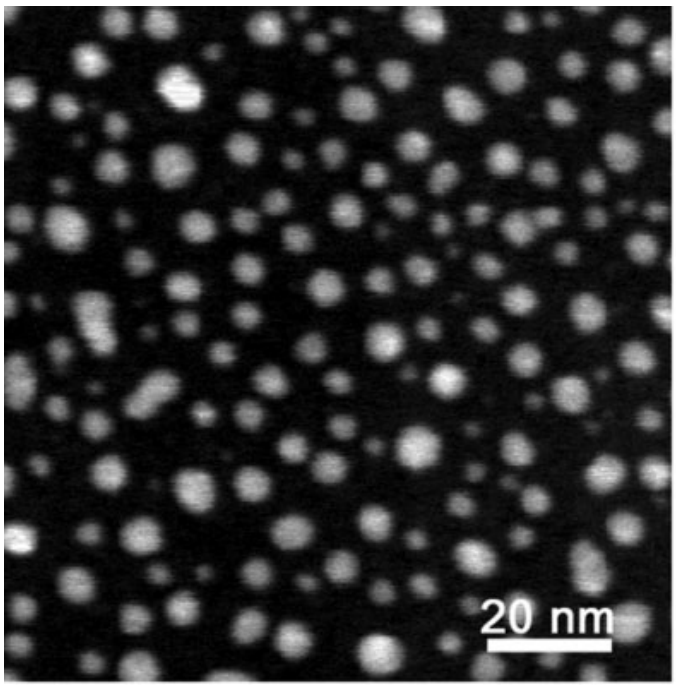

Figure 2.2: Au clusters deposited on the amorphous carbon made by atomic vapour method. This figure is adapted from [40].

2.2.3 Chemical synthesis

Chemical synthesis is a versatile and inexpensive way of producing nanoparticles [43]. It involves making use of metal or semiconductor salts [44, 45, 46]. The earliest study of the colloidal synthesis is probably from Faraday [47]. A soluble salt is dissolved in liquid to supersaturated conditions, and subsequently reduced so that nanoparticles can form. The size dispersion, shape and crystallinity of the particles can be controlled by the parameters in the solution, such as pH or ion concentration. Nanoparticles made using this method can be very useful if their applications require them to be used in solution [48], for instance, as platforms for further deposition [49]. Figure 2.3 shows different shapes of colloidal FCC metal nanocrystal (Ag, Au, Pt) bounded with {111} and {100}

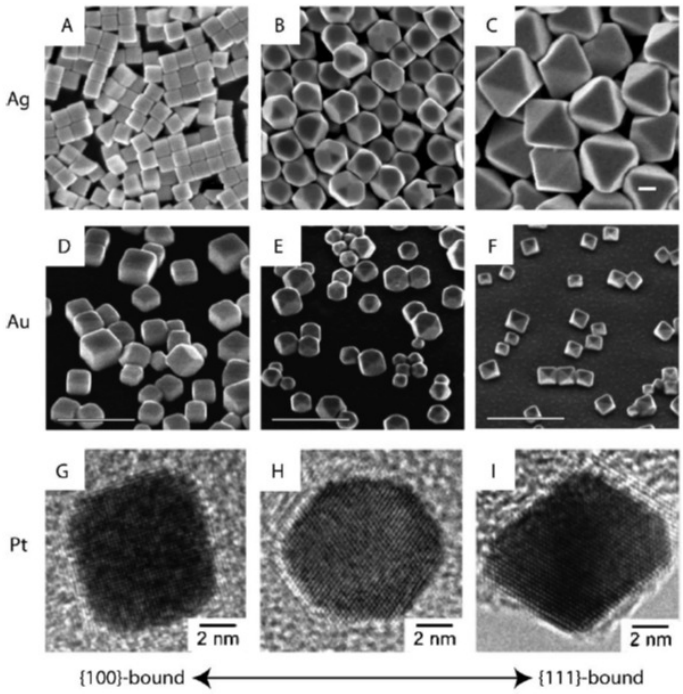

Figure 2.3: Polyhedral metal nanocrystal (Ag, Au, Pt) synthesised using colloidal synthesis method. These nanocrystal are bounded by the FCC {111} and {100} planes but with different ratio. This figure is adapted from [42].

planes.

2.2.4 Self-assembled cluster on surface

Self-assembly is a "spontaneous assembly of atom/molecules into structured, stable, non-covalent joined aggregates under equilibrium" [50]. If the appropriate conditions are met, the self-assembly can occur with sizes ranging from the molecular to the macroscopic [51] [52]. To date, self-assembly has been demonstrated in metals (Au, Ag), metal ion salts ($Ca_3(PO_4)$, $CaCO_3$), quantum dots (CdS), magnetic (Fe_3O_4) and photo-active (TiO_2) oxides, and glassy solids (SiO_2), which are chemically integrated with discrete organic nanostructures [53]. The primary mechanism for self-assembly is through the adsorbed species randomly hopping across at the substrate atomic lattice thermally [54]. The diffusivity D (the mean square distance travelled by an adsorbate per unit time), which obeys Arrhenius law, is usually compared with the deposition rate F. If the ratio D/F is large, the growth will be close to equilibrium condition which means the (meta-stable) absorbed species have enough time to explore the potential energy surface allowing the system to reach a minimum energy configuration, otherwise the growth is determined by the kinetics [54, 55] (illustrated in Figure 2.4). However, this method is usually limited to the specific circumstances in which the clusters are produced and can not be generalised [41].

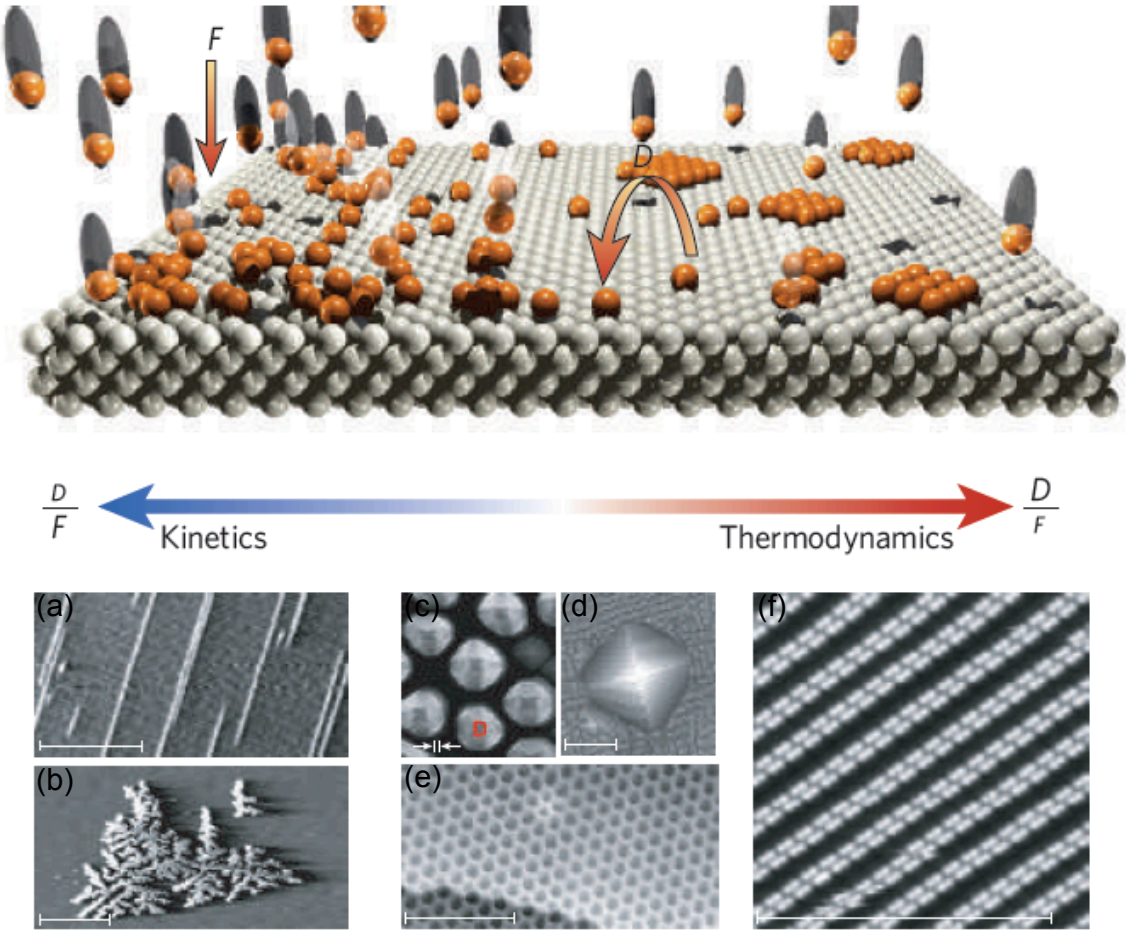

Figure 2.4: This figure is adapted from [54]. Top: the schematics of deposition of atoms or molecules vapour. (a) Cu chain grown on an anisotropic Pd(110) substrate. (b) Ag dendrites on hexagonal Pt(111). The semiconductor nanostructure are usually grown at intermediate D/F as shown in the centre whereas dome-shaped and pyramidal Ge semiconductor quantum dots grown on Si(100) ((c) and (d) respectively). (e) A boron nitride nanomesh on Rh(111) (f) An an example of superamolecular nanograting of rod-like benzoic acid molecules on Ag(111) which is close to the equilibrium condition. All of the scale bars are 20 nm.

2.3 Cluster Structures

For an FCC crystal, the stacking fault ABCABCCBACBA (A,B,C are three possible positions), instead of regular growth sequence ABCABCABCABC, leads to twinning [56].

Apart from Lamellar twinning, where parallel contact twins repeat continuously one after another [56], multiply twinned particles (MTP, including Dh and Ih) or their variations can be often seen [57]. MTPs can be produced through gas phase, liquid phase and solid phase techniques [57]. Recently, it has been found that the strain on the multiple twining particle can enhance the catalytic performance [58] or influence the catalytic selectivity [59]. In this section, the basic crystallographical geometries of Ih, Dh and FCC will be reviewed, but not including their variations [60, 61] for the sake of conciseness. Figure 2.5 shows paper models of the three main structures (FCC, Dh and Ih). It can be seen that each model exposes different {111}/{100} facet ratios.

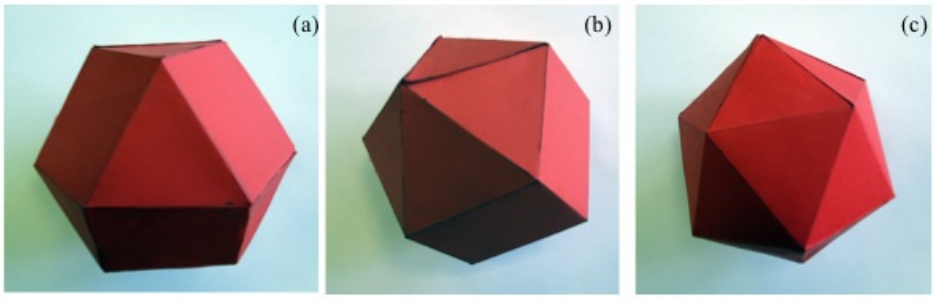

Figure 2.5: Paper models of (a) cubo-octahedron , (b) Ino-Dh and (c) Ih. The triangle faces are {111} facets and the square faces are {100} facets.

2.3.1 Icosahedron

An Ih consists of 6 fivefold axes and 20 distorted tetrahedral units sharing the same vertex at the centre. The tetrahedra have {111} facets exposed and every adjacent tetrahedral unit shares crystallographical {111} facets. Figure 2.6 (a) and (b) show Ih viewing from two different orientation. The three sides of each tetrahedral units that lie towards the

centre are about 5% (the dashed lines in Figure 2.6 (c)) shorter than the three sides on the surface (The solid lines in Figure 2.6 (c)) [62]. The adatoms deposited on the facets can be placed on the sites of FCC (Mackay) or hexagonal close packed (HCP, anti-Mackay) stacking [63]. The number of atoms in an icosahedron with k full shells is [64] (Figure 2.6)

$$N = \frac{10}{3}k^3 + 5k^2 + \frac{11}{3}k + 1. \tag{2.3}$$

This number sequence is also applicable to some Ino-Dh and FCC cubo-octhedra which will be discussed later. Theoretic calculations have shown that, at the very beginning of cluster formation, Ih is energetically favoured [65]. It has been argued that the Ih can be formed by freezing [66, 67] and melting [68]. Baletto et al. have shown theoretically that Ih can grow at low temperature and then transform to Dh [69]. A number of variants of Ih have been found in the literature [63], and it is suggested that the Ih with "crater" on

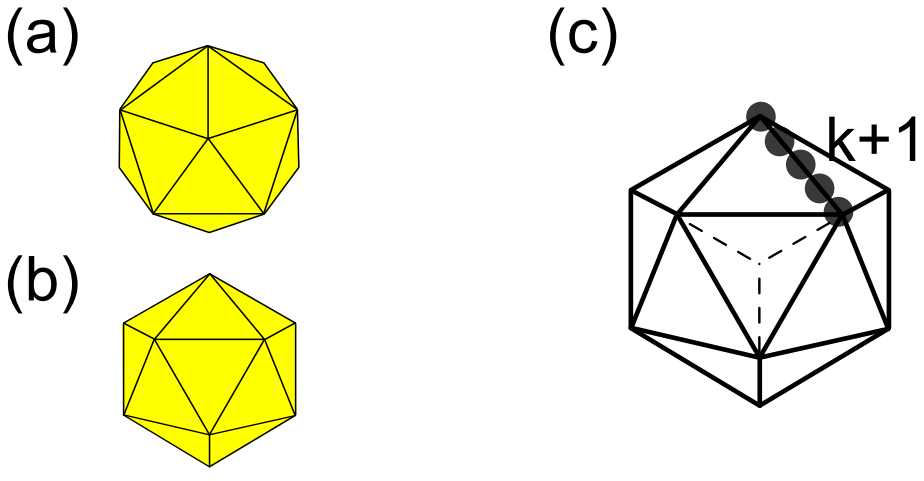

Figure 2.6: The schematics of icosahedron. (a) and (b) show the geometry of an icosahedron with two orientations. The yellow colour means that the structure is enclosed with {111} facets. (c) The the number of shell+1. The dashed lines are the the sides of the units inside the model.

each corner (Chui Ih) are more stable and thermodynamically realistic at large size [70] [71] [72]. Mechanism for the structural transformation from Ih to Dh has been discussed by Koga [6].

2.3.2 Decahedron

The classic Dh (indicated in Figure 2.7 (a) and (b)) includes five tetrahedral units [73]. Each tetrahedral unit has four slightly distorted equilateral triangle {111} facets and shares two of their faces as twinning planes with other units, whilst the other two facets form the surface of Dh. Compared with Ih, Dh has lower strain energy, which is partially due to lower strain in the tetradehedral units. In addition, Dh can minimize strain energy by changing the size and shape of units. The classic Dh is not very spherical, which makes it unfavourable energetically [74] and experimentally Ino- and Marks- Dh are more often observed (Figure 2.7 (c-d) and (e-f) respectively).

In fact, classic and Ino Dh are special case of Marks Dh in terms of mathematic description. With three integer geometry parameters, m, n and p (indicated in Figure 2.7 (g)), the number of atoms the Marks-Dh contains is

$$\begin{aligned} N &= \frac{1}{6}\{30p^3 - 135p^2 + 207p - 102 + 5m^3 + (30p - 45)m^2 \\ &\quad + m[60(p^2 - 3p) + 136] + n[15m^2 + (60p - 75)m \\ &\quad + 3(10p^2 - 30p) + 66]\} - 1. \end{aligned} \tag{2.4}$$

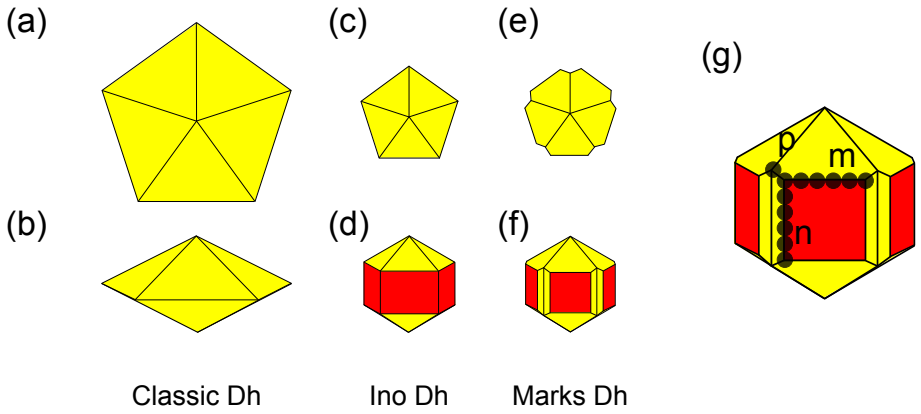

Figure 2.7: The geometries of classic Dh (a-b), Ino Dh (c-d), and Marks Dh (e-f). (g) is the definition of the parameters for Dh [75, 76]. The yellow color and red color represent {111} and {100} facets.

The length of the symmetry axis is $m + n + 2p - 3$. When $p = 1$ the cluster becomes Ino-Dh (indicated in Figure 2.7 (c) and (d)) with {111} (top and bottom) and {100} (side) facets exposed. For Ino Dh ($p = 1$) with $m = n$, giving square {100} facets at the side, Equation 2.4 become the same as Equation 2.3, i.e. they have the same number sequence. For classic Dh, $p = 1$ and $n = 1$.

2.3.3 FCC

The FCC particles can be seen as a fraction of bulk material with crystalline structure. In an equilibrium state, the particles should form a Wulff construction [77], fulfilling this equation [78],

$$\frac{\gamma_{(100)}}{\gamma_{(111)}} = \frac{d_{(100)}}{d_{(111)}}, \tag{2.5}$$

where $\gamma_{(100)}$ and $\gamma_{(111)}$ are the (100) and (111) surface energies, and $d_{(100)}$ and $d_{(100)}$ are the distances of the corresponding facets from the centre of the cluster. Figure 2.8 shows

the evolution between the cube and octahedron by modifying their morphologies through selective growth or cutting on certain facets ({111} or {100}). The shape of each face is triangular, square, or hexagonal [78].

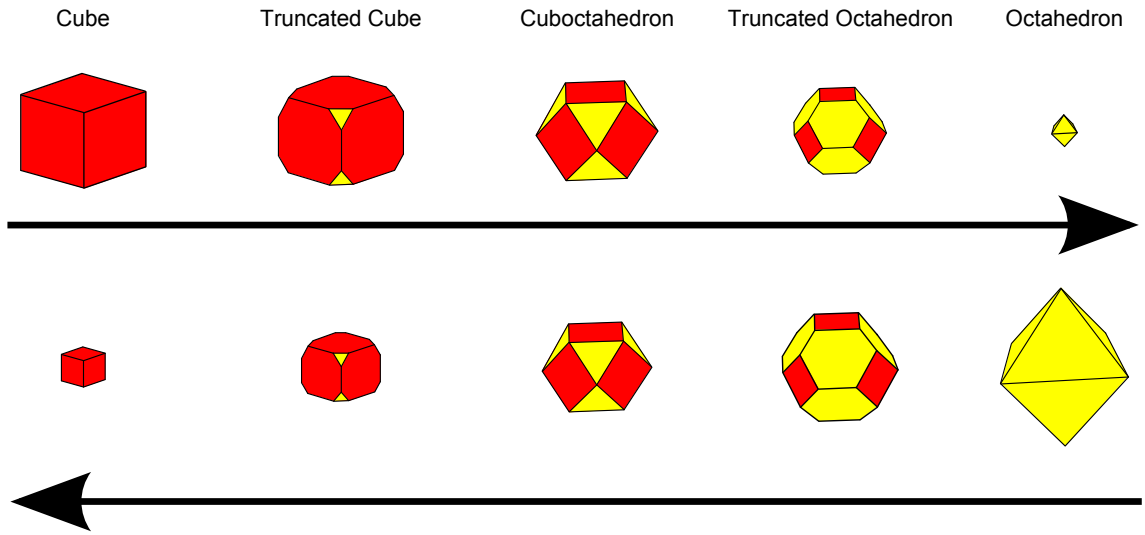

Figure 2.8: Modifying the shape between cube and octahedron by different depth of cutting. Yellow is the {111} facets and red is the {100} facets.

2.4 Energetics of clusters

The energetics of clusters is very important when it comes to their structure preference, particularly for those have the lowest energy. There are two steps considered in theoretic calculations: (1) building a model for the interactions between the elementary constituents of the cluster, including solving the Schrödinger equation directly, or constructing the semi-empirical inter-atom potentials, and (2) searching for the most favoured isomers by applying a global optimization algorithm [78].

The choice of energetic modelling method is crucial. The *ab initio* method is accurate

but becomes cumbersome as the size of cluster increases. Methods based on density-functional theory can be highly accurate and are less cumbersome if tested adequately. The weak point in density functional calculations is that often the exchange and correlation term is treated in an approximate way [78]. There are also several approximate energetic models based on semi-empirical methods. At an intermediate degree of computational effort, there is the tight-binding model for semiconductors [79] and metals [80]. Based on approximately quantum models, classic atom-atom (or molecule-molecule) potential can be useful for large systems. The parameters in these potentials need to be fitted to experimental material properties or to density functional calculation, for example, using the embedded atom method (EAM) and second moment approximation to tight binding (SMATB, including Gupta, Rosato-Guillopé-Legrand (RGL), and Sutton-Chen potentials) [81].

The binding energy of a cluster which contains N atoms can be presented as

$$E_b = aN + bN^{2/3} + cN^{1/3} + d, \tag{2.6}$$

where the first term corresponds to the volume contribution and the others are surface contributions from facets, edges and vertices, respectively. To describe the stability of clusters, the excess energy per surface atom with respect to N atoms in a perfect bulk crystal [78], Δ, is introduced

$$\Delta(N) = \frac{E_b - N\epsilon_{coh}}{N^{2/3}}, \tag{2.7}$$

where ϵ_{coh} is cohesive energy per atom in the bulk material.

Many works show that FCC structures are not necessarily the lowest energy structure for smaller cluster sizes [82]. In 2002, Baletto et al. worked out the energy cross-over of the structure of noble metal clusters (Figure 2.9 [65] for Au). By using different potentials, the exact crossover is slightly different, but the result shows that the general trend of the minimum energy structure is Ih<Dh<FCC in size. In particular, the transition size for gold was found to be less than 100 atoms from Ih to Dh or FCC, and 500 from Dh to FCC.

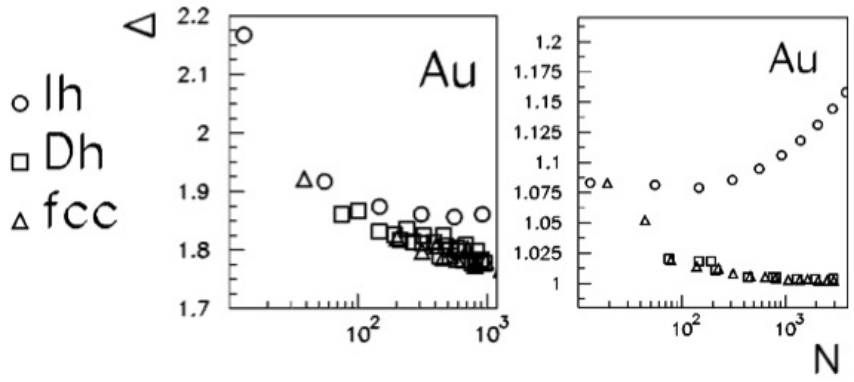

Figure 2.9: Excess energy Δ as a function of the number of atoms within cluster for different gold cluster structures. The work has been done by Baletto and Ferradno and the figure is reproduced from [65]. The left one uses EAM and the right one uses RGL.

2.5 Current study on the cluster structures

Apart from the size distribution usually concerned in producing the nanoclusters [83], the structure of nanocluster is another independent parameter which can have influence on their optical properties [84, 85] and catalytic activities [86]. In the literature, the tools used

to study the structure include electron microscopy imaging (scanning electron microscopy (SEM) and (S)TEM), electron diffraction [87], X-ray diffraction [88] and scanning probe microscopy[89]. Here the previous studies on cluster sturtcure is summarised. They are grouped into theoretic and experimental work, with focus on the growth and stability of nanoclusters, with the emphasis on gold.

2.5.1 Theoretic work

Regarding to the growth of the clusters, Grocholar et al. used the EAM to simulate the initial nucleation, coalescence and growth kinetics of vapour synthesized gold nanoparticles [90]. This work shows that at early stage (N <300 atoms) coalescence greatly improves the chance of Dh and FCC structure forming, while the aggregation rate and the type of noble gas vapour used had little impact on structure statistics. Also using the EAM, Feigl et al. found that increasing the size of initial seed can decrease the chance of transformation to Ih during the growth whilst higher temperature has a positive effect of transformation [91]. Desgranges and Delhommelle used both hybrid Monte Carlo and Molecular Dynamics simulations to study the nucleation of nanogold from a supercooled liquid [92]. They showed that, although the structure of the nucleus is dominated by stable FCC structure in the early stage, meta-stable HCP structures nucleate heterogeneously on the surface when the size approaches the critical diameter [93]. Successive cross-nucleations between two polymorphs can lead to the growth of the crystallite [92]. Baletto et al. studied the microscopic mechanisms in the growth of meta-stable silver Ih, and pointed out that, at low and intermediate temperature (350 <T< 500 K), noncrys-

talline structures such as Ih and Dh are likely to be formed, whereas the meta-stable Ih grows in shell-by-shell mode or by a complete structural transformation from a Dh [69]. Baletto et al. simulated silver clusters up to N≃150, showing that at a given deposition flux, Ih structures are obtained at low and high temperature while Dh forms at the intermediate range [94]. It has also been found that the immersion environment can play a role in the growth of gold nanostructures [95].

As the cluster grows, the strain of MTP can become very big, their stability has been taken into account theoretically. In the case of gold, Ino's calculation predicts that free gold clusters are stable with diameter smaller than 43.6 nm for Ih and 396.1 nm for Dh by taking into account of the specific surface energy, twin boundary energy and the elastic strain energy [97]. Chui argue that the effect of surface disorder plays a very important

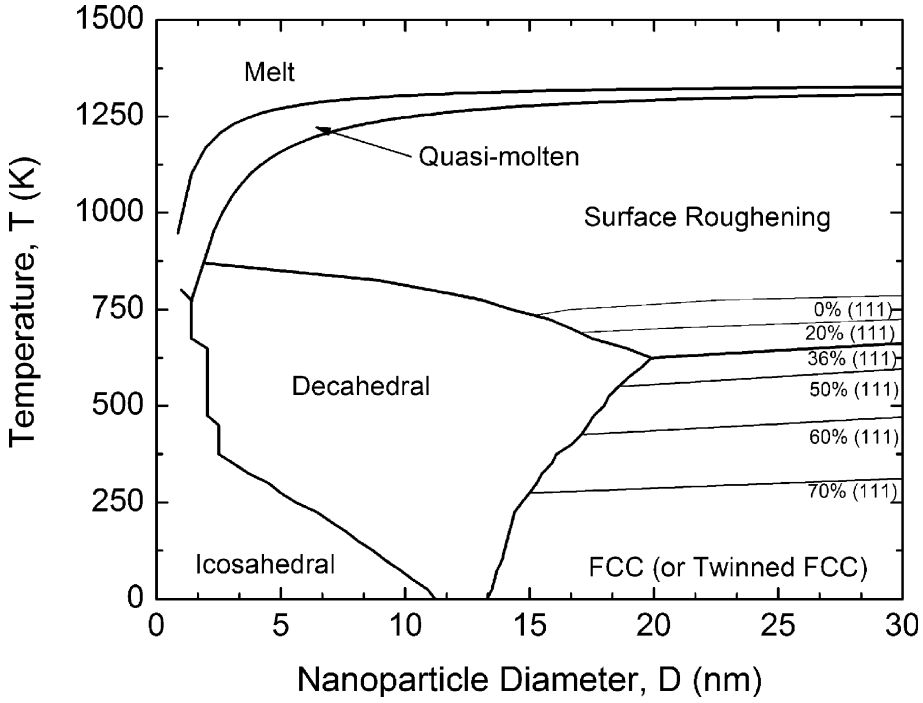

Figure 2.10: Gold phase map based on relativistic first principles calculations. This is adapted from [96].

role in considering the stability of the nanoclusters [72]. From an energetics point of view, by applying two different semi-empirical potentials, Baletto et al. found that the crossover for Ih to Dh or FCC happens at less that 100 atoms, while Dh to FCC happens at about 500 atoms for gold [65]. Cleveland et al. has also found that for Ni cluster there is the same trend for Ih as increase of size [73]. Barnard et al. calculated the phase map for gold based on the first principles (Figure 2.10) [96]. In addition, the substrate can also play a role in cluster growth by altering both free energy stability and free energy barriers [98], for example, the silica surface can cause cluster transformation from Dh to Ih during growth [99].

When clusters are heated, the surface softens[100] and reconstructs [101, 102] and they can also form a liquid skin [103] or a quasi-molten state [99] before fully melting. By using EAM Schebarchov et al. found that Pt Dh at the size of 887 and 1389 transform to FCC before they melt [104]. In addition, similar behaviour has been also found for Pd_{887} [105]. In contrast to heating the cluster, Chushak studied the freezing process of molten clusters with 1157 gold atoms using a cooling rate 3×10^{11} K/s to show most of them formed Ih [106]. The crystallisation process has been studied in many groups. In general, the results show that the crystallisation starts from the surface [66, 107, 108] which provides a template for the latter crystallisation [109].

2.5.2 Experimental work

On the experiment side, the multiply twinned structures metallic nanoparticles have been observed for more than several decades [148]. Table 2.1 summaries the studies on gold

Table 2.1: Summary of Au MTP particles observed in experiments

Year	Method	Type	Size	characterization method	Reference
1964	Atomic vapour deposition	Dh	30 nm	TEM	[110]
1966	Atomic vapour depoistion	Dh Ih	40 nm 10-40 nm	TEM	[111]
1967	Atomic vapour depoistion	Dh Ih	30 nm 15 nm	TEM	[112]
1967	Atomic vapour depoistion	Dh	500 nm	TEM	[113]
1968	Atomic vapour deposition	Dh Ih	15 nm 13 nm	TEM	[114]
1969	Atomic vapour depoistion	Dh Ih	15 nm 10nm	TEM	[115]
1972	Atomic vapour deposition	Dh Ih	20-40nm 15-30 nm	TEM	[116]
1973	Chemical synthesis	Dh	30 nm	TEM	[117]
1975	Atomic vapour deposition	Dh Ih	40 nm 40 nm	TEM	[118]
1977	Atomic vapour deposition	Dh Ih	15 nm 8 nm	TEM	[119]
1979	Atomic vapour deposition	Dh	12-40 nm	TEM	[120]
1981	Cluster beam	Dh Ih	6 nm 7 nm	TEM	[121]
1983	Atomic vapour deposition	Dh	10 nm	TEM	[122]
1984	Atomic vapour deposition	Dh	70-100 nm	TEM	[123]
1985	Atomic vapour deposition	Ih	30 nm	TEM	[124]
1986	Atomic vapour deposition	Dh	2.5 nm	TEM	[7]
1988	Atomic vapour deposition	Ih	5 nm	TEM	[125]
1989	Atomic vapour deposition	Dh	2-6 nm	TEM	[126]
1990	Inert gas aggregation	Dh	4 nm	TEM	[127]
1990	Chemical synthesis	Dh	65nm	TEM	[128]
1995	Chemical synthesis	Dh Ih	40 nm 20 nm	TEM	[129]
1996	Chemical synthesis	Dh	50-60 micron	SEM	[130]
1997	Chemical synthesis	Dh Ih	40 nm 20 nm	TEM	[131]
2000	Chemical synthesis	Dh	2-4 nm	TEM	[132]
2000	-	Dh	5 nm	TEM	[133]
2000	Atomic vapour depostion	Ih	6 nm	TEM	[134]
2003	Chemical synthesis	Dh Ih	5 nm 5 nm	TEM	[59]
2003	Cluster beam	Dh Ih	3-18 nm 3-18 nm	TEM	[135]
2005	Chemical synthesis	Ih	100 nm	SEM	[136]
2006	Chemical synthesis	Dh	400 nm-5 micron	SEM	[137]
2007	Chemical synthesis	Dh	5 nm	TEM	[138]
2007	Chemical synthesis	Ih	10-90 nm	TEM	[139]
2008	Chemical synthesis	Dh Ih	120 nm 94 nm	TEM & SEM	[140]
2008	Chemical synthesis	Ih	300-400 nm	SEM	[141]
2008	Cluster beam	Dh	2 nm	TEM	[9]
2009	Chemical synthesis	Dh	3 nm	TEM	[142]
2009	Chemical synthesis	Dh	10 nm	TEM	[143]
2010	Chemical synthesis	Dh Ih	30-40 nm 15-20 nm	TEM	[144]
2010	Chemical synthesis	Dh Ih	9-20 nm 7.2 nm	TEM	[145]
2012	Chemical synthesis	Dh	3nm-1 micron	TEM & SEM	[146]
2012	Cluster beam	Dh Ih	3 nm 3 nm	TEM	[147]

MTP nanoparticles reported in the literature using electron microscopy since 1964. For other metals, the list of MTP can be found in [56]. It can be seen (Table 2.1) that the MTP can be made using all kinds of synthesis methods. It is worth to note that both Dh and Ih structures have been observed in experiments up to very large sizes (a few microns and several hundred of nanometer respectively).

There are two reports worthy of mentioning on manipulating Au nanoparticle structure. The first one was electrodeposition, where the MTP are preferred at low potential while high potential leads to single crystalline or polycrystalline nanoparticles [131]. The second study conducted by Lee's group, using 1,2-hexadecanediol to reduce the $AuCl_4^-$ in the solution, found that the crystallinity of the formed nanoparticle was strongly dependent on the concentration of the $AuCl_4^-$, although the mechanism responsible for this was not identified [144].

The instability of nanoclusters has also been studied experimentally. The first observation of structure fluctuation in a small cluster was reported by Iijima and Ichihashi in 1986. The 2 nm gold nanocluster, on the surface of SiO_2, under illumination of 120 kV TEM with the dose of $1.3 \times 10^7 e/\text{nm}^2$, was found to flip randomly between single crystal and MTP structures [7]. For larger Au clusters (3 nm), Wang and Palmer found trends in structural transformation whereby Ih was the least stable structure and would transform either to Dh or FCC under 200 kV STEM scanning [147]. Young et al. studied the structural transformation over a greater size range with well controlled temperature, finding that in the size range of 5-12 nm, the cluster transformed to Dh regardless of their initial structure when they were *in-situ* heated [145]. In addition, Dh also has been found to

transform to Ih while cooling [145]. Another inspiring experiment was conducted by Koga et al. in 2004 [6]. When the clusters were annealed in gas phase, the clusters with 3-14 nm underwent structural transformation from Ih to Dh, whilst a melt-freeze process leads to Dh (7- 17 nm) to FCC transformation. Apart these studies of bare Au nanoclusters, there have also been reports of structural instability of passivated gold clusters [149], and the fluctuation of structure at extremely small scale (< 100 atoms) [150, 151].

2.5.3 Mechanisms of MTP formation and structural transformation

The origins of MTP has been reviewed by Gryaznov et al. [76] as shown in Figure 2.11. (a) shows that MTP can be formed by sequential joining of tetrahedra. (b) represents a sequential twinning model, which is caused by the presence of shear stresses of the planes perpendicular to the film surface. (c) is the well known model for MTP in small atomic clusters, for example, a Dh can form with a 7 atom embryo or an Ih can form with a 13 atoms embryo. (d) shows that a MTP formed from liquid phase, where when the cluster passes the liquid-solid boundary, the prerequisite for an embryo of with five fold symmetry to originate is enhanced, then during cooling, this embryo inter-grows inside, transforming into the MTP. (e) is another model where the crystal structure fluctuates during growth and by chance it reaches as the MTP, which is relatively more stable than other structures, so it becomes trapped in that structure.

For the transformation of gold cluster from Ih to Dh, Koga et al. proposed that it

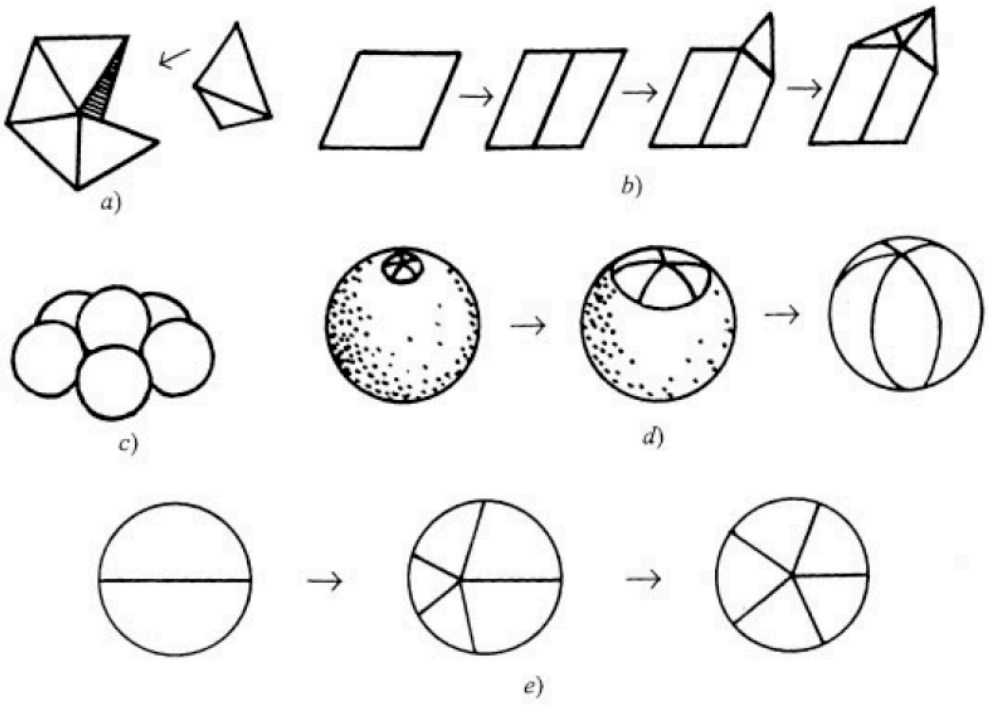

Figure 2.11: The possible mechanisms of MTP formation. This figure is adapted from [76].

is due to a cooperative slip dislocation of {111} planes in the Ih structure (Figure 2.12) [6]. The Ih has 10 distorted FCC tetrahedra in the middle around the five fold axis. 5 of these tetrahedra in the upper region and 5 in the lower region (Figure 2.12 (a)) with (111) plane as boundaries. When these (111) planes slip on its underlying plane shown as arrow in Figure 2.12 (c), the neighbouring tetrahedra merge into a new pyramid segment exposing a {110} plane [6]. Such non-diffusive cooperative process is considered to have much lower energy barrier.

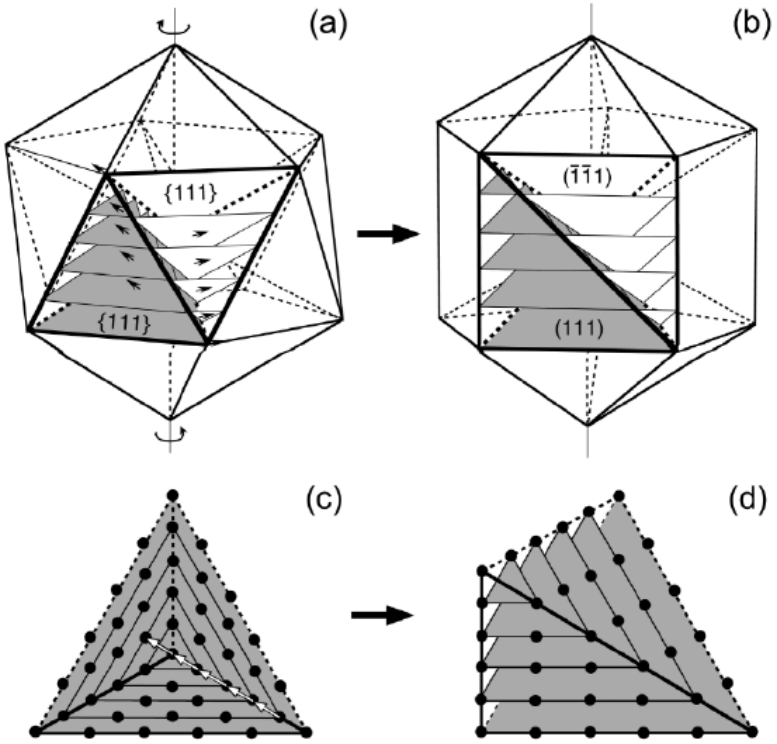

Figure 2.12: The mechanism of Ih transforming into Dh. This figure is adapted from [6].

2.6 Summary

Apart from the size, which is an usual concern in manufacturing the nanocluster, the structure is another dimension that possibly makes the nanoparticles present fascinating properties. As can be seen in the literature, due to the computational affordability, theoretic work has studied the structures of ultrasmall (less than 5 nm) nanoparticles from many aspects, such as energetics, melting, structural transformation etc. However, there are few experimental work on the structure of cluster, leaving some open questions, such as why do these big Ih clusters exist, how do the structures transform into each other? In this thesis, these questions will be discussed experimentally by studying the size-selected Au_{887} clusters.

Chapter 3

Aberration Corrected Scanning Transmission Electron Microscopy

3.1 The development of (S)TEM

Prior to the early of 20th century, microscopes using visible light were the principal method used by scientists to observe small objects and explore the micro-world. However, this technique met an insurmountable limit to resolution, called the Rayleigh limit, which limited the use to objects of several hundreds of nanometres size. The Rayleigh limit states that the visibility of an object is approximately in the same order of the wavelength of illuminating source [152]. In 1925, de Broglie proposed that the principle of wave-particle duality implies that electrons travel like waves with wavelength λ determined by their momentum p, $\lambda = h/p$, where h is the Planck constant. The momentum of an electron is given by $(2m_eV + eV^2/c^2)^{1/2}$, with relativistic correction, where m_e, c and e correspond respectively to the rest mass of electron, light speed in vacuum and unit electron charge. Thus the wavelength of electrons can be tuned by altering the accelerating voltage V [152].

For example, in the case of accelerating voltage of 200 kV, the corresponding wavelength is 2.75×10^{-3} nm with consideration of relativistic effect. This compares to traditional optical microscope, where the wavelength is 100 nm or even higher; thus the electron microscope provides a significant improvement of resolution.

By applying the theory of visible light to electron optics, in 1932, Ernst Rusk and Max Knoll successfully constructed the first transmission electron microscope (TEM) for which Ernst Rusk was awarded the Nobel Prize in Physics in 1986 [153]. In 1938, Manfred von Ardenne successfully developed scanning transmission electron microscopy (STEM) by rastering beam across the sample [154]. Unlike conventional TEM, which illuminates the sample with parallel electron beam, STEM uses a focused beam. A range of analysis techniques are possible in STEM, such as mapping of Energy Dispersive X-Ray (EDX), electron energy loss spectroscopy (EELS) and annular dark field (ADF) imaging. The spatial resolution of STEM is the size of the electron probe on the sample, which is formed by the objective lens located before the sample optically [155].

In 1936, Scherzer stated that round electron lenses always suffer from positive spherical aberration, which limits their resolution [157]. In 1947, a non-rotationally symmetric corrector was proposed by Scherzer [158], to overcome this aberration. This aberration corrector produces a negative aberration to cancel the positive aberration generated by the round lens [159]. Recent advances in manufacturing of aberration correctors bring the resolution into a new era, not only improving the two dimensional resolution but also depth sectioning resolution [160, 161]. Figure 3.1 shows the development of the resolution of microscopes. Nowadays the state-of-the-art aberration corrected microscope

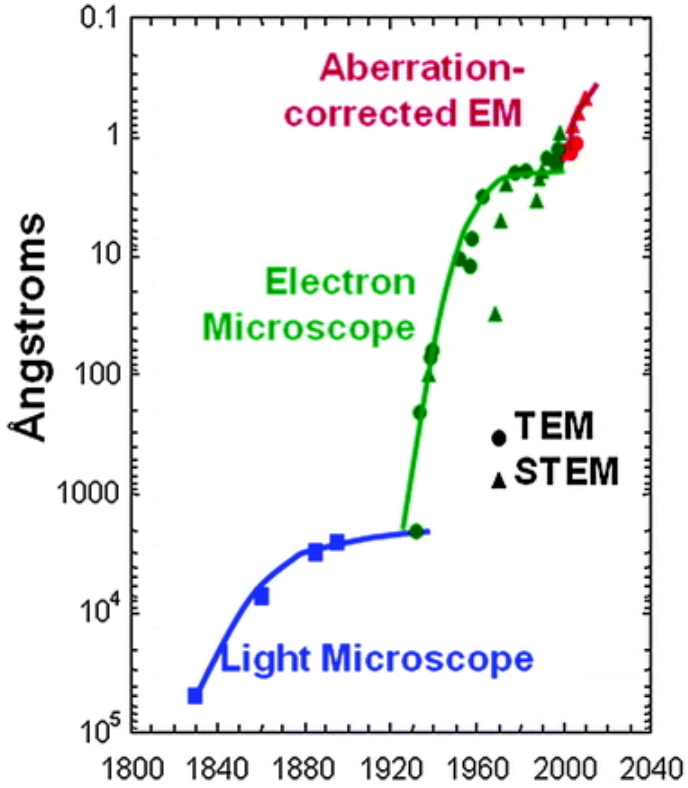

Figure 3.1: The development of the spatial resolution of microscope. This figure is adapted from [156]

can achieve sub-angstrom resolution [156]. A comprehensive textbook written by Williams and Carter covers most of the electron-microscopy related issues [152]. In this chapter, basic principles and components of (S)TEM will be introduced.

3.2 Interaction between electron beam and specimen

Electrons are charged particles and can be easily manipulated by electromagnetic fields. Having both wavelike and particle properties, gives electrons significant advantages. Wave-like behaviour allows electrons to form images and diffraction patterns that reveal internal structure of material, with a wavelength that can be tuned by their energy. Particle be-

haviour affects their electron-specimen interaction, making chemical analysis possible.

In general, there are two ways of grouping the electron scattering. The first one is between elastic and inelastic scattering, which are distinguished by detectable energy loss and is important to chemical analysis. The second way is between coherent and incoherent scattering, wherewith coherent scattering the waves can form interference pattern by phase differences, while in incoherent scattering they can not.

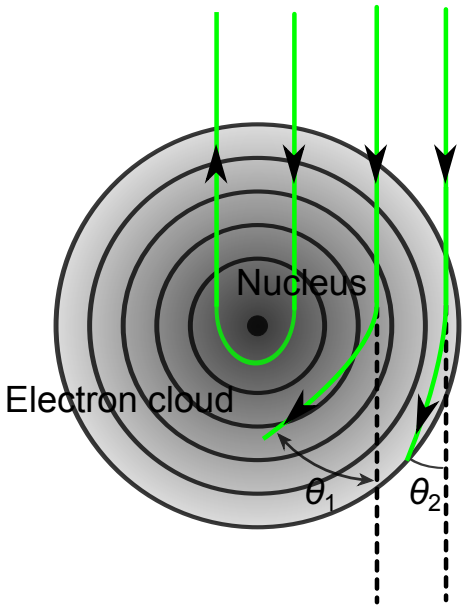

Figure 3.2: Electrons scattered by an isolated atom.

Elastic scattering usually occurs at the relatively small angles $(1-10°)$, in the forward direction. At higher angles, elastic scattering becomes more incoherent [152]. When it comes to addressing a particular problem, elastic scattering is normally considered into two mechanisms, scattering from individual atoms and from the whole specimen [152]. Figure 3.2 shows a schematic of electron scattering from an isolated atom. The Coulomb interaction within the electron cloud leads to low angle scattering, while Coulombic at-

traction by the nucleus cause higher angle scattering even back-scattering with angle more than 90° [152]. Ignoring scattering at low angle, the high angle electron-nucleus interaction is analogous to Rutherfold scattering. The following expression gives the differential cross section for high angle scattering by the nucleus alone [152],

$$\sigma_{\mathrm{R}}(\theta) = \frac{e^4 Z^2}{16(4\pi\varepsilon_0 E_0)} \frac{d\Omega}{\sin^4 \frac{\theta}{2}}, \tag{3.1}$$

where θ, E_0, Ω, Z and ε_0 are respectively the scattering angle, electron energy, solid collection angle, atomic number of the specimen and permittivity of free space, respectively. From Equation 3.1, it can be seen that higher atomic number leads to high differential cross section.

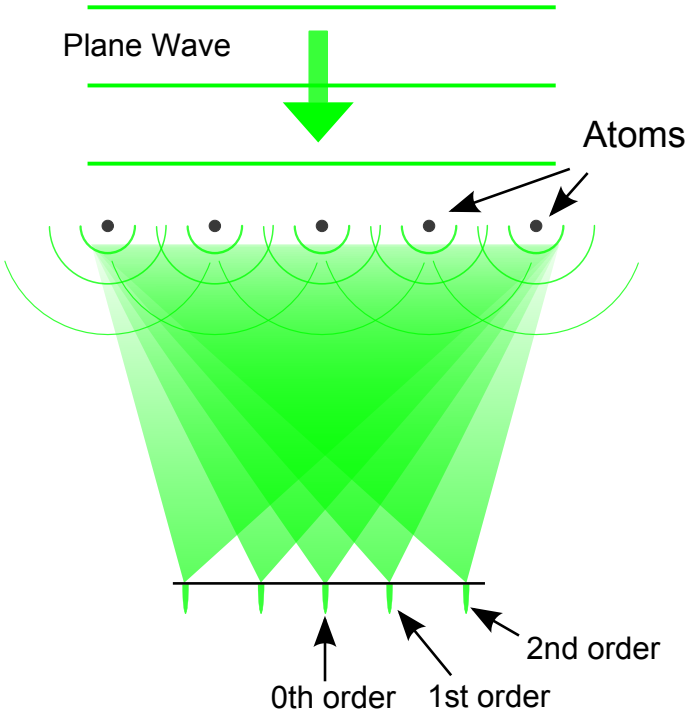

Figure 3.3: A plane, coherent electron wave passes through an array of atoms, resulting in direct (0th order) beam and several high order coherent beams diffracted at specific angle.

As shown in Figure 3.3, when the plane coherent electrons pass through the specimen, they are scattered to low angles by each atom, generating the secondary spherical wavelets that form a diffraction pattern at the back focal plane of the lens. The diffraction pattern contains the structure information.

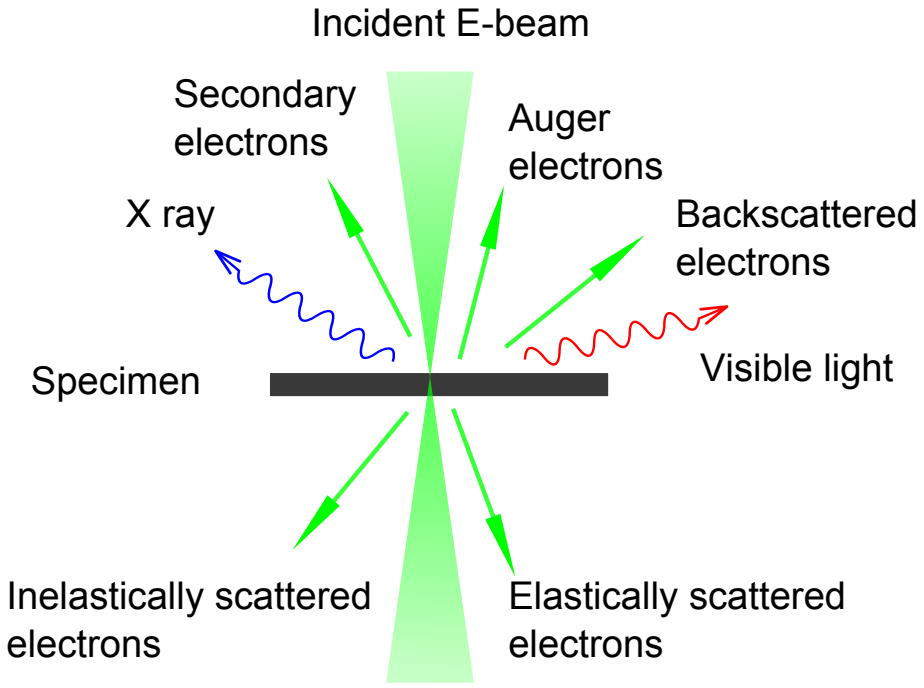

Figure 3.4: Interaction between electron beam and specimen.

Inelastic scattering is almost always incoherent. For the inelastic scattering, X-rays, secondary electrons, phonons, plasmons etc can be generated (Figure 3.4). There are two types of X-rays: Characteristic X-rays and Bremsstrahlung X-rays. Characteristic X-rays are emitted from heavy elements when their electrons make transitions between the lower atomic energy levels. It usually shows two sharp peaks and is useful for local elemental analysis of nano-structured materials and crystal defects. Bremsstrahlung X-rays are emitted when electrons are decelerated by a metal target and appear as background in

the spectrum. Secondary electrons are electrons within the specimen that are ejected by the electron beam. They can be produced from the conduction bands, valence bands and inner shells. Secondary electrons ejected from inner shells are normally referred as Auger electrons and result from an ionized atom returning to the ground state. The incident electron beam can also induce the excitation of lattice oscillations, or phonons. This kind of scattered electrons normally gives a uniform background. Plasmons are normally generated in metals where the outermost atomic electrons are loosely bound so that high energy incident electron can excite waves in the "free electron sea" [152].

3.3 The electron optics components in (S)TEM

The exact setup of the electron optics components may vary with different types of electron microscope or even different modes in the same electron microscope, but the main components used are the same, including the electron source, magnetic lenses and detectors. In this section they will be introduced briefly.

3.3.1 Electron gun

There are two kinds of electron source that are widely used in (S)TEM. The first is thermionic sources that generate electrons by heating. The other one is field emission guns (FEG) that generate electrons when an intense electric field is applied to them [152]. Schottky source combines both heating and field emission. The materials of electron source usually have high melting point or low work function, such as W, LaB_6, so that

conduction band electrons can easily escape from tip and into a vacuum [152]. The FEG generates more monochromatic electrons so that it is usually preferred in (S)TEM.

In brief, the FEG acts as a cathode with respect to two anodes [152]. The first anode provides the extraction voltage (several kV relative to the tip) to pull electrons out of the tip and the second anode accelerates the electrons (Figure 3.5). In addition, the second anode acts as an electrostatic lens to produce a crossover. This lens controls the effective source size and position, although it is not flexible. The surface of the tip needs to be free of contamination and oxide, so the gun is operating in ultra-high vacuum conditions. If the tip is operated in ambient temperatures, it is referred as cold FEG.

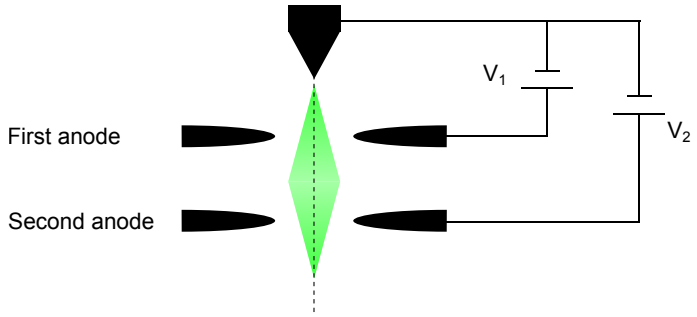

Figure 3.5: Schematic representation of FEG.

3.3.2 Magnetic lenses

Electrons can be focused by both electrostatic and magnetic lenses. However, in practice, magnetic lens has advantages in many respects, especially because it is not susceptible to high voltage breakdown [152]. The Lorentz force $\boldsymbol{F}$ that deflects an electron when it enters a magnetic field of strength $\boldsymbol{B}$ and an electric field of strength $\boldsymbol{E}$ with a velocity

$\boldsymbol{v}$, is as follows

$$\boldsymbol{F} = -e(\boldsymbol{E} + \boldsymbol{v} \times \boldsymbol{B}). \tag{3.2}$$

Equation 3.2 means that the electrons spiral through the round lens field with a helical trajectory.

Figure 3.6 shows a schematic diagram of a magnetic lens which consists of a coil of copper wires inside the soft iron pole piece. A current through the coils creates a magnetic field in the bore of pole piece [152]. The magnetic field is inhomogeneous. It is weaker in the centre and stronger close to the bore. Thus electrons passing through the centre are deflected less by the magnetic field that those far off the axis, providing the focusing power of the lens.

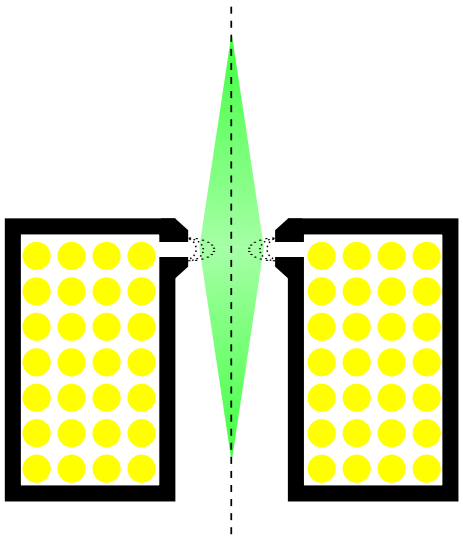

Figure 3.6: Schematic diagram of a magnetic lens.

For a thin lens forming an image of an object, without aberration, the ray diagram can be simply drawn as given in Figure 3.7. The electron rays pass through the lens from the

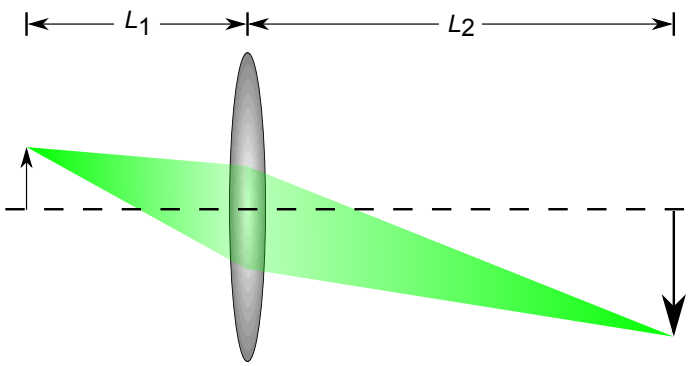

Figure 3.7: Raytracing for a thin lens.

object and are focused at the image plane. This principle also applies to electromagnetic lens even though in reality the electrons follow a helical path.

The distance between the object plane and lens (the object distance L_1) and the distance between lens and image plane (the image distance L_2) follow the lens equation,

$$\frac{1}{f} = \frac{1}{L_1} + \frac{1}{L_2}, \tag{3.3}$$

where f is the focal length of the lens. The magnification is defined as

$$M = \frac{L_2}{L_1}. \tag{3.4}$$

3.3.3 Aberration and aberration correction

In theory, a rotationally symmetric electromagnetic lens must be a convex lens. When a parallel electron beam passes through such a lens, positive spherical aberration is always generated, which means that the rays passing close to the optical axis (paraxial ray) are focused further than the rays away from the axis (Figure 3.8 (a)). This essentially blurs

the electron beam probe. To overcome this limitation in focusing a electron beam, an aberration corrector is inserted into the optical path, which acts as a negative aberration generator (Figure 3.8 (b)). There are two different types of correcting system commercially available, from Nion using multiple quadrupole and octupole lenses, and from CEOS using hexpole and other transfer lenses. The quadrupole-corrector system has the intrinsic advantage of compensation of the axial chromatic aberration but is more complicated in the sense of the number of non-rotationally symmetric lenses [162]. For the hexapoles correction system, a pair of hexpole lenses are placed at each side of a round lense doublet [163]. The primary non-rotationally symmetric secondary-order aberrations of the first hexapole are compensated by the second hexapole element. At the same time, a residual secondary third-order spherical aberration which is rotationally symmetric is induced, due to hexapoles non-linear diffraction power [164]. The sign of the coefficient of spherical aberration is opposite to that of the objective lens. In other words, the electron beam is pre-diverged by the usage of corrector, which compensates for the aberration of the objective lens located after the corrector.

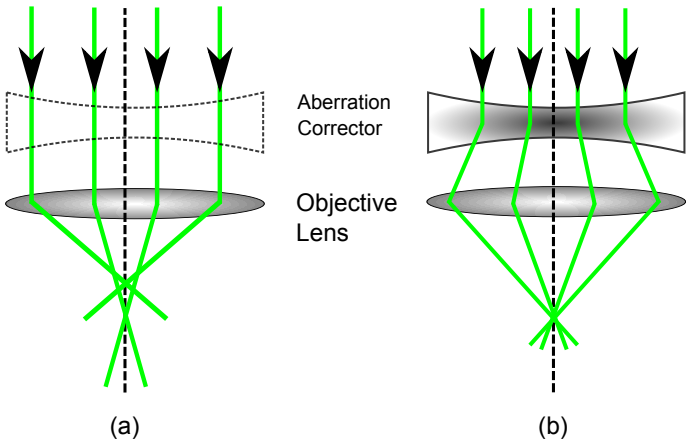

Figure 3.8: Schematics of a convex lens (a) without and (b) with aberration corrector.

3.3.4 Detectors

The electrons are invisible to human eyes. In (S)TEM, a viewing screen is placed in the viewing chamber, made of doped ZnS so that it gives off green fluorescence when electrons hit it, so they are visible to human eyes. Electrons can also be detected using semiconductor detectors, scintillator-photomultiplier detectors/TV cameras, charge-coupled device (CCD) detectors, and Faraday cups. In this work, most of the characterisation is done by ADF detector which is made of scintillator-photomultiplier and coated with Al [152].

Figure 3.9 illustrates the principle of how ADF detector works. When the incident electrons hit the scintillator, photons are generated, which induce the photoelectric effect at the entry of the photomultiplier tube (PMT). Successively the electrons are multiplied at different dynodes in the photomultiplier. The gain of photomultiplier can achieve up to 10^8. The scintillator can not be made of ZnS as the viewing screen because the decay time is too long (microseconds). Normally the scintillator is made of Ce-doped yttrium-aluminium garnet to achieve the nanoseconds decay time [152]. Bright field (BF) detection works in the same way, but with slight different detector geometry using a round

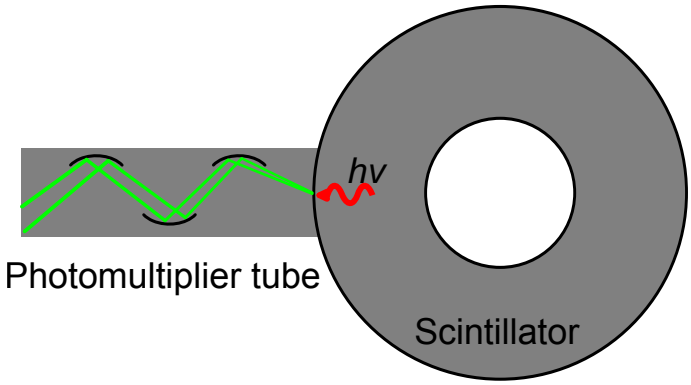

Figure 3.9: Schematic of ADF detector composed of scintillator and photomultiplier tube.

detector collecting the direct electron beam, instead of annular detector. The electron collection angle of both ADF and BF can be adjusted by the post-specimen electron optics, e.g., camera length. Particularly for ADF detector, when it collects high angle scattered electrons, it is called high angle annular dark field (HAADF) detector. However, the exact "high angle" is not well-defined in the literature.

Some microscopes are equipped with EDX detectors. The most advanced detector is called silicon drift detector, or SDD for short, which is basically a CCD consisting of concentric rings of p-doped Si implanted on a single crystal of n-Si across which a high voltage is applied to pick up the electrons generated as X-rays enter the side opposite the p-doped rings [152]. This analytical technique sometimes can be very useful particularly to distinguish the elements with similar atomic numbers. For example in Figure 3.10 (a) shows a HAADF-STEM image of Au nanorod coated with Pt where Au and Pt can not be distinguished solely from the HAADF-STEM image because they have close atomic numbers, 79 and 78 respectively. By mapping the EDX signals, the chemical composition

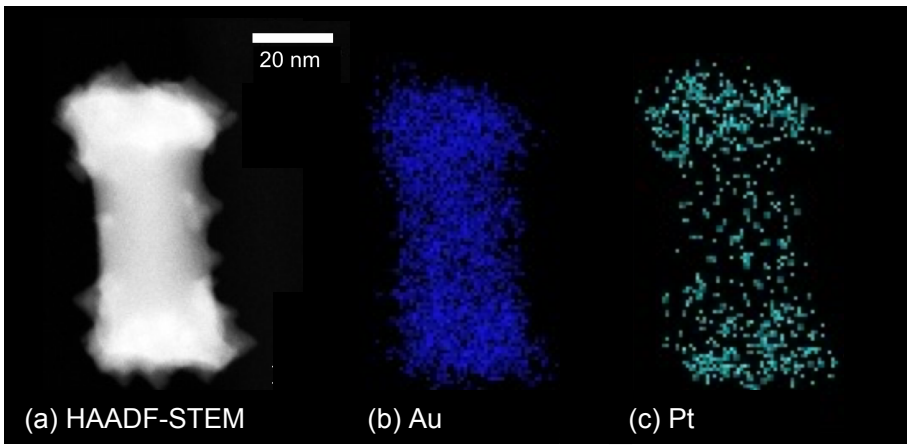

Figure 3.10: (a) HAADF-STEM image of a Pt coated Au nanorods. (b) and (c) are corresponding Au and Pt EDX mapping. This figure is adapted from [165]

distribution can be determined, shown in Figure 3.10 (b) and (c). It can be seen that the Pt is not uniformly deposited on the Au nanorods but prefers the ends [165].

3.4 Vacuum system

All electron microscopes has to be operated in vacuum and contamination in the vacuum mainly derives from hydrocarbons [166]. Contamination during imaging occurs when hydrocarbon molecules are polymerised by electron beam, so is related to the current density. By making use of synthetic oils and appropriate traps on the pump, the contamination of residual hydrocarbons from pump oil has been reduced to satisfactory levels for TEM [152]. However, the small probe used in convergent beam electron diffraction (CBED) or STEM results in strong local electron beam, thus contamination is more of an issue. There are two means for contamination to reach the irradiate area, (1) directly from residual gas and (2) by surface diffusion from neighbouring regions. Normally the latter one dominates in the case of small probe illumination [167].

There are many ways of minimising contamination. Anti-contamination device (ACD) cooling (using liquid nitrogen) can reduce the residual gas in the vicinity of the specimen [168]. It can also be helpful to use plasma cleaning which bombards the surface of the sample with energetic electrons and ions to break the C-H bonds so to have a clean sample to start with. In practice, beam-showering the region of interests with strong dose but large coverage of beam is often applied to pin the contamination to its local area and avoid diffusion during imaging.

3.5 Image Formation

Images in (S)TEM are dominated by three types of contrast [169]: amplitude contrast, phase contrast and mass thickness (atomic number) contrast. The amplitude contrast is caused by the defects (local strain/defects/dislocation), perturbating the amplitude of the Bragg reflected beams. The phase contrast is the modulation of the incident electron wave when it transmits through the crystal potential. This type of contrast is sensitive to the atom distribution in the specimen. The mass thickness (atomic number) contrast is originated from that fact that atoms with different atomic number has different power to scatter electrons.

According to the contrast mechanism, there are two reciprocal ways of forming high resolution image in (S)TEM: (1) TEM images, which are resulted mainly from the phase contrast and (2) ADF-STEM images, which are formed by collecting the scattered electrons. In TEM mode, the electron illuminates the sample with parallel beam. The electron beam in STEM is focused to a sharp point and rasters across the sample surface. The image and source point can be exchanged in TEM and STEM.

3.5.1 TEM image formation

The TEM image formation mechanism and its application in nanotechnology have been reviewed By Wang [169]. Figure 3.11 shows a simplified TEM image formation system with only one objective lens. The specimen is illuminated by a (nearly) parallel electron beam, which is diffracted by the crystal lattice and forms Bragg beams propagating along

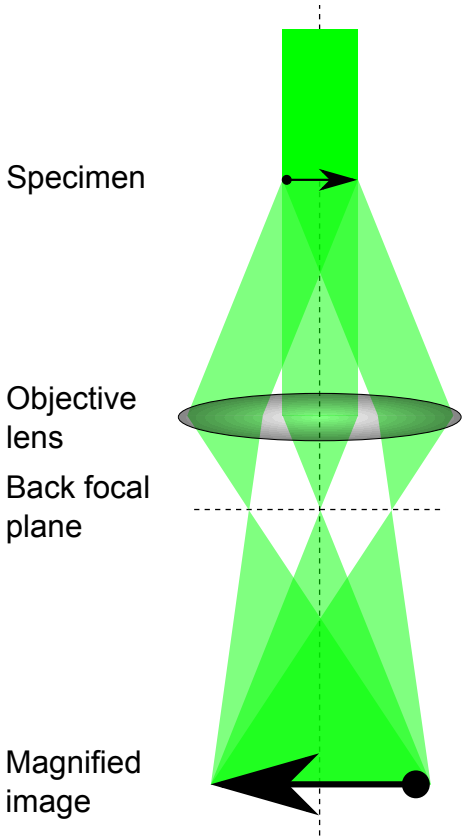

Figure 3.11: Schematic of TEM image formation with one lens.

different directions. The quantum mechanical diffraction theory determines the phase and amplitude change of the electron wave during the electron-specimen interaction [169]. The exit surface wavefunction, $\Psi(\mathbf{r})$, which contains the full structural information on the specimen, is magnified by the objective lens (and further lenses) to form a highly magnified image. A diffraction pattern is formed at the back focal plane by the focused diffracted beams. Mathematically, the diffraction amplitude function at the back focal plane (diffraction plane) is

$$\psi'(\mathbf{u}) = \psi(\mathbf{u}) \exp[i\chi(\mathbf{u})], \tag{3.5}$$

where $\psi(\mathbf{u})$ is the Fourier transform of the wave $\Psi(\mathbf{r})$ at the exit face of the specimen and $\mathbf{u}$ is the reciprocal space vector that is related to the scattering angle [170]. $\chi(\mathbf{u})$ is the phase shift determined by the spherical aberration coefficient C_s of the objective lens and the lens defocus Δf,

$$\chi(\mathbf{u}) = \frac{\pi}{2} C_s \lambda^3 \mathbf{u}^4 - \pi \Delta f \lambda \mathbf{u}^2, \tag{3.6}$$

where λ is the electron wavelength. Thus, the observed image intensity is

$$I_{coherent}(\mathbf{r}) = |FT^{-1}[\psi'(\mathbf{u})]|^2 = |\Psi(\mathbf{r}) \bigotimes t_{obj}(\mathbf{r}, \Delta f)|^2, \tag{3.7}$$

where $\bigotimes$ indicates a convolution calculation, and $t_{obj}(\mathbf{r}, \Delta f)$ is the inverse Fourier transform of the phase function $\exp[i\chi(\mathbf{u})]$ [169]. Equation 3.7 correlates the object wave function $\Psi(\mathbf{r})$ with the experimentally observed image intensity distribution $I_{coherent}(\mathbf{r})$.

For a thin crystal, the electron transmission can be approximated to be only modulated in phase, not in amplitude, i.e. the phase object approximation. In this approximation, when the electrons go through a crystal potential field, their kinetic energy is perturbed by the variation of the potential field, resulting in a phase shift with respect to the electron wave that travels in a space free of potential field [169]. For a specimen of thickness, d_{cry}, the phase shift is approximately

$$\frac{\pi}{\lambda V} V_p(\mathbf{r}) = \frac{\pi}{\lambda V} \int_0^{d_{cry}} V(\mathbf{r}, z) \mathrm{d}z, \tag{3.8}$$

where V and $V_p(\mathbf{r})$ are the acceleration voltage and the thickness-projected potential of

the crystal,respectively. Equation 3.8 shows that the phase contrast image is the thickness projected image along the beam direction (z-axis) of a three dimensional object. The 3-D shape of the crystal can be revealed using the images recorded from at least two independent orientations. For a thin crystal, the electron transmission can be approximated to be only modulated in phase, not in amplitude, i.e. the phase object approximation. At the exit face, the electron wave is described as

$$\Psi(\mathbf{r}) = \exp[i\sigma V_p(\mathbf{r})]. \tag{3.9}$$

If the incident travel along a low-index axis, the variation of $V_p(\mathbf{r})$ across atom rows is a sharply varying function (0.02-0.03 nm), as the width of the potential of an atom is narrow [169]. This sharp phase variation is the basis of phase contrast analysis, the fundamental principle of atomic resolution imaging in TEM. This technique needs a highly coherent source and is also known as coherent imaging. Contrast can be reversed by the thickness of the specimen.

3.5.2 STEM image formation

Image formation in STEM is different from coherent TEM imaging, as it employs a focused electron beam to scan across the specimen (Figure 3.12). The illuminating STEM probe wavefunction $p(\mathbf{r})$, is a sum over all the partial plane waves,

$$p(\mathbf{r}) = \int \mathrm{A}(\mathbf{u}) \exp[-i2\pi\mathbf{u}\cdot\mathbf{r}]d\mathbf{u}, \tag{3.10}$$

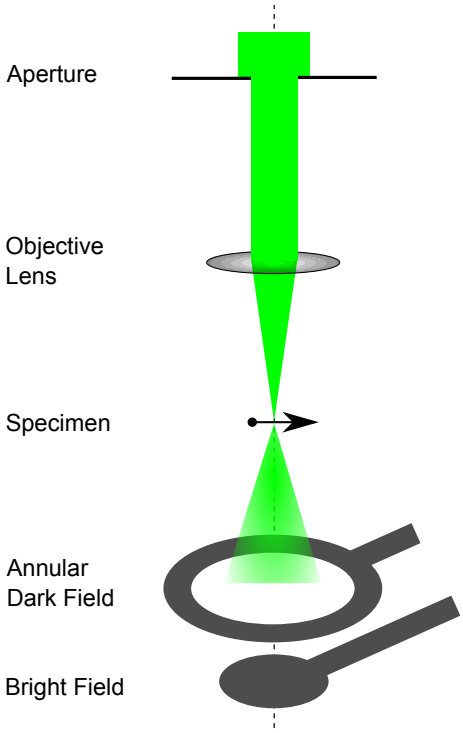

Figure 3.12: Schematic of the principle of STEM.

where the complex aperture function

$$\mathrm{A}_c(\mathbf{u}) = \mathrm{H}_c(\mathbf{u}) \exp[i\chi(\mathbf{u})], \tag{3.11}$$

where $\mathrm{H}_c(\mathbf{u})$ is a circular top-hat function with unit height. The phase shift $\chi(\mathbf{u})$ is dependent on the objective lens aberrations, which can include not only the rotationally symmetric aberrations such as defocus and the spherical aberration of the third and the fifth order but also non-symmetric aberration such as astigmatism and coma.

When the specimen is illuminated from a wide range of angles, it can be treated as a self-luminous object. This technique is usually referred as incoherent imaging and can be mathematically modelled as a convolution in intensity rather than a complex amplitude

[171]

$$I_{incoherent}(\mathbf{r}) = |p(\mathbf{r})|^2 \bigotimes |O(\mathbf{r})|^2, \tag{3.12}$$

where $O(\mathbf{r})$ is the specimen object function (the projected potential).

As can be seen in Equation 3.12, the image resolution of the image is largely dependent on the probe function. After years of the development of STEM, it can now achieve atomic resolution. The advantage of the this technique is that atomic column intensity increases monotonically with increasing thickness, with no contrast reversal up to very large thickness, so the data is more direct interpretable and relatively less dependent on focus [171].

In terms of interpreting the ADF images, the Rutherford scattering model is normally used to assume that the scattered electrons collected by the ADF is proportional to Z^2. However, because the screening effect at low angles, the power exponent ranges from 1.5 to 2.0, depending on the camera length used in the experiment [172]. Initially, the signal collected by ADF detector was assumed to derive from elastically scattered electrons and shows strong atomic number (Z) contrast [173]. Later work showed that if any coherent scattering Bragg beams were incident on the ADF detector, the contrast could not purely be related to atomic number [174]. Therefore, caution must be taken in quantitatively interpretating the intensity of the ADF-STEM image.

3.5.2.1 The incoherence and coherence in ADF-STEM

The most important feature in STEM is incoherence. This brings the direct interpretation of the image and the doubling the resolution than TEM. As classified by Nellist and Pennycook, there are two aspects [173]: transverse incoherence and longitudinal coherence.

The transverse incoherence is that the peaks in the ADF-STEM image only correspond to the atomic columns that have been scanned. When the electron beam passes through the specimen, it will lead to the Bragg beam disk underneath and this may cause the intensity contributed from neighbouring columns. This can be avoided by simply increasing the collection angle of the detector. It has been suggested by Hartel et al. that the inner collection angle should be at least three times larger than the convergence angle [175], so that even the Bragg beam can lead to the transverse incoherence.

The longitudinal coherence is more complicated, resulted from the interference from the same atomic column ("intra-column interference"). The geometry of the detector plays less important role in breaking the longitudinal coherence than the transverse coherence [173]. It was suggested to use the thermal diffuse scattering (TDS) to break the intra-column coherence [174]. However, with calculation, it shows that the signal that ADF detects is a combination of the TDS electrons and coherent scattered Bragg beams, which leads to a non-linear relationship between intensity and thickness. Importantly, the calculation shows that the intensity-thickness has no contrast reversals [173]. Thus, in principle, if a calibration curve is obtained the non-linearity of intensity-thickness can be corrected.

3.6 Summary

To characterize the three dimensional structures of nanoclusters, the tomography is the best choice as it can look at the nanoclusters from different direction. However, this requires the stability not only from the (S)TEM instrument, but also from the nanoclusters. For those nanoclusters that are small enough, their intrinsic structure instability sets constrains to the measurement time, and also electron beam current used. The HAADF-STEM imaging has much better advantage than TEM imaging when studying three dimensional structures of nanoclusters. First, STEM has better contrast if the sample is deposited on the light element substrate such as carbon. This contrast is approximately quadratic increased in HAADF-STEM. Second, the intensity is directly interpretable and less dependent on the defocus condition. This makes observer easier to recognize the structure in a real space. Third, the intensity means something! As the intensity generally increases as a function of the sample thickness. With the quantitative technique, once the intensity-thickness calibration curve is obtained, the intensity can be used to count atoms in a cluster/atomic column thus the three dimensional information of clusters can be obtained.

Chapter 4

Experimental quantification of JEOL 2100F

4.1 Introduction

With the sophistication of the software, hardware and after-sale service, the commercial microscope is more friendly to use. However, using the microscope blindly is dangerous. It can lead to misinterpretation of the data. On the other hand, direct comparison between experimental images and simulated images requires quantification of the microscope in use. In this chapter, the pixel size, convergence and collection angles, and the response of the annular dark field (ADF) detector in JEOL 2100F microscope, which is located in the University of Birmingham, are investigated practically. The approach to quantify the ADF detector used in this thesis has been published in 2013 Electron Microscopy and Analysis Group conference proceedings.

4.2 Overview of JEOL 2100F

The aberration corrected scanning transmission electron microscope (STEM), installed in Nanoscale Physics Research Laboratory, University of Birmingham in 2009 is a standard

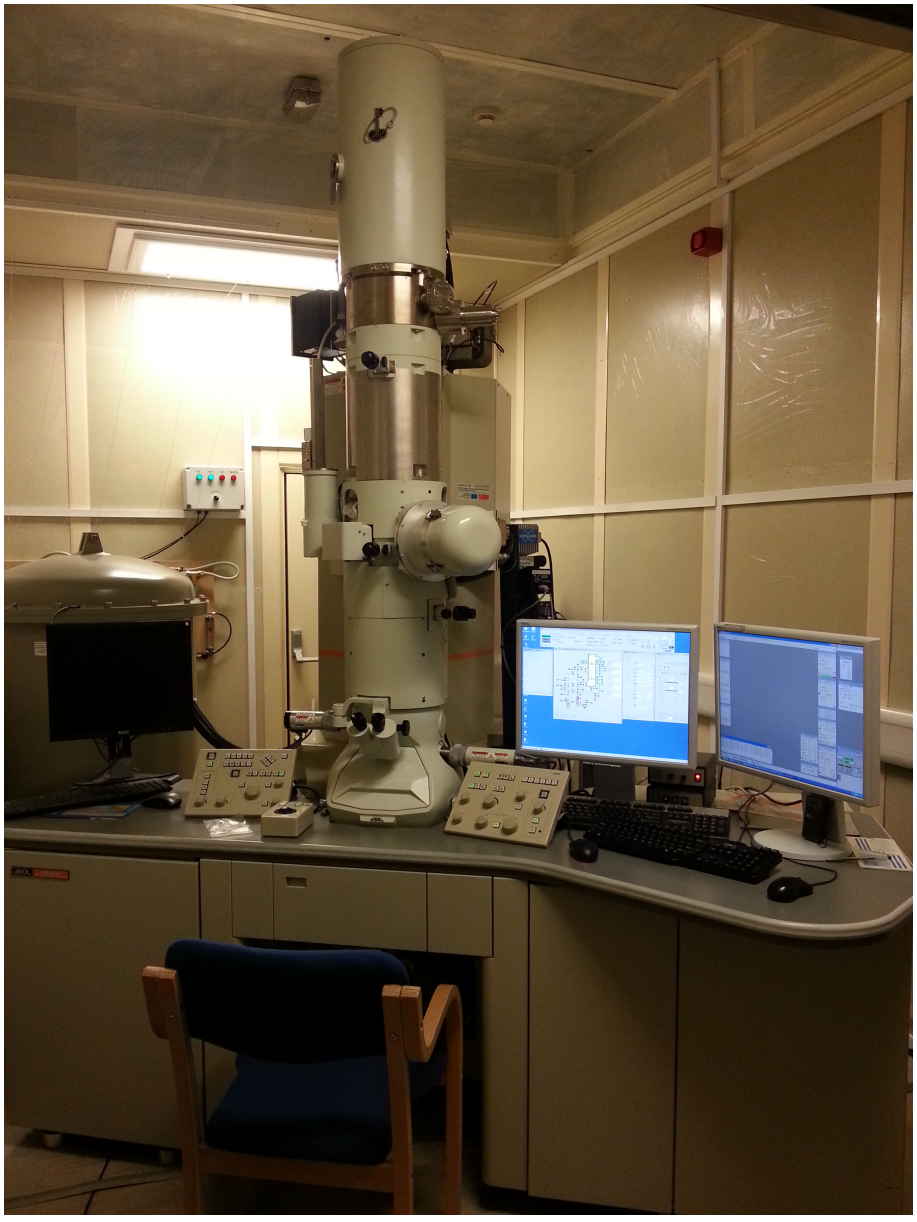

Figure 4.1: Aberration corrected JEOL 2100F microscope located in the University of Birmingham.

JEOL 2100F STEM, fitted with a CEOS aberration correction system, which corrects spherical aberration up to the fifth order (Figure 4.1). The microscope can operate in both transmission electron microscope (TEM) and STEM modes and has an acceleration voltage of 200 kV. It is equipped with both JEOL and Gatan bright field and dark field detectors, Gatan TEM charge coupled device (CCD), electron energy loss spectrometer (EELS) and Bruker energy dispersive X-ray (EDX) detector. For the high angle annular dark field (HAADF) -STEM imaging, normally the JEOL dark field detector is used, whose brightness and contrast can be more readily controlled using JEOL software. It is physical located above the Gatan bright field, which allows the two detector to be used simultaneously.

The electrons are generated by the field emission gun (FEG) which is made of a sharp tungsten tip with (100) face normal to the optical axis with a layer of ZrO on top to reduce the work function barrier. The tip works in vacuum pressure of the order of 10^{-10} mbar. The FEG is heated to aid emission and avoid contamination. The electrons extracted are accelerated to high energies using an electrostatic accelerator.

After the electrons leave the electron gun, they pass through a 3 stages lens system, an aberration corrector and reach the specimen. The vacuum in the specimen chamber is about 2×10^{-7} mbar. The aberration correction system is driven by the CESCOR software. In this study, the nanoparticles or clusters were deposited onto standard commercial TEM Cu grids, with a diameter of 3 mm and coated with an amorphous thin carbon film. The sample stage can be tilted $\pm21^{\circ}$ in both X and Y directions with respect to the electron beam to get information from sample in different orientations. The area surrounding the

sample is cooled by the liquid nitrogen to reduce contamination.

4.3 Calibration of pixel size

The pixel size is crucial to nanomeasurement in STEM. To calibrate it, an MgO crystal was used as a standard, which has lattice constant 0.421 nm [176]. Figure 4.2 (a) is an image showing a part of the MgO crystal, taken at magnification of 15 M× from the [001] zone axis and convoluted by Gaussian with 2 pixels. The inset is the FFT pattern of this image. Both the direct image and the FFT shows square patterns that are characteristic feature of this orientation. Figure 4.2 (b) and (c) show the line profile taken as indicated by A and B in (a). In both (b) and (c) there are 11 peaks (indicated by the red arrows) which

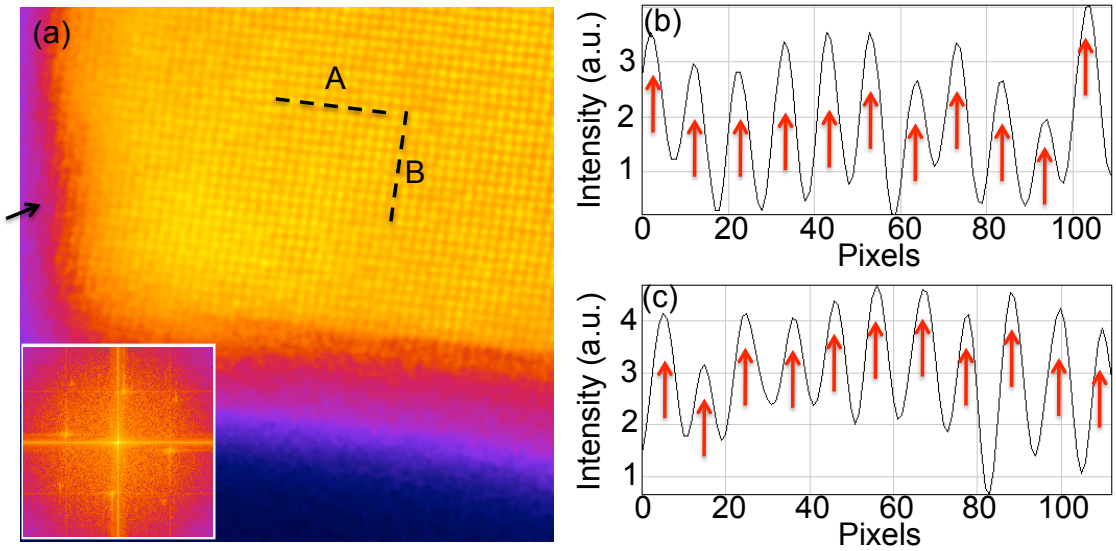

Figure 4.2: (a) HAADF-STEM image of 15 M× magnification with 512×512 pixels (filtered using Gaussian blurring with 2 pixels). The inset shows the FFT. (b) The line profile of the region A indicated in (a). (c) The line profile of the region B indicated in (a). Both (b) and (c) have been averaged over 10 pixels to reduce the noise.

correspond to 11 atomic columns. The distances across these 11 peaks are representing 105 and 103 pixels, respectively. Averaging the distances between adjacent columns gives respectively 10.5 and 10.3 pixels between peaks. In FCC crystals, the distance between the adjacent columns at [001] direction is half of the lattice constant, i.e. 0.211 nm in the case of MgO. Thus the pixel sizes are 2.01×10^{-2} and 2.05×10^{-2} nm respectively. As it can be seen here, the difference between orthogonal directions is small ($\sim$ 0.9%). Taking the average of these gives 2.03×10^{-2} nm as the pixel size, and so 10.39 $\pm$ 0.10 nm is the image length for 512×512 pixels. Using the same method, the pixel sizes for magnification from 6 to 30 M× were determined. For lower magnification (less than 6M) atomic columns are not visible so the feature of damaged part of the crystal by electron beam (visible at the corner of the MgO in Figure 4.2 (a) indicated by the black arrow) and the length of the MgO cubic were used to determine the pixel size. Table 4.1 lists the pixel sizes and image sizes (512×512 scanning window) for the different magnifications shown on the microscope.

Table 4.1: Calibration of the pixel size and image size

Magnification	Pixel size	Image size
30 M×	$(1.06 \pm 0.01) \times 10^{-2}$ nm	5.40 ± 0.05 nm
20 M×	$(1.61 \pm 0.03) \times 10^{-2}$ nm	8.26 ± 0.16 nm
15 M×	$(2.03 \pm 0.02) \times 10^{-2}$ nm	10.39 ± 0.10 nm
10 M×	$(3.14 \pm 0.05) \times 10^{-2}$ nm	16.09 ± 0.23 nm
6 M×	$(5.14 \pm 0.13) \times 10^{-2}$ nm	26.31 ± 0.64 nm
4 M×	$(7.66 \pm 0.19) \times 10^{-2}$ nm	39.23 ± 0.95 nm
1 M×	$(2.45 \pm 0.06) \times 10^{-1}$ nm	125.54 ± 3.05 nm
600 k×	$(4.09 \pm 0.10) \times 10^{-1}$ nm	209 ± 5 nm
300 k×	$(8.24 \pm 0.21) \times 10^{-1}$ nm	421 ± 10 nm
100 k×	1.98 ± 0.05 nm	1.01 ± 0.02 micron
50 k×	4.89± 0.12 nm	2.50 ± 0.06 micron

4.4 Calibration of convergence angles and inner collection angles

In ADF-STEM mode, the combination of convergence angle and collection angle can give different information about the sample. For example, when small collection angle is used, the electrons collected by the ADF detector are more likely to be influenced by the Bragg beam, while using bigger collection angle they are more likely to be influenced by thermal diffuse scattering (TDS) electrons. In this work, in STEM mode, the convergence angle of the aperture and the collection angle of the ADF detector was calibrated using convergent beam electron diffraction (CBED) of a gold nanorod. Figure 4.3 (a) shows the diffraction pattern of Au nanorod along the [001] zone axis. 20 cm camera length in the microscope was used and the lens CL1 current was set to C100 with spot size 8C shown

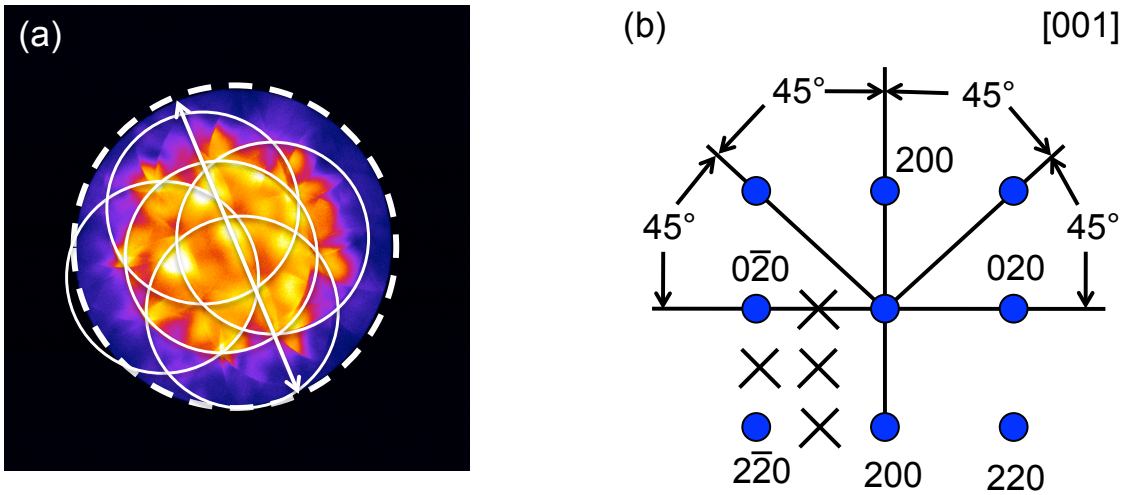

Figure 4.3: (a) The electron diffraction of a Au nanorod from [001] zone axis. The solid circulars indicate the diffraction spots and the dashed line indicated the shadow of the ADF detector. (b) An ideal electron diffraction pattern.

in the JEOL software. In Figure 4.3 (a) the dashed circle indicates the shadow of the ADF detector and the solid circles with the same size indicate the diffraction spots. The ratio between the diameter of the dashed line and the diameter of the solid circle is equal to the ratio between inner collection angle to the convergence angle based on the small angle approximation ($\sin x \approx x$ when the angle x is small). Figure 4.3 (b) shows the ideal indexed diffraction pattern from this direction. Some spots such as 100 are forbidden in the FCC structure for the reason of the structural factor (indicated by the cross symbols). The distance between adjacent (hkl) lattice planes is

$$d_{hkl} = \frac{a}{\sqrt{h^2 + k^2 + l^2}}, \tag{4.1}$$

where a is the lattice constant, and h, k and l are the Miller indicies of a family of lattice planes. Using the Bragg's equation, $2d_{hkl} \sin\theta = \lambda$, where λ is the wavelength, it is possible to obtain the angle between the central spot and the nearest spot. The inner collection angle can then be deduced as 31.5 mrad. Use this as a reference, other inner collection angles and convergence angles was obtained as shown in Table 4.2.

Table 4.2: Convergence angle and inner collection angle

Convergence angle[2]	Condenser Aperture 3	19.2 mrad
	Condenser aperture 4	14.0 mrad
Inner collection angle [2]	CL 20 cm	31.5 mrad
	CL 10 cm	57.0 mrad
	HAADF 3	83.9 mrad
	HAADF 4	109.0 mrad

[1] Condenser Aperture 4 is the smallest condenser aperture and Condenser Aperture 3 is the second smallest condenser aperture in the microscope.
[2] Shown in the JEOL software.

4.5 The beam dose

The beam dose is an important parameter in the microscope when studying effects of the electron beam with nanoclusters. Normally in the microscope, the electron beam current can be measured from either the CCD detector or the small fluorescent viewing screen as long as they are well calibrated. A Faraday cup is also a possible option to measure the absolute vale of the electron beam dose, however it is not widely installed.

The CCD detector installed in this microscope is a Gatan US1000, with Phosphor scintillator (P47) on top of it. It detects the electrons and converts them into counts. The conversion factor provided by the manufacturer, Gatan, is 0.266 electrons/count. Figure 4.4 shows the counts as a function of the exposure time for the Gatan CCD in

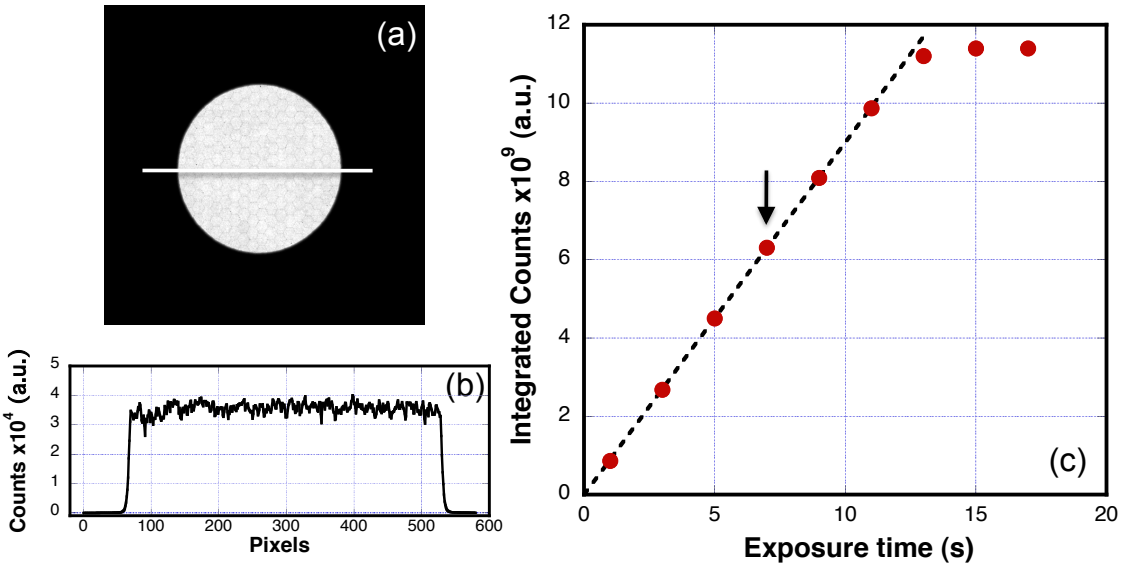

Figure 4.4: The linearity of Gatan CCD as a function of exposure time. (a) An example image when the electron beam hits the CCD directly. (b) The line intensity profile indicated in (a).(c) The total number of counts within the spot as a function of exposure time. The dashed line is the line fitting ($y = ax$) upto t=11 s.

which the linearity can be seen.

Figure 4.4 (a) is an example image when the electron beam hits the Gatan CCD directly with 7 s exposure time. The line profile in Figure 4.4 (b) shows that the beam is uniform, and that the detector has a good signal/noise ratio as the background level is very low. At this exposure time, the CCD is not saturated by the electron beam, as indicated by the arrow in Figure 4.4 (c). The integrated intensity of the spot over the exposure time after background subtraction is plot out in Figure 4.4 (c). The dashed line is a linear fit with the function of $y = ax$ for exposure time up to 11 s. The fit function passes through the origin. This shows that the CCD count is very linear with exposure time (and thus number of the electrons) before it gets saturated, which occurs at 65000 counts for each pixel. Thus the offset of the CCD detector is appropriate and the beam current can be obtained by dividing the total number of electron hitting the CCD (counts $\times$ 0.266) by exposure time.

Table 4.3: The typical electron beam current value[1] acquired using Gatan CCD and the small fluorescent screen

Spot size	Aperture[2]	Gatan CCD beam current	Small screen current
10C	4	5.6 pA	0 pA
10C	3	11.5 pA	7 pA
9C	4	8.4 pA	4 pA
9C	3	17.9 pA	13 pA
8C	4	16.5 pA	12 pA
8C	3	35.1 pA	30 pA
7C	4	24.5 pA	19 pA
7C	3	52.9 pA	46 pA
6C	4	50.1 pA	42 pA
6C	3	108.3 pA	96 pA

[1] Measured with emission current of 138 μA.
[2] 4 is the smallest condenser aperture and 3 is the second smallest condenser aperture in the microscope.

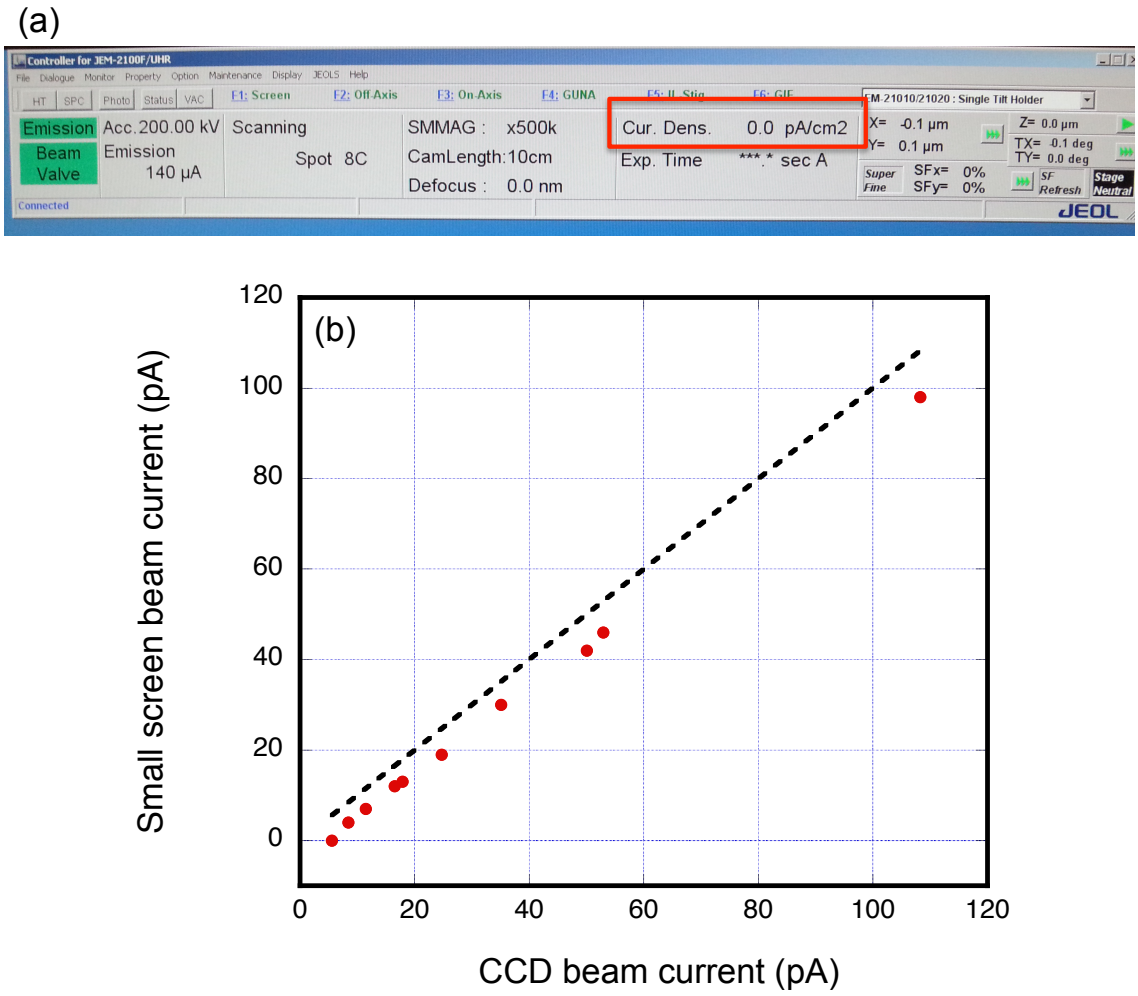

Figure 4.5: (a)The screen snapshot of the microscope control software. The beam density can be read in the red rectangular. (b) The red points are the beam current worked out from the small screen as a function of the beam current worked out from the Gatan CCD. The dashed line is the 1-1 function.

The small fluorescent screen can be used for viewing the electron beam as well as measuring the beam density. If the screen has been calibrated carefully, the beam density can be read from the TEM controller application (labelled with red box in Figure 4.5 (a)). It was suggested by the JEOL engineer that multiplying the beam density by 10 cm^2 gives the beam current. The beam current can be tuned by varying the spot size and the aperture. Table 4.3 shows typical values of the beam current measured using the small

screen and the Gatan CCD. The CCD beam current was worked out using the method described above. 0.5 s exposure time was used to avoid CCD saturation. These data are plotted in Figure 4.5 (b) (red dots), with the dashed line showing the 1-1 ($y = x$) for the guidance to eye. Figure 4.5 shows that the data points and the dashed line have similar trend (slope) but are offset differently. This means that (1) the gains of both Gatan CCD and JEOL small screen are set appropriately; (2) the offset of the small screen is slightly off because the Gatan CCD's offset is correct as shown in Figure 4.4. Nevertheless, the conversion factor of Gatan CCD is confirmed from the viewing screen. In the following work, the beam current is worked out from the Gatan CCD.

4.6 The response of the ADF detector

The ADF detector is also an electron dose detector, but works much faster than the Gatan CCD. To compare the electrons scattered by the specimen on to the detector in terms of the percentage of the total incident beam, the performance of ADF detector is crucial and has been the subject of more attention recently. The response of the ADF detector is normally non-uniformly distributed [177], and the brightness and contrast of the preamplifier, which are controlled by the JEOL software, can also change the count obtained. This makes the interpretation dependent on many experimental parameters, all of which must be considered to understand the performance of the ADF detector.

For this particular microscope, the ADF detector is a ring-like detector, made of P47 Phosphor scintillator with inner diameter of 3 mm and outer diameter of 8 mm. When

the electrons hit the scintillator, photons are generated. Photons travel through the waveguide by reflection. When the photons reach the photomultiplier tube (PMT), the signal carrier transforms from photons to electrons. At the latter stage the electronic signal is then adjusted by the pre-amplifier and eventually turns into counts.

4.6.1 Brightness and contrast

Both the brightness and contrast of the pre-amplifier can change the image count and controlled by the JEOL software. Figure 4.6 shows the count of the detector as a function of beam current, generated by directly focusing the electron beam on it with different brightness and contrast (lenses setting in STEM mode: IL1 621F, IL2 9777, IL3 8C8A, PL FA00 and appropriate defocus). Figure 4.6 (a) shows an example of the count mapping when the electrons hit the detector directly. The response is non-uniform, with the left-upper region near the inner boundary having the highest output count and the right-lower region near the outer boundary having the lowest output count. To understand this in more detail, the highest, intermediate and lowest response rate are investigated as a function of beam current indicated respectively by the black dot, red square and blue diamond in Figure 4.6 (a). The results are shown in Figures 4.6 (b1-5) and (c1-5) with the same coloured symbols. The beam current was varied using different combinations of spot sizes and apertures.

Figures 4.6 (b1-5) and (c1-5) show that in general for each position, there are three operating regions: a region that has no counts when the electrons hit the detector (cut-off region), a region where the output count is linear with the incident beam current (linear

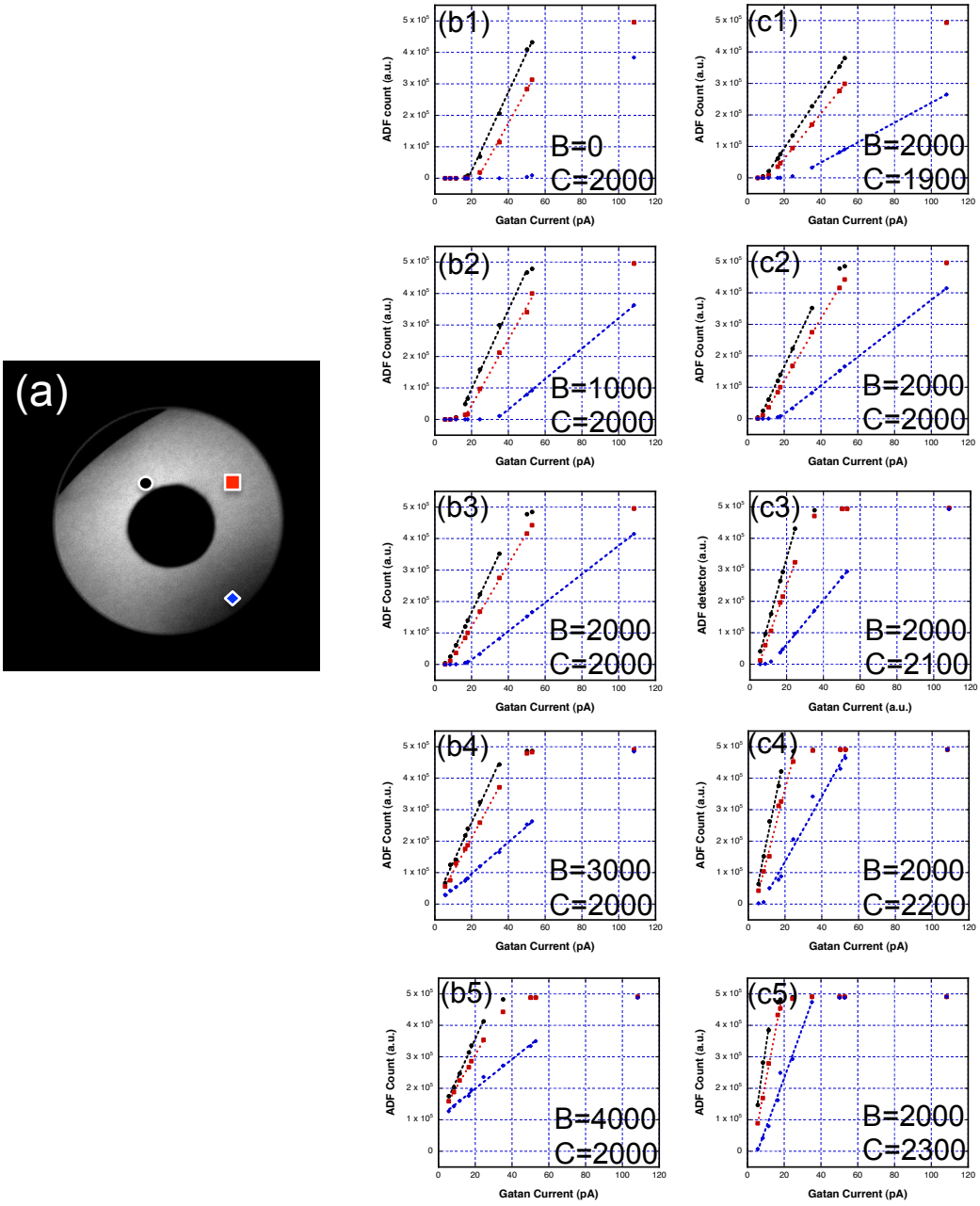

Figure 4.6: The performance of ADF with different brightness and contrast setting of the pre-amplifier. (a) An example of the non-uniformity of the detector. The positions indicated by black dot, red square and blue diamond are investigated in detail in (b1-5) and (c1-5) with the same coloured symbol. (b1-5) The counts against the incident beam current with varying brightness from 0 to 4000. (c1-5) The counts against the incident beam current with varying contrast from 1900 to 2300. The dashed lines are the linear fits.

region, fitted with lines) and a region where the count is saturated (saturation region). Operating in both the cut-off region and the saturated region leads to distortion of the linearity of the data, which should be avoided. However, even within the linear region in Figure 4.6, it is not straightforward to understand how brightness and contrast affect the parameters of the linearity such as intercepts and slopes.

To better understand the effect of the brightness and contrast, three parameters of the linear fitting shown in the Figure 4.6 (b1-5) and (c1-5), are considered in further

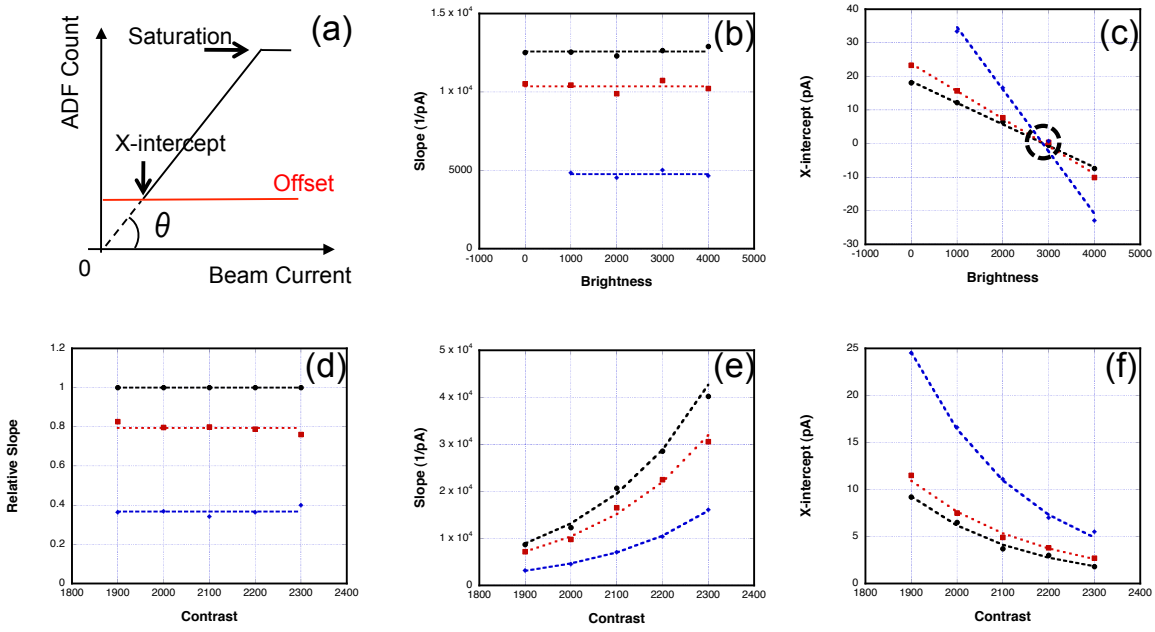

Figure 4.7: (a) A schematic of the ADF response as a function of beam current. (b) The slope as a function of brightness at contrast =2000. (c) the X-intercept as a function of brightness at contrast=2000. The circle shows that at this brightness setup the counts reach zero at the same time for different regions. (d) the relative slope as a function of the contras at brightness =2000. The slope has been scaled to the value of the highest slope. (e) The slope as a function of contrast at brightness=2000. (f) The X-intercept as a function of contrast at brightness =2000. In (b-f), the data points are from experiment and the dashed curves are fits. Black dots, red square and blue diamond represent the corresponding region shown in Figure 4.6 with the same color.

detail: X-intercept, slope (slope= $\tan\theta$) and the saturation count (indicated in Figure 4.7 (a)). Ideally, if the offset is zero, each electron contributes a certain number of counts, dependent on the conversion factor (efficiency), i.e.slope of the linear fitting. However, in most cases the offset is not zero. The X-intercept represents the electron dose that must be exceeded to produce counts. The X-intercepts and slopes are different from one position to another position on the detector. Figure 4.7 (b-c) and (e-f) show the slope and X-intercept against the brightness and contrast respectively, with dashed curves showing fits. The fit functions used are $y = a$ in (b) and (d), $y = ax$ in (c) and $y = e^{ax+b}$ in (e) and (f), where a and b are constant and x and y are variables.

Figure 4.7 (b) shows that brightness has little influence on the slope and is linear with the X-intercepts shown in Figure 4.7 (c). As indicated in Figure 4.7 (c) (black dashed circle), when the contrast is set to 2000, the X-intercept is zero for all three locations when the brightness is about 2900, showing that the offset for all location is zero. When the brightness is more than 2900, the offset of the detector is less than zero and the X-intercepts are negative, which means a positive background level will be added to the output count even though there are no electrons hitting the detector. When the brightness is less than 2900, a negative background is applied to the output counts as some of the signal generated by the electron is "swallowed" by the pre-amplifier. Thus the brightness 2900 setup is important where every electron proportionally contributes to the output counts with the offset of zero. With this setup the count read out can be linked to the number of electrons hitting the positions. The non-zero offset is not important for work involving to work out the intensity with background subtraction, as long as the electron

dose hitting the lowest response region (the region around the blue diamond position in Figure 4.6 (a)) exceeds its X-intercept. This is because the influence of the cut-off region can be cancelled out by background subtraction. However, when the work involving calculating the intensity contributed directly from the incident beam, the offset should be set to zero, otherwise it can lead to over- or under- estimation of the electron dose. Another relevant point from the Figure 4.7 is that the loss of the signal, S_{loss}, at each point is a fraction of the input signal, S_{input}, i.e. mathematically $S_{loss} = aS_{input}$ $(a < 1)$, instead of $S_{loss} = aS_{input} + b$. If this were not the case then, the lines in Figure 4.7 (c) would reach zero at different brightness instead of the same one.

The relationships between contrast and the slope, and between contrast and the intercept are not linear (Figure 4.7 (e) and (f)). As shown in Figure 4.7 (e), the slope increases exponentially as a function of contrast. However, the relative slopes (the relative conversion factors) stay unchanged with the contrast setup (Figure 4.7 (d)). If the offset is zero, i.e. at brightness of 2900, the relative slopes are the same as the count ratios as there is no cut-off region and the count-current curves pass through the origin. The relative conversion factor can be mapped directly by scanning the detector and normalising the intensity map. Alternatively a line function fitted to the linear operating region for each position at the detector is needed and then normalise the slopes. As shown in Figure 4.7 (a), the X-intercept is equal to the offset level of the detector divided by the slope. The slope is an exponent function of contrast, so in Figure 4.7 (f) the X-intercepts exponentially decrease with the contrast.

In summary, investigating the brightness and contrast setup of the preamplifier of the

detector allows two useful conclusions to be drawn: (1) When the brightness is 2900, the offset of the pre-amplifier is zero; (2) Combining the facts that brightness does not change the absolute slope (and thus the relative slope) and that the contrast does not change the relative slope across the detector, it can be concluded that the relative conversion factor is invariant between different brightness and contrast setups.

4.6.2 The saturation of ADF detector

Another parameter that must be considered in experiments is the saturation of the detector. Figure 4.8 (a) shows a saturated ADF detector. It can be seen that the saturation count is the same all over the detector. This implies that the saturation happens at the preamplifier, because the response of the scintillator varies so the saturation should be different from position to position if it is the scintillator saturated. Saturation count has a linear relationship with dwell time during scanning, which is 4.99×10^4 count/μs (Figure 4.8 (b)).

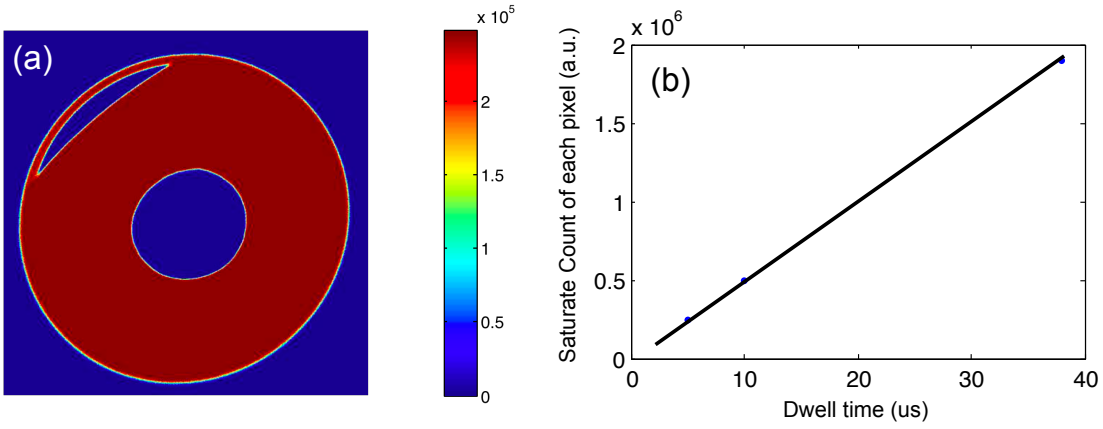

Figure 4.8: (a) Saturated ADF. (b) Saturation count against scanning dwell time.

4.6.3 Conversion factor (efficiency) mapping

The conversion factor is important for estimation of the electron scattered by the specimen compared with the incident beam. As described above, the relative conversion factor does not change with brightness and contrast setup. In this study, the conversion factor has been mapped as follows: (1) the response was mapped at each beam current and aligned

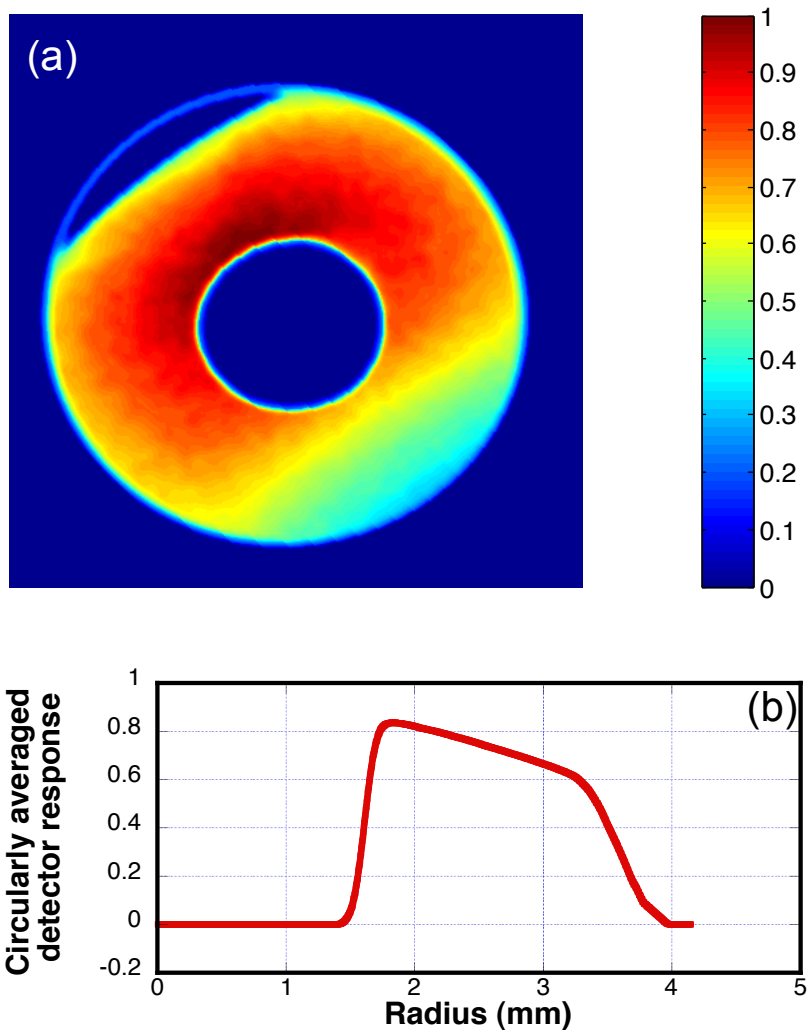

Figure 4.9: (a) Conversion factor mapping. (b) Circularly averaged conversion factors.

using a correlation coefficient; (2) at each position, after being averaged over 10×10 pixels windows, the linear range was fitted with a linear function; (3) the slope of the fitting parameters was obtained and normalised to the highest slope. As shown in Figure 4.8 (a), the obtained map is slightly distorted because the electron beam was not perfectly aligned. In Figure 4.9 (a) the geometrical distortion of the mapping has been corrected by assuming the detector has a ring-shape to allow circularly averaging (shown in Figure 4.9 (b)). The mapping also shows a geometry-dependence with the same feature as the example shown in Figure 4.6 (a), which is a scanning of the detector of only one beam current. The left-upper inner region has the highest efficiency and the right-lower outer region has lowest efficiency. This can be explained by the generated photons needing multiple reflections to reach the PMT or attenuating by them being absorbed in the waveguide so that they suffer a loss. This mapping can be taken into account in simulation to compare the absolute scattering fraction between experiment and simulation [178]. The circularly averaged response (Figure 4.9 (b)) shows that in most of the part the efficiency is between 0.6-0.8.

4.6.4 Implication on the cluster characterisation

For small clusters, electron scattering is usually dominated by kinematic scattering. Figure 4.10 shows the effect of a non-uniform detector on cluster characterisation. Figure 4.10 (a) shows size-selected Au_{887} clusters at the magnification of 1M×, with brightness and contrast of 2900 and 1700, respectively, and inner collection angle of CL10. The beam current was varied as mentioned before. The clusters labelled in Figure 4.10 (a) were tracked with different beam currents but the same scanning speed. Figure 4.10 (b)

shows the average integrated intensity of these clusters as a function of beam current. The standard deviations of those integrated intensities form the error bars. Figure 4.10 (b) shows that the integrated intensity of the clusters is linear with the beam current, implying that although the detector is not very uniform, this does not have a significant impact on kinematic scattering. Another point relevant is that as the beam current is varied by a combination of spot size and aperture, the linearity in Figure 4.10 (b) also shows that convergence angles (about 14 mrad and 20 mrad) have little influence on the intensity of the clusters.

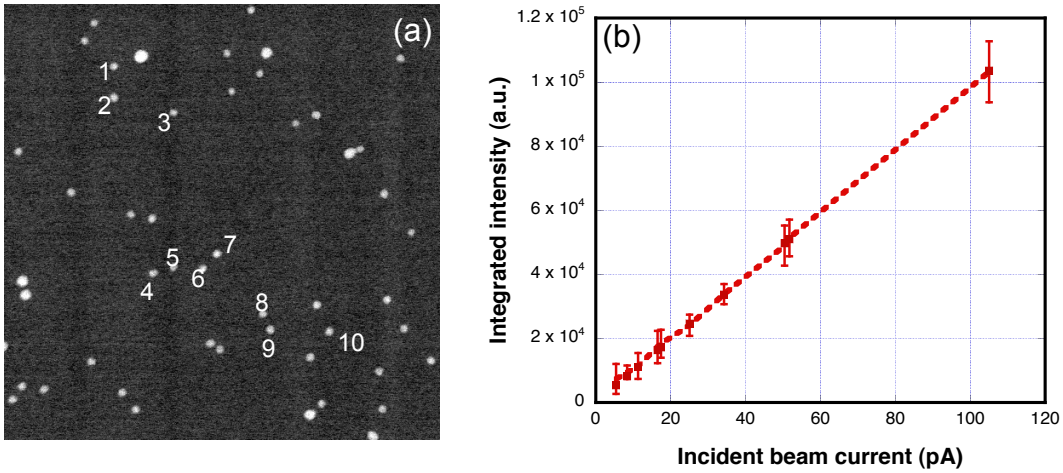

Figure 4.10: (a) The Au_{887} clusters chosen to be tracked under different beam current. The image was acquired under 1M (image length 157 nm). (b) The integrated intensity of the clusters as a function of beam current. The error bars are estimated from the standard deviation. The dashed line is the fit with a function of $y = ax$.

4.7 Summary

In this chapter, the pixel size, convergence and collection angle and the non-uniformity of the detector have been investigated for the microscope JEOL 2100F in the University of

Birmingham. It allows better understanding of the image, particularly in the quantitative work to be presented in the following chapters. In general, the intensity collected by the detector increases proportionally to the number of electron if the spatial distribution of the electrons invariant, which is the case for kinematic scattering. However, if the spatial distribution of the electron varies (for example as a function of the thickness for thick sample), the non-uniformity should be taken into account and the efficiency map can be incorporated into simulation.

Chapter 5

Modelling HAADF-STEM image

5.1 Introduction

A high angle annular dark field-scanning transmission electron microscopy (HAADF-STEM) image is a two dimensional projection of a three dimensional object. Because of the intrinsic instability of nanoclusters, often, only limited time is allowed to image the clusters. In other words, often only single-shot image is possible. Therefore, it is very important to reliably quantify parameters from HAADF-STEM to extract as much information as possible, for example, the size and shape of the clusters. With the help of the aberration corrected STEM, it is possible to determine thickness in terms of the number of atoms and the position of atoms, i.e. count atoms column by column.

In study of small clusters, it has been shown in the past the kinematic approximation is valid [9, 179, 180], which simplifies greatly quantitative analysis of HAADF-STEM images. In this chapter, the justification of the kinematic approximation will be given

first. This will be followed a detailed description of mathematical model of STEM image, which was firstly applied to the HAADF-STEM image by Van Aert et al. [181]. The methodology to extract atomic column position and to count number of atoms will then be introduced. Examples will be given in illustrating the steps. By applying the method to particular systems, the work in this thesis has generated two papers [182, 183]. As an reversed process, the kinematic simulation will also be introduced. A software has been written to allow the kinematic simulation and will be uploaded online soon.

5.2 The linearity of HAADF intensity

Figure 5.1 is a representative HAADF-STEM image of Au_{887}. Single atoms can be seen in the vicinity of the cluster (indicated by arrows), and the atomic columns within the cluster are also visible. Three dimensional information of the cluster can be extracted from this

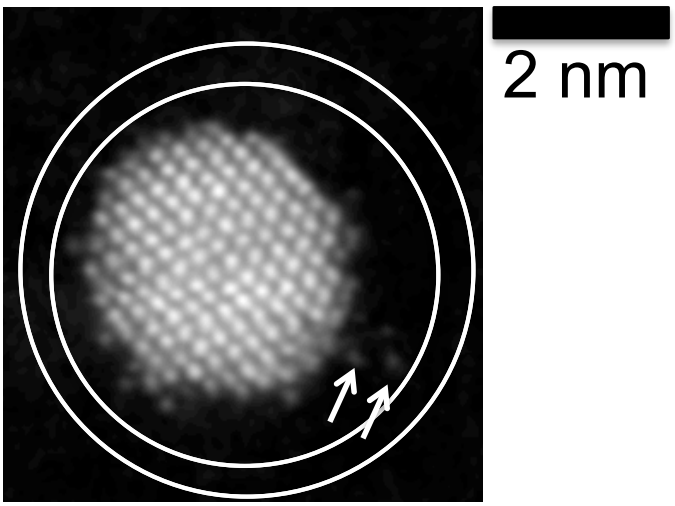

Figure 5.1: A typical HAADF-STEM image of Au_{887}. The arrows point at individual atoms at the vicinity of the cluster.

image in three ways: integrated intensity of the whole cluster, integrated intensities of individual atomic columns, and the peak intensities of atomic columns.

There are many ways used to obtain the integrated intensity of clusters depending on the treatment of the background. In this work, the integrated intensity is worked out using two rings as shown in the Figure 5.1. The background level of the cluster is estimated from the intensity between the two rings. Thus the integrated intensity of the clusters is given by

$$I = A_i M_i - \frac{A_i(A_o M_o - A_i M_i)}{A_o - A_i}, \tag{5.1}$$

where A_i, M_i are the area and the mean value within the inner ring and A_o, M_o are the area and the mean value within the outer ring. The first term on the right side of Equation 5.1 is the integrated intensity of the whole cluster including the background, and the second term is the estimated background, which assumes the same background intensity density of the inner ring region as the region between two rings. The criterion for choosing the size of the two circles are: (1) that they are large enough to ensure all atoms in the cluster are included, and (2) that they are small enough to avoid the unevenness of the carbon film. All the values required for the calculation can be obtained using ImageJ [184].

Extracting information about the total electrons scattered by each atomic columns, which contributes to the integrated intensity of the atomic columns, is not a trivial task. When the electron beam is focused into a small spot, the tail of the spot can extend to neighbouring columns and the so-called 'cross talking' occurs. As a consequence, the

intensity of one column is included in the intensity of the neighbouring columns and vice verse. To solve this problem, Van Aert et al. proposed an empirical method [181], where by rather than deconvolving of the image, the experimental image is compared with the parametrised model image. The best parameter vector is obtained by applying the uniformly weighted least square criterion.

Another approach to this problem compares the peak intensities of the atomic columns [180]. It applies a correlation between a Gaussian function and the normalised image to find the peak positions, then calculate the average intensity within a disk around each peak. The ratio of this value to the dose of the incident electron beam can be compared with the frozen phonon multislice simulation at an absolute scale [185]. This allows the local thickness to be determined to an accuracy of several atoms.

Figure 5.2 shows a summary of these three types of quantitative work. Experimentally all of them show that, if the sample is not very thick, the HAADF image intensity is approximately linear with the number of atoms, implying that the kinematic scattering dominates at the very small scale. This can simplify the mathematical treatment of the HAADF-STEM simulation for small nanoparticles. Figure 5.2 shows that when the size is smaller than 887 for Au cluster (or the atomic column height along the electron beam direction is lower than 12 atoms), this assumption is valid.

Another advantage of the HAADF-STEM imaging is that it can distinguish the chemical composition of materials by analysing the relative contrast when the thickness is uniform. This originates from Rutherford scattering, as higher atomic number atoms scatter electrons more strongly. The image contrast between elements can be modelled as

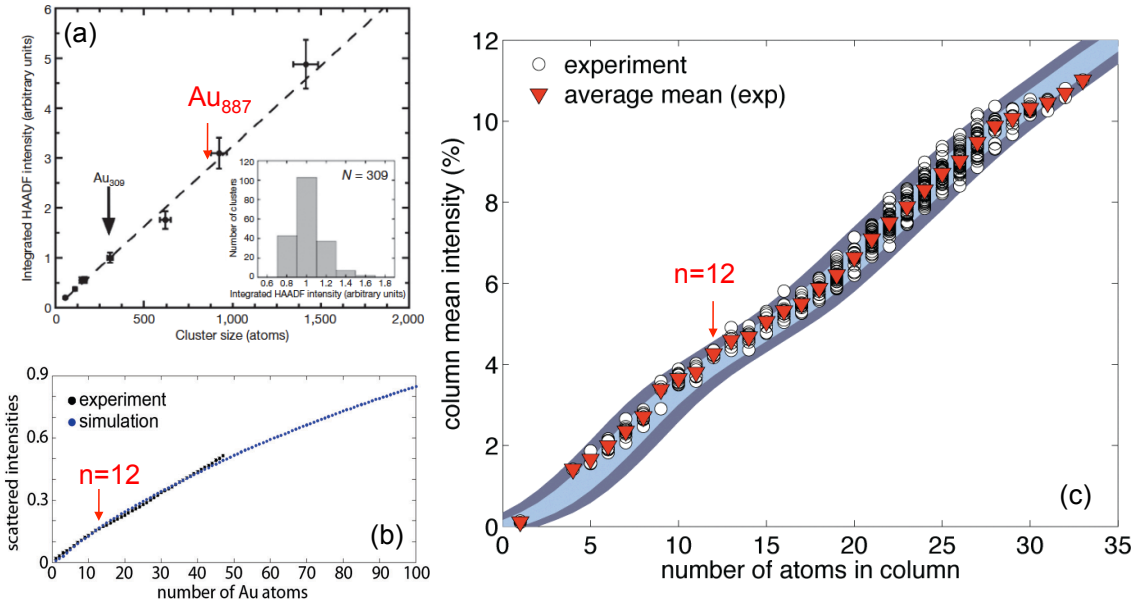

Figure 5.2: Recent study of linearity of HAADF-STEM intensity of Au atoms. (a) The integrated intensity of cluster against cluster size. (b) Integrated intensity of atomic column against atomic thickness. (c) Peak intensity against the thickness of sample. Au_{887} whereas the highest atomic column contains 12 atoms, is indicated in each plot by red arrows. (a), (b) and (c) are adapted from [9], [179] and [180], respectively.

Z^n. Because the electron cloud screens the nucleus charge, which happens noticeably at small collection angles, the value for n is normally less than 2. However, increasing the collection angle, n can get closer to 2, which means it depends on the geometry of the detector used [172].

5.3 Modelling of HAADF-STEM image

In incoherent HAADF-STEM imaging, the image intensity $I_{incoherent}(\mathbf{r}_{k,l})$ at pixel (k,l) can be modelled as a convolution between an object function $O(\mathbf{r}_{k,l})$ and a probe function $P(\mathbf{r}_{k,l})$[186]

$$I_{incoherent}(\mathbf{r}_{k,l}) = |O(\mathbf{r}_{k,l})|^2 \bigotimes P(\mathbf{r}_{k,l}), \tag{5.2}$$

where as the $\mathbf{r}_{k,l}$ is the vector of the pixel position (k, l). The object function is sharply peaked at the atomic columns [187]. It is modelled as a superposition of two dimensional Gaussian functions. The probe function is the intensity of the illuminating probe and it can vary from one experiment to another. In this section, to obtain a simplified and a general mathematical description of the HAADF-STEM image, the probe function is approximated as a 2 dimensional Gaussian and discussed as follows.

In practice, the souce is not an infinitely small point. Therefore, the probe function, $P(\mathbf{r})$, which is a positive-real point-spread function, is treated as the convolution between coherent source contribution and the incoherent extended source size effect [188],

$$P(\mathbf{r}) = |p(\mathbf{r})|^2 \bigotimes S(\mathbf{r}), \tag{5.3}$$

where $p(\mathbf{r})$ is the probe function for the infinitely small and $S(\mathbf{r})$ is the geometric image of the source after taking into account the demagnification [173]. The probe function $p(\mathbf{r})$ is given by the inverse Fourier transform of the aperture function $\mathrm{A}(\mathbf{u})$ (Equation 3.10) [186]. The intensity distribution of the extended source image $S(\mathbf{r})$ is usually assumed to be a Gaussian:

$$S(\mathbf{r}) = \frac{1}{2\pi d_s^2} \exp(-\frac{\mathbf{r}^2}{2d_s^2}), \tag{5.4}$$

where the d_s describes the size of the extended source image [186].

Ideally, if there is no source extension and aberration, the electron beam focused on the sample is an Airy disk, which appears with a central spot and series of concentric bright rings surrounding, whose sizes are dependent on the wavelength (accelerating voltage) and

the convergence angle. However, because of the source extension effect and aberration, it can blur the spot, so that the rings disappear and leave only a spot.

Figure 5.3 shows an the example of how an extended source blurs the Airy disk. Figure 5.3 (a1-2) is the Gaussian distribution of the extended source, which is described in Equation 5.5 with $d_s = 0.5$ nm. The simulated Airy disks were from focused plane incident wave with convergence semiangle of 15 mrad (Figure 5.3 (b1-2)) and 20 mrad (Figure 5.3 (d1-2)) without aberration. It can be seen that, when the larger convergence angle is used, the spot size is smaller in the ideal case. When the Airy disks are convoluted (blurred) with the extended size (described in Equation 5.3), most of the intensity accumulates into the central peak (Figure 5.3 (c1) and (e1)). The red lines are fitted Gaussian functions, and show that the fitting is fairly good.

Thus to simplify the mathematical calculation, the probe function $P(\mathbf{r})$ in Equation

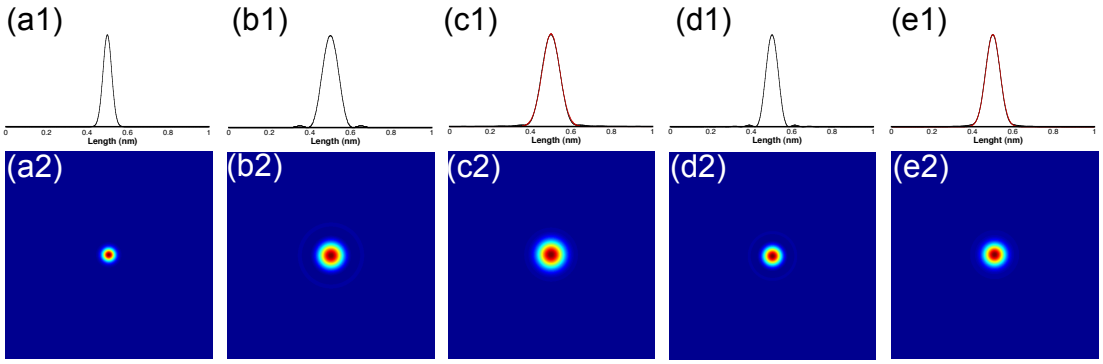

Figure 5.3: From left to right: (a1-2) the source blurring with FWHM 0.5 nm Gaussian distribution, (b1-2) the ideal Airy disk with 15 mrad convergence angle, (c1-2) the convolution of the source and the Airy disk with convergence angle of 15 mrad, (d1-2) the ideal Airy disk with 20 mrad, (e1-2)the convolution of the source and the Airy disk with convergence angle of 20 mrad. The plots (a1-e1) are profiles (black lines) of the two dimensional images beneath. The red lines are Gaussian fits to the blurred line profile.

5.2 can be replaced with Gaussian function. When a Gaussian with standard deviation c_1 convolutes with another Gaussian with standard deviation c_2, the result is a broadened Gaussian with the standard deviation $c_3 = \sqrt{c_1^2 + c_2^2}$. This approximation gives a simpler mathematical calculation. For example, when the cluster is off the axis, the intensity of each atom can be assumed to be a Gaussian function, while if it is on the axis, the whole atomic column can be assumed to be a Gaussian function.

Taking into account the approximation and substituting into Equation 5.2, the HAADF-STEM image from a mono-element sample can be simply modelled as superposition of Gaussians (broader than the object function), is given

$$I_{mol}(\mathbf{r}_{k,l}) = bkg + \sum_{m=1}^{M} A_m \exp \frac{-(x_k - P_{xm})^2 - (y_l - P_{ym})^2}{2\sigma_G^2}, \tag{5.5}$$

where bkg, A_m, P_{xm}, P_{ym} correspond to the background, amplitudes, x and y coordinates respectively. All of the Gaussians share the same width σ_G. When the width of each column is the same, the amplitude of the peak A_m can proportionally represent the total number of electrons scattered on the ADF detector. This simplified treatment enables the estimation of information without full knowledge of the experimental parameters such as d_s, the size of the extended source image.

5.4 Three dimensional image analysis

To reconstruct the three dimensional structure for the ultrasmall cluster is challenging. The most recent tomography can only rebuild half of the particles [189]. This technique

becomes even more difficult as the size of the nanoparticles reduces, because intrinsic instability of the small cluster as well as the interaction between the clusters and electron beam becomes non-negligible. In this work, three dimensional analysis realised with the help of HAADF-STEM imaging. Even though this technique cannot provide complete three dimensional information, such as the precise atom position in an atomic column along the electron beam, it can be useful in measuring the local thickness of sample and in gaining insight of three dimensional structure of nanostructured material.

There are three steps in this method. The first one is to use two dimensional Gaussians to fit the on-axis HAADF-STEM image in order to obtain the intensities of the atomic columns. The second step is to estimate the intensity contribution of single atoms from the histogram of the intensities of atomic columns. The third step is to count the atoms at the electron beam direction. The first and the second steps involve using a combination of Gaussians (the first step uses two dimensional Gaussians whilst the second step uses one dimensional Gaussians), but they are for different purposes and from different mathematical backgrounds.

5.4.1 Two dimensional image fitting

Using the uniformly weighed least squares estimator, the parameters vector in Equation 5.5, $g = (bkg, A_1, A_2, ...A_M, P_{x1}, P_{x2}, ...P_{xM}, P_{y1}, P_{y2}, ...P_{yM}, \sigma_G)$, can be estimated from the experiment. The estimates $\hat{g}$ are given when the uniformly weighted least squares

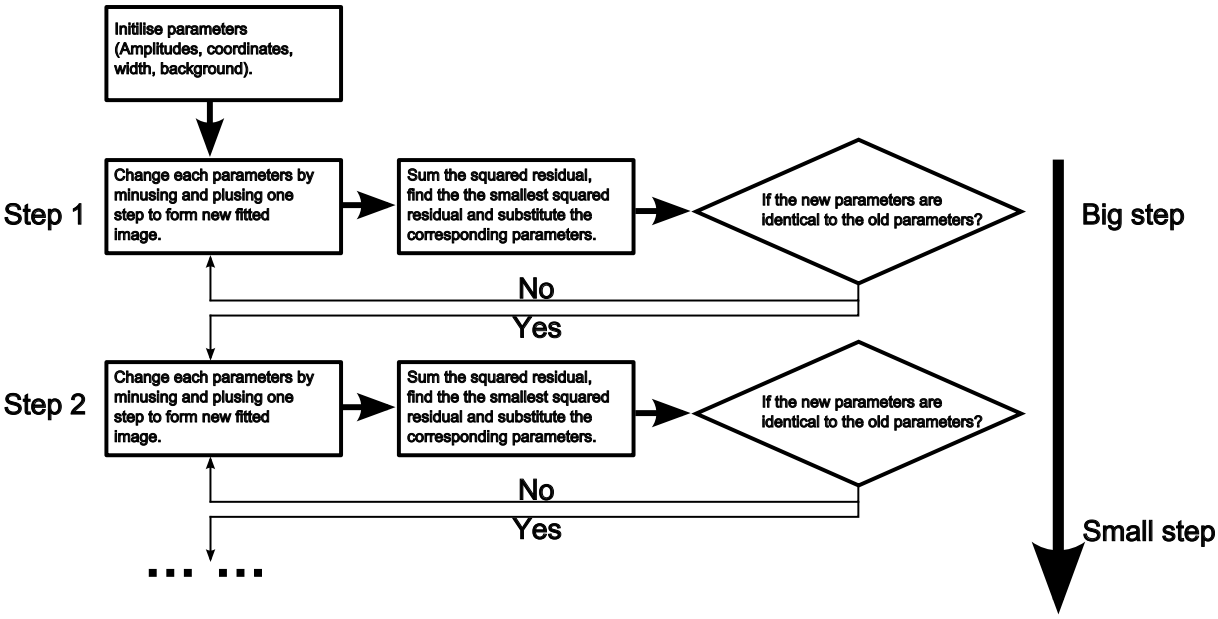

Figure 5.4: The flowchart of the two dimensional image fitting.

criterion is minimized [186],

$$\hat{g} = \arg_t \min \sum_{k=1}^{K} \sum_{l=1}^{L} (I_{incoherent}(k,l) - I_{mol}(k,l))^2, \tag{5.6}$$

with $I_{incoherent}(k,l)$ the HAADF-STEM intensity at the pixel (k,l) and the function $I_{mol}(k,l)$ given by Equation 5.6. The pixel values are independent and identically normally distributed about the expectation [186]. Thus the uniformly weighted least squares estimator is equal to the maximum likelihood estimator, which is known to have optimal statistical properties [186].

The procedure for fitting is illustrated in Figure 5.4. The initial parameters are obtained in this way: the image is filtered using Gaussian blurring to achieve a smooth image and the initial peak position is found using the "local maximum" function in ImageJ. De-

pending on the quality of the filtering, sometimes that two local maxima are chosen for one peak or peaks are missed can happen. Both of these can be corrected manually by adding or deleting the coordinates. The initial amplitudes can then be obtained by finding the intensity at the peak positions with background subtracted. The background is estimated from a corner of the image where there are no particles or contamination. The initial width is estimated by several trials of image fitting.

The initial parameters do not necessarily have to be accurate but they provide a starting point for the iterative algorithm. After the parameters are initialised, the fitting

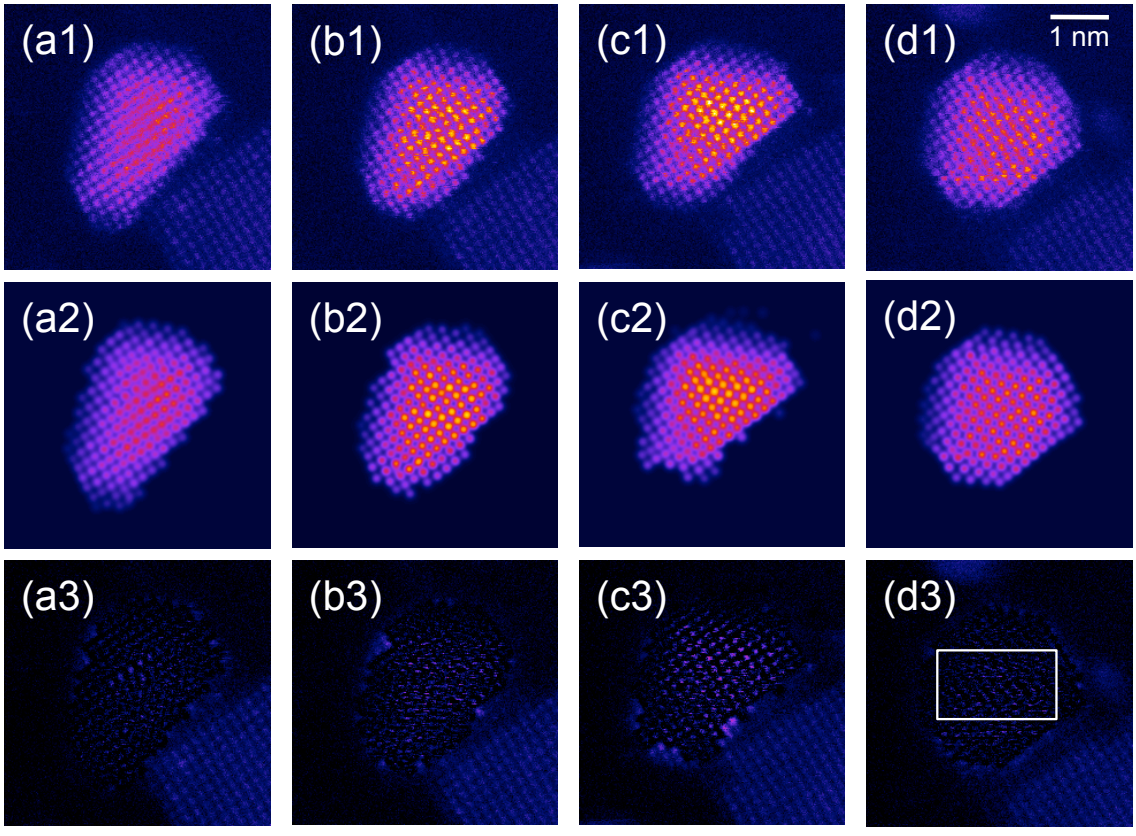

Figure 5.5: The first row (a1)-(d1)are the original successive images of a cluster on MgO. The second row (a2)-(d2) are the fitted image. The third row (a3)-(d3) is the residuals of the image subtraction. This figure is reproduced from [182].

runs with parameters that are based on the previous iteration. The length of each step is tunable in the fitting program and is usually dependent on the particular system. Generally, the step length goes from big to small to make the fitting convergence.

Figure 5.5 shows four successive experimental images (a-d1) of a Au cluster on MgO (100). The cluster was dynamically rearranging itself under the electron beam. The two dimensional fitting method has been applied to these images (shown in the second row) and the third row shows the residual (experimental images subtract the simulation). In this example most of the intensity in the centre of the cluster has been fitted. However at the edge of the cluster, where atoms are fluctuating more than the atoms in the centre, the fitting is less accurate.

Figure 5.6 shows the histogram of the counts indicated in the white box in Figure 5.5 (d3). This histogram shows the residual is symmetrically distributed around the 0 which is characteristic feature of a good fitting.

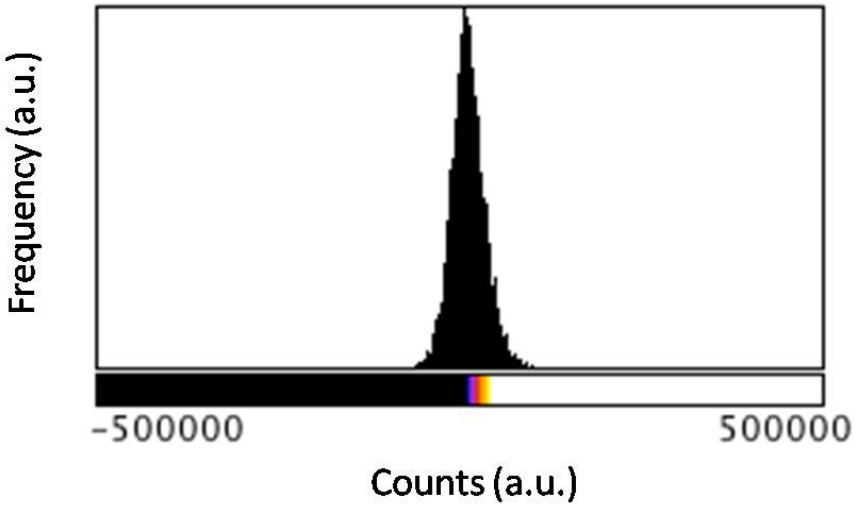

Figure 5.6: The histogram of the counts at the white box region indicated in Figure 5.5 (d3).

5.4.2 One dimensional Mixture Gaussian model

Upon completion of the two dimensional fitting, the histogram of atomic column intensity provides additional information. The histogram ideally should appear as a series of Delta functions with separated peaks. For each peak, the intensity should represent the number of atoms. The distances between adjacent peaks should arise from the contribution of an additional atom. However, in reality, the peaks are broadened by factors such as noise in experiment, atomic vibration etc. Thus each peak is modelled as a normal distribution and the whole histogram is a mixture of normal distributions. Each normal distribution is a component in the histogram. However, the number of components K is unknown. A mathematical method is needed to assess data partitions in histogram, choose the best number of components K and determine the position of each components. In this subsection, the basic maths is introduced and two applications are exemplified.

In the Bayesian framework, a way of selecting a model among candidate models is to choose the model of highest posterior probability [190]. In the case that all models have equal prior probability, which is the case here, then the model with the highest integrated likelihood also has the highest posterior probability [190]. For a probability distribution which is a mixture of normal distributions (so-called Gaussian mixture model), the integrated likelihood is described mathematically as

$$\mathbf{f}(V_i|\Psi_K) = \sum_{k=1}^{K} \pi_k \frac{1}{\sqrt{2\pi}\sigma} \exp[\frac{-(V_i - \mu_k)^2}{2\sigma^2}], \tag{5.7}$$

where V_i is the data in the histogram (for example fitted intensity for a particular atomic

column i), the vector $\Psi_K = (\pi_1, ..., \pi_K, \mu_1, ..., \mu_K, \sigma)^T$ contains the unknown parameters of the probability distribution, where the parameters μ_k and σ are the position and standard deviation of the Gaussian component k, respectively [186]. The mixing proportions sum to unity,

$$\sum_{k=1}^{K} \pi_k = 1. \tag{5.8}$$

Thus one of the mixing proportions is redundant and only K-1 mixing proportions need to be determined. Therefore, in total there are $2K$ unknown parameters.

The parameters Ψ_K need to be estimated from the obtained intensities V_i using the maximum likelihood estimator. The parameter estimates are given by the value of Ψ_K for which the likelihood function $L(\Psi_K)$ is maximized. For independent data V_i, the likelihood function is given by

$$L(\Psi_K) = \prod_{i=1}^{n} \mathbf{f}(V_i|\Psi_K), \tag{5.9}$$

where n is the total number of data points. In general, this maximization requires the use of an iterative numerical algorithm. If the number of components K is given, the likelihood can be calculated using the so-called expectation maximization algorithm effectively.

In practice, the value of K is unknown and has to be inferred from the available data. Generally, increasing the number of Gaussian components K in the model, improves the model fit, because when more parameters are used, more details are described. However, for large K, the details are random and do not provide extra information. The good model order K is found by balancing model fit and model quality [179]. Therefore, an order

selection criterion is needed to evaluate the statistical significance of an extra component in the model, in another word to justify how many components are needed. The so-called integrated classification likelihood (ICL) criterion is used here since it outperforms other order selection criterion [191],

$$ICL(K) = -2\log L(\Psi_K) + [2EN(V_i, \Psi_K) + 2K\log n], \tag{5.10}$$

where $EN(V_i, \Psi_K)$ is the estimated entropy.

5.4.2.1 Application 1: Counting atoms column by column

One application of the one dimensional mixture Gaussian model is to analyse the distribution of atomic column intensities. Because the number of atoms at each atomic column is an integer, the intensities of the atomic columns should be discrete values. As a result, the distance between neighbouring peaks in the mixture Gaussian model is the intensity contributed by one atom. Using this method, it is possible to understand the three dimensional shape of the nanoparticles.

For example, Figure 5.7 (a)-(d) shows histograms of the atomic column intensity for each image of Figure 5.5 (a)-(d). The individual images do not have enough data to show clear individual peaks, so in Figure 5.7 (e) all the data from all the images has been added together. By apply the ICL criterion, it shows 11 peaks, which are equidistant apart. Assuming that from low to high, each peak has one atom added, and plotting the intensity against the number of atoms (shown inset), a linear trend is apparent. By rounding the

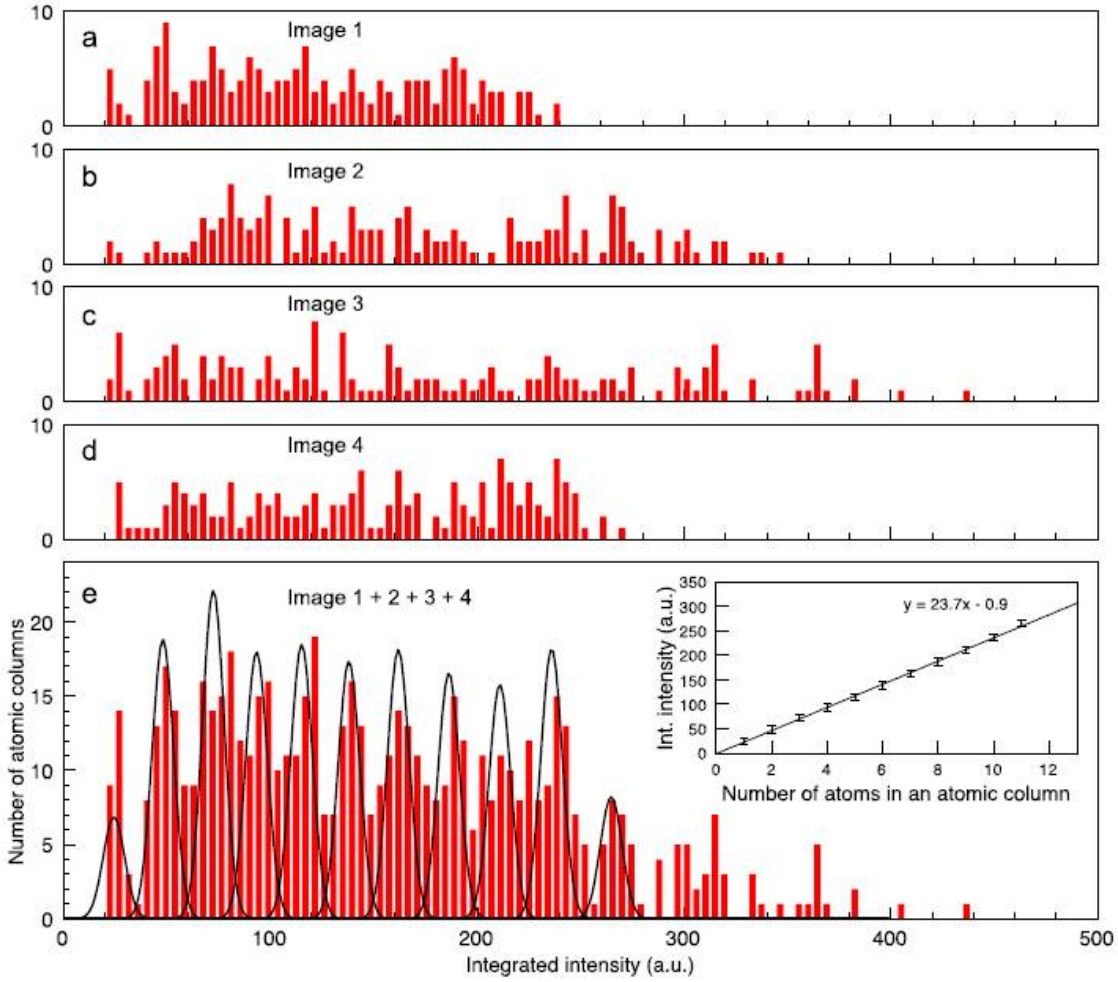

Figure 5.7: The histograms of the counts.(a)-(d) are individual intensity histograms corresponding to Figure 5.5. (e) is the total histogram of adding (a)-(d). The inset is the intensity peak against of number of atoms by assuming that each peak from left to right has only one atom addition. This figure is adapted from [182].

number of atoms of each column, the number of atoms in each column can be identified with accuracy of ± 1 atoms.

It should be noted that even though the expectation maximization method is a well-established method, the output could be dependent on the initial parameters. Here, the ICL calculation has been iteratively run 100, 200 and 500 times with random initial parameters, the results are shown below in Figure 5.8 where a maximum at the position

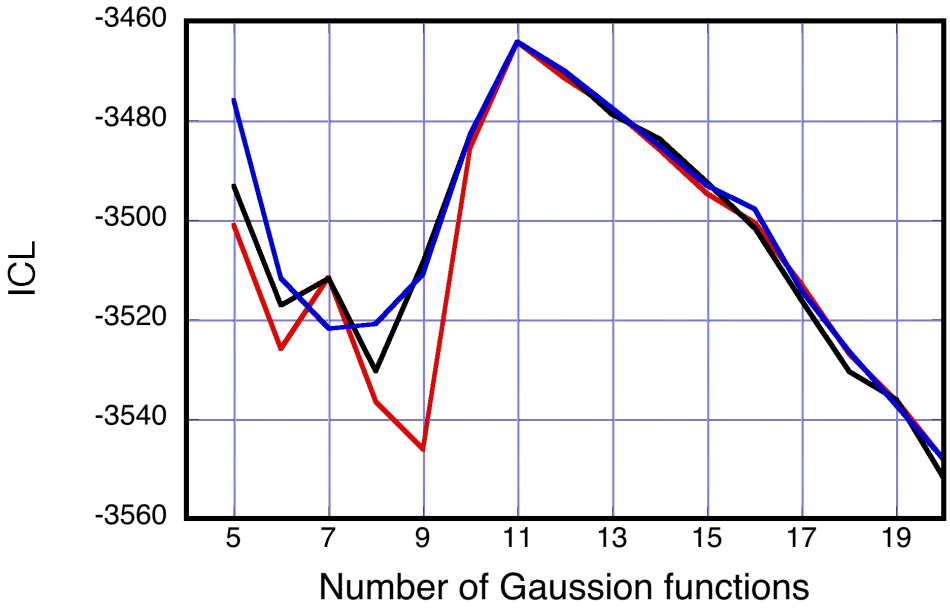

Figure 5.8: ICL calculated by repeating 100 (red), 200 (black) and 500 (blue) times of running the expectation maximization method with random initial parameters. This figure is adapted from [182].

of 11 is identified.

After identifying the number of atoms in each column, the three dimensional reconstruction can be performed. Using the one dimensional Gaussian mixture model, the contribution of single atom can be worked out as discussed above. Simply dividing the intensity of the columns by the intensity of single atom, and rounding to the nearest integer, the column height (in term of number of atoms) can be obtained as shown in Figure 5.9. It can be seen that the centeral columns in the right image have higher intensities compared to the left one, suggesting that the cluster has become elongated along the electron beam direction. The whole number of the atom within the cluster has also increased, which may be attributed to the electron beam activating single atoms/small clusters nearby and causing them to join with this cluster.

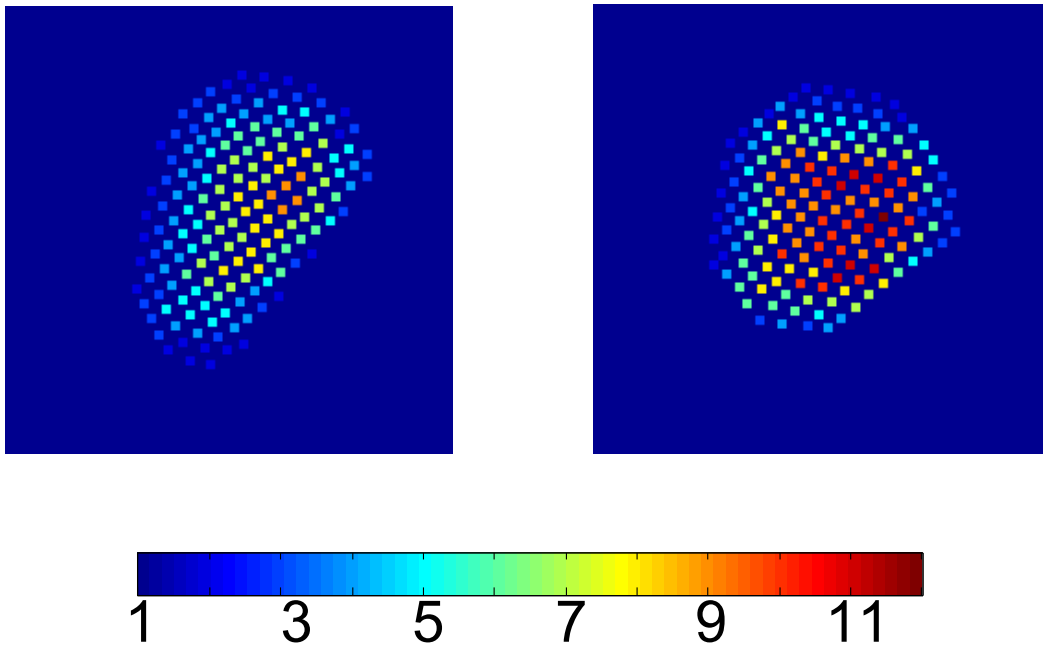

Figure 5.9: Atomic counting applied to the Au nanoparticles in Figure 5.5. left: the first frame in Figure 5.5 and right: the last frame in Figure 5.5.

5.4.2.2 Application 2: Mass distribution analysis

Another application of the one dimensional mixture Gaussian model is to analyse the mass distribution of the nanoparticles. For example in Figure 5.10, the clusters Au_{25} and Au_{38} (clusters containing nominal 25 and 39 gold atom) are imaged by the HAADF-STEM. The intensity distributions are plotted in Figure 5.10 (c) and (d) respectively. By applying the ICL, criterion, the distributions are found to consist of several peaks whose centers are integer multiples. This indicates that the aggregation of clusters on the surface is not via Ostwald ripening, but cluster fusion.

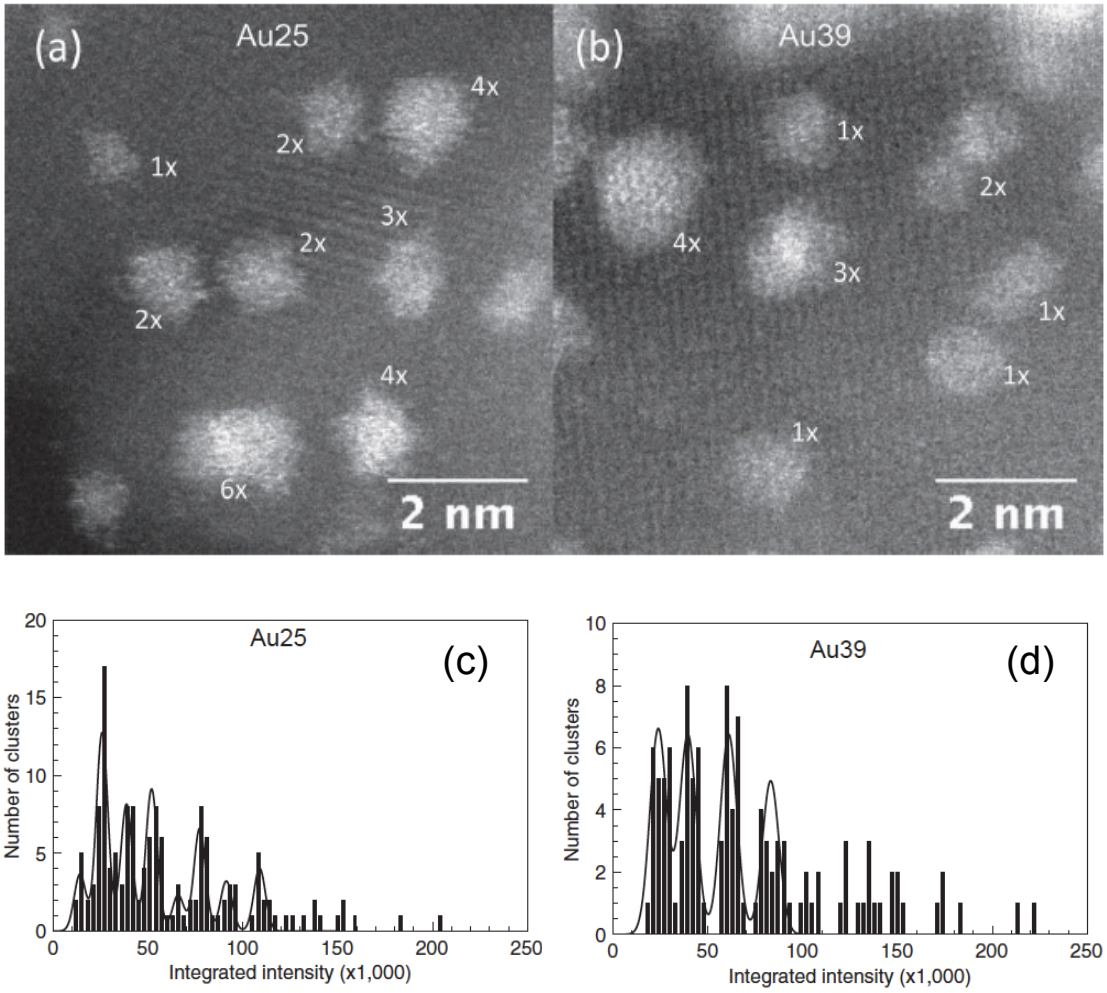

Figure 5.10: The HAADF-STEM images of (a) Au_{25} and (b) Au_{38} on carbon films. (c) and (d) are the integrated intensity histograms of Au_{25} and Au_{38}, respectively. This figure is adapted from [183].

5.5 Kinematic image simulation

For HAADF-STEM simulation, one can perform multislice dynamic simulation (such as using QSTEM) as well as kinematic simulation [9]. For small and thin clusters, the previous sections show that the intensity of cluster can be approximated to be the sum of the contributions of all the atoms, allowing the kinematic simulation to be used to achieve fast computational speed.

For a specific three dimensional structure the contribution of each atom can be considered as a Gaussian function in two dimensional HAADF-STEM image [10], which is

$$I_{atom}(i) \propto Z^n \mathrm{e}^{-c_g d_i^2}, \tag{5.11}$$

where d_i is the distance between the centre of the current grid point and the centre of the atom, and n is the exponent number. c_g is the Gaussian constant related to experimental conditions and the atomic column potential. The total intensity at the given point is given by the contribution of all the atoms,

$$I_{tot} \propto \sum_i I_{atom}(i). \tag{5.12}$$

Even though some part of this model lacks a physical basis, it is practically useful for small objects. Figure 5.11 shows an example of a Au_{309} cluster on MgO substrate shown in different orientations. The width of the peak has been assumed to be 0.12 nm (Full Width Half Maximum) and Z exponent used is 2. False colour is used to show both MgO and Au cluster. The gradual change of the MgO substrate in Figure 5.11 (b) is due to the thickness of the model for the particular direction, but the variation in local contrast in Figure 5.11 (b) shows the difference between Mg atomic columns and O atomic columns. This method can be used easily to generate kinematic simulations of HAADF-STEM images from all directions.

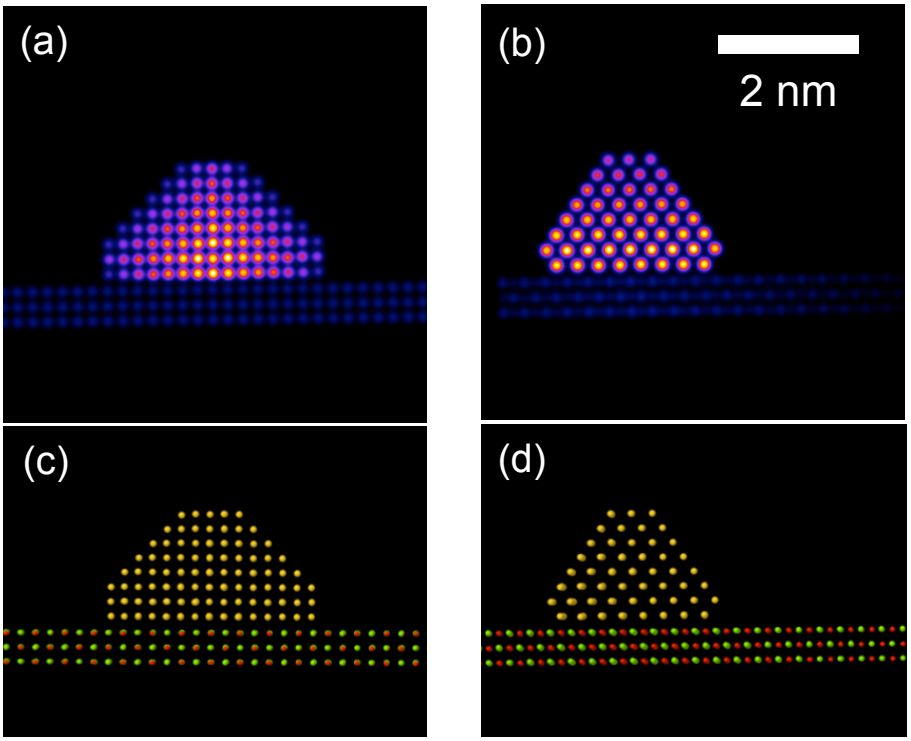

Figure 5.11: Simulation of Au_{309} on MgO from (a) [001] (b) [110] direction (with reference to Au). (c) and (d) are corresponding hard ball model. The coordinates are provided by Yisong Han.

5.6 Summary

To summarize, in this chapter, the HAADF-STEM intensity as a function of the sample thickness has been reviewed and found to be linear to the number of atom within clusters as well as in the atomic column at small size region. This has been verified through examples. It suggests that the kinematic scattering dominates at the small size and enables to assume the contribution of each atom is equal. Based on this assumption, an inhouse software has been developed to allow kinematic image simulation and will be used in the next chapter for structural identification.

Chapter 6

Cluster structural identification

6.1 Introduction

Simulation is extremely helpful to understand the acquired image. Ideally, the multislice simulation [192] is currently the most accurate approach. It essentially sections the specimen into discrete slices and calculates the beam on the projection plane of each slice. This is crucial when comparing the absolute intensity (the ratio over the incident beam). However, to do the multislice simulation for high angle annular dark field-scanning transmission electron microscopy (HAADF-STEM) image is computational expensive as it has to calculate the intensity point by point [192]. Using this method, it is very time consuming to simulate the cluster as a function of sample orientation in a very detailed fashion (one image can take hours [193]) and big gaps in orientation step may which may lead to some missing patterns.

In this thesis, instead of the multislice simulation, the kinematic simulation is per-

formed which is firstly published in [10]. The mathematics of the kinematic simulation has been discussed in detail in the Chapter 5. The advantage of this method is the fast computational speed, where for each image the computational time is almost negligible (less than 1 second on an Intel CPU with clock speed 2.67 GHz for a cluster containing less than 1000 atoms with 512×512 grids) without losing the characteristic features. Figure 6.1 is the comparison of the simulations using multislice (a1-a2) and kinematic (b1-b2) simulation. This is an icosahedron (Ih) cluster with a size of 923 atoms. It was simulated from $< 110 >$ and $< 211 >$ directions. They show similar overall pattern (for example, the positions of bright dots and the fringe directions). The kinematic simulations show more detail as they are 512×512 pixels.

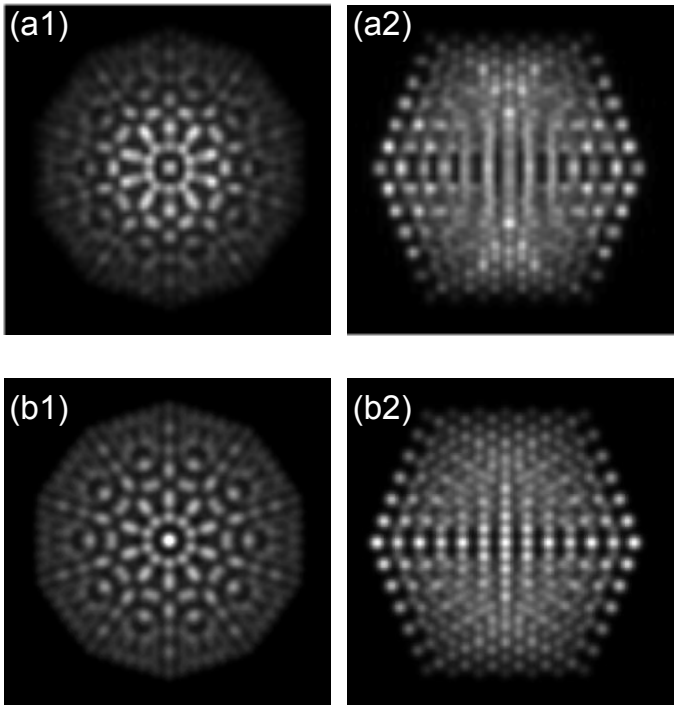

Figure 6.1: Comparison between the multislice simulation and kinematic simulation of Au_{923} Ih. (a1-2) The multislice simulation (adapted from [151])and (b1-2) the kinematic simulation are from $< 110 >$ ((a1) and (b1)) and $< 211 >$ ((a2) and (b2)) directions.

For comparison between experiment and simulation for structural identification, both the direct HAADF-STEM image and the fast Fourier transform (FFT) are used. The direct HAADF-STEM images contain rich information, including the distances and angles between lattice planes. The FFT emphasises the periodic features. Because the images are simulated at the absolute length scale, not only the angles between the spots in the FFT, but also the distance between them are comparable directly. However, due to the resolution limit of the microscope, normally only the 1-3 nearest spots are visible in the FFT.

In this chapter, the single crystal face centred cubic (FCC), decahedron (Dh) and Ih are made of 861 (truncated octahedron, TO), 887 (Marks-Dh), 923 atoms, respectively. The model cluster coordinates were supplied by Dr. Andy Logsdail, and were calculated from the mathematical constructs [194]. The nearest-neighbour bond lengths were scaled to bulk values and relaxed by the Gupta potential [78]. To make the structural identification more accurate, the single twinned FCC structure has also been taken into account in this work. The single twinned model cluster is made by imaging the atomic coordinates on one side of the central (111) plane of the TO model cluster to the other side, forming a twin boundary in the centre (indicated in Figure 6.5).

For each model cluster the "main orientations" and the "atlas" through a range of rotated angles are discussed and compared with experimental images. For the atlas, the model clusters are rotated with 10° increment per step. The five fold symmetry model cluster repeats its patterns each 72° (360°/5), so at 10° per step, which is not a rational factor of 72, gives both good overview and shows small changes in the pattern as a function

of rotation. The full width half maximum of the Gaussian function used in simulations is 0.12 nm. The simulations are scaled to the highest intensity. The hard ball models are shown with 15% and 100% van der Waals radius, which are generated from the free software Jmol [195]. The FFT of both experimental image and simulation are performed in the free software ImageJ [184]. All of the images are acquired with 512×512 pixels and has been filtered with 2 pixels Gaussian convolution. The source of error in structural identification is also discussed.

6.2 FCC

The FCC structure is a fraction of the bulk form as well as the building blocks of the multiply twinned particles (MTP). However, apart from the single crystal cluster, experimentally sometimes the lamellar twinned cluster is also observed, which is characterised by two or more parallel twin boundaries [196]. The simplest form of the lamellar twinned cluster has only one twin boundary, i.e. single twinned cluster. Therefore, two types of FCC are considered here, the single crystal FCC and the single twinned FCC. For the purpose of categorisation, due to the fact that single twinned and single crystal FCC can have the same feature at some direction, both of these clusters are put into the category of FCC.

6.2.1 Single crystal FCC

Figure 6.2 shows the kinematic simulation images and the hard ball models of a TO_{861} with low index orientations. This structure has $6 < 100 >$ orientations ([100], [010], [001], [$\bar{1}$00], [0$\bar{1}$0], [00$\bar{1}$]), $12 < 110 >$ orientations ([110], [101], [011], [$\bar{1}$10], [1$\bar{1}$0], [$\bar{1}$01], [10$\bar{1}$], [0$\bar{1}$1], [01$\bar{1}$], [$\bar{1}\bar{1}$0], [$\bar{1}$0$\bar{1}$], [0$\bar{1}\bar{1}$]), and $8 < 111 >$ orientations ([111], [$\bar{1}$11], [1$\bar{1}$1], [11$\bar{1}$], [$\bar{1}\bar{1}$1], [$\bar{1}$1$\bar{1}$], [1$\bar{1}\bar{1}$], [$\bar{1}\bar{1}\bar{1}$]) that all have the same patterns as shown in Figure 6.2 (a1), (b1) and (c1) respectively. The model cluster is enclosed by 8 {111} facets and 6 {100} facets.

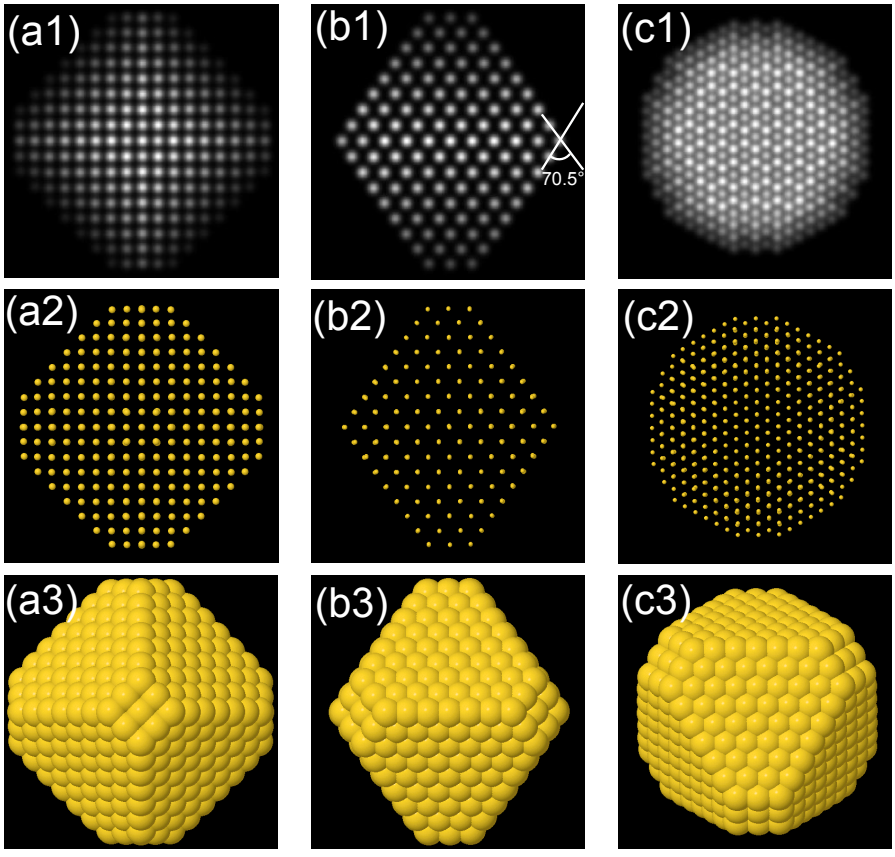

Figure 6.2: Low index orientation (a1-a3) $< 100 >$ (b1-b3) $< 110 >$ (c1-c3) $< 111 >$ of a TO_{861}. (a1-c1) The kinematic simulation; (a2-c2) hard ball model with 15% van der Waals radius (a3-c3) hard ball model with 100% van der Waals radius.

Each {100} facet is a 3×3 square atomic array, while each {111} facet is an equilateral triangle which is truncated by 2 atoms at each corner. Figure 6.2 shows the low index orientations, $< 100 >$, $< 110 >$ and $< 111 >$. Figure 6.2 (a1) is the pattern from the $< 100 >$ zone axis, showing square pattern, where dots represent the atomic columns. The distance of the nearest neighbouring column is $a/2$ where a is the lattice constant. Figure 6.2 (b1) is the pattern from the $< 110 >$ zone axis. The angle between two two dimensional atomic lattice directions is 70.5° (or 109.5°) (as indicated in the Figure 6.2 (b1)). It has the largest atomic inter-column spacing of the nearest columns of $\sqrt{6}/4a$. Figure 6.2 (c1) is the image from the $< 111 >$ zone axis. It shows hexagonal units and the distance between neighbouring column is $\sqrt{6}/6a$. The dimmer centre dots are due to atomic columns containing fewer atoms which is hard to distinguish in the case of TEM imaging as TEM imaging is mainly based on the phase contrast.

Figure 6.3 is the kinematic simulation atlas for the single crystal FCC model cluster rotating from 0-90° in α and β as indicated in Figure 6.3. It shows that the simulated images have either two or four fold symmetry.

As shown in Figure 6.4, there are four types of the pattern: (1) Two dimensional atomic columns, such as ($\alpha = 0°, \beta = 0° - 90°$) and ($\alpha = 40°$ and $50°, \beta = 0°$ and $90°$), is an array that is periodic and regular (exemplified in Figure 6.4 by the red box). The FFT patterns usually show six spots (a3-c3). The FFT of (a3) and (a4) are analysed in detail with vectors $\vec{l1}$-$\vec{l6}$ and summarised in Table 6.1. Both the lengths and angles are similar.

(2) Pattern with parallel and straight lines, such as ($\alpha = 10° - 30°, \beta = 0°$), ($\alpha =$

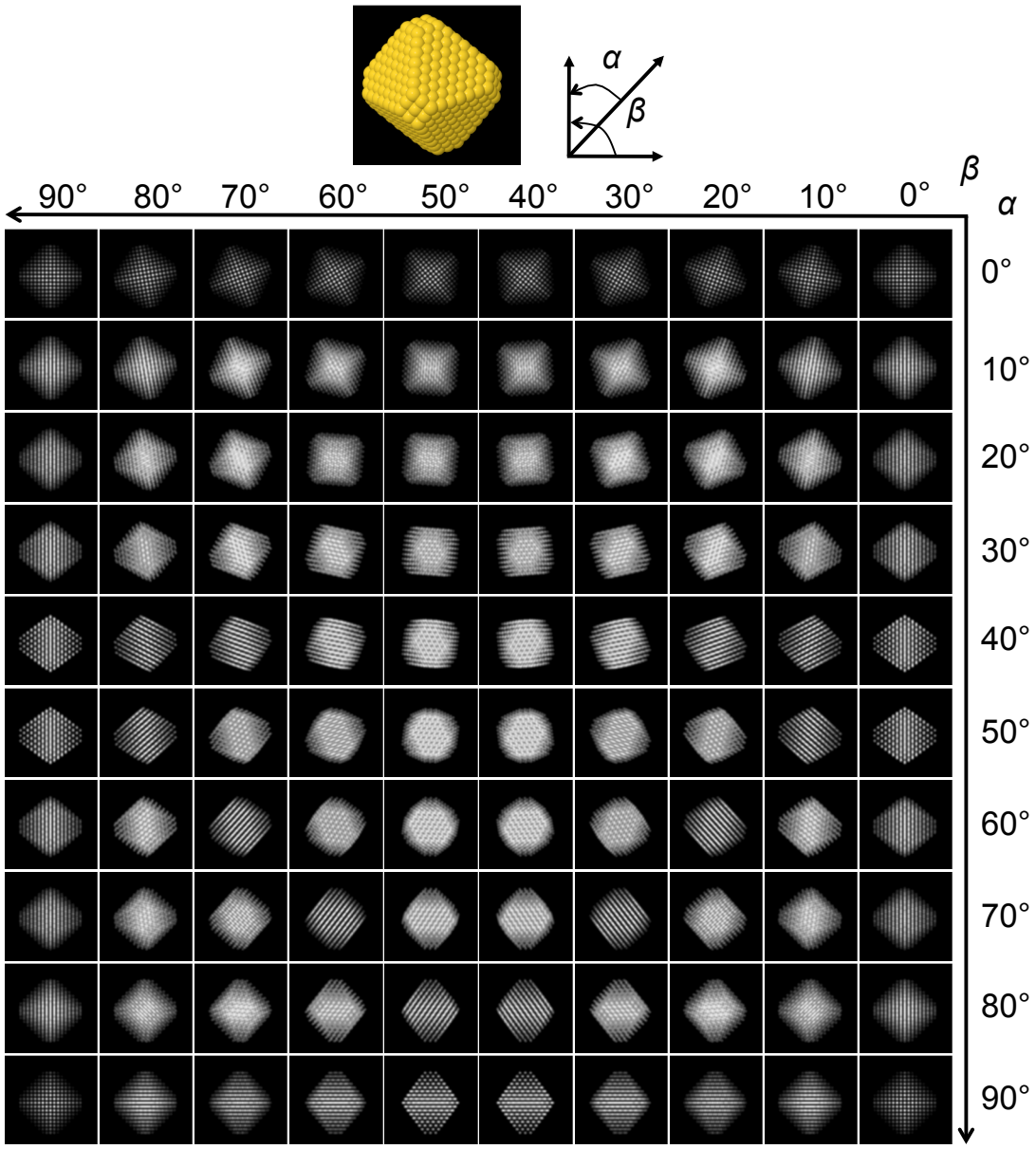

Figure 6.3: Kinematic simulation altas of TO_{861}.

40° and 50°, β = 10°). These are most frequently observed in experiments for FCC (exemplified in Figure 6.4 by the blue box). The FFT usually show two spots as they have only 1 dimensional features.

(3) Structures orientated in high index directions, so the two dimensional projections

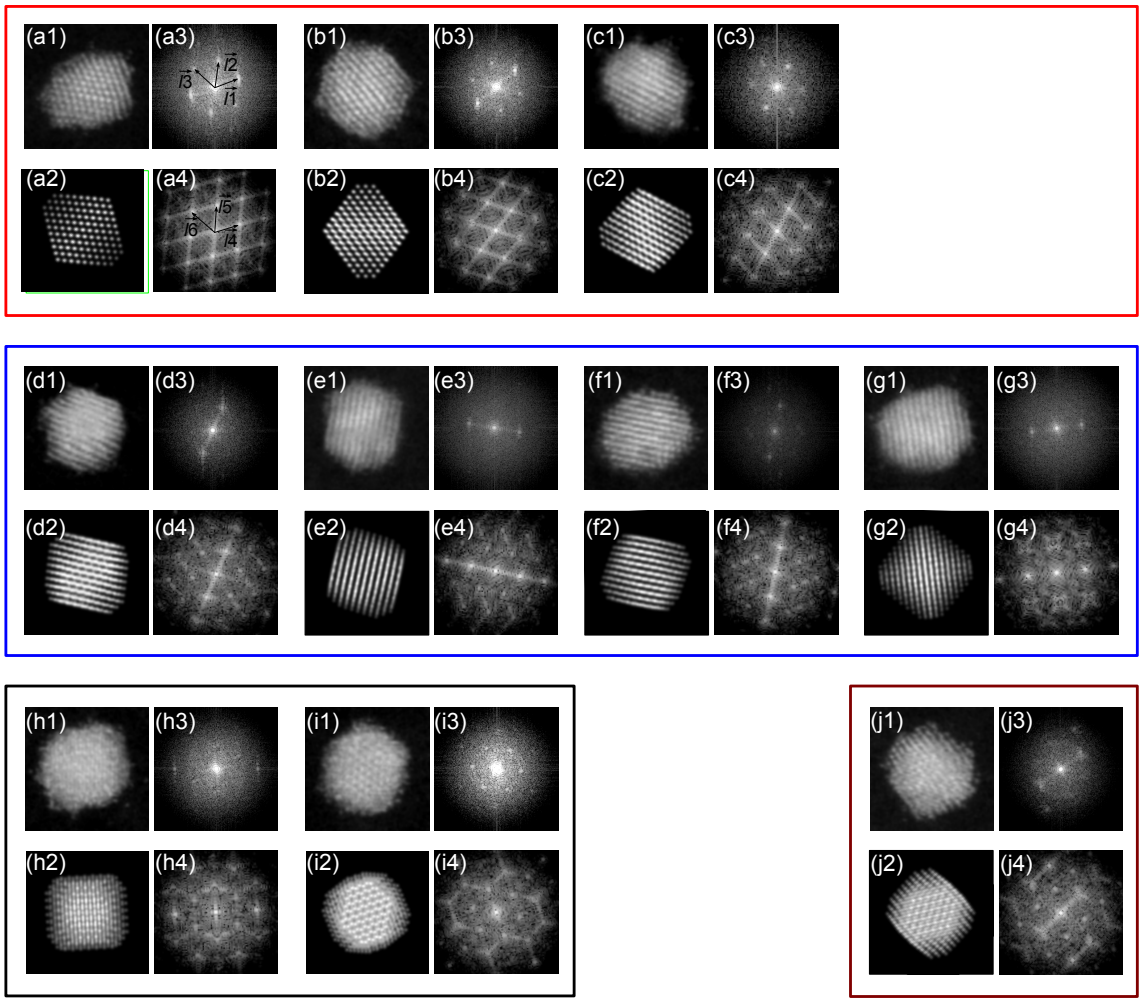

Figure 6.4: The comparison with the experimental images and the simulations of single crystal TO_{861}. (a1-j1) experimental images, (a2-j2) simulated image (a3-j3) FFT of direct images, (a4-j4) FFT of simulated images. The image patterns are placed into four groups boxed with red, blue, black and brown colours.

of the atoms is dense and the distance between the projections of atoms is less than the probe size. These images are essentially Moiré fringes (such as $(\alpha = 20°, \beta = 20° - 70°)$), which are periodic and regular (exemplified in Figure 6.4 by black box). The spots in the FFT can be slightly further away from the center, such as Figure 6.4 (h3) comparing with the FFT in the red and blue boxes.

(4) High index directions, where the edge regions show different regular feature from

Table 6.1: The comparison between the FFT of experimental image[1] and simulated image[2]

Length	(a.u.[3])	Length	(a.u.)	Angle between	(°)	Angle between	(°)
$\vec{l1}$	2138	$\vec{l4}$	2045	$\vec{l1}$ and $\vec{l2}$	59.5	$\vec{l4}$ and $\vec{l5}$	67.5
$\vec{l2}$	2290	$\vec{l5}$	2258	$\vec{l2}$ and $\vec{l3}$	58.2	$\vec{l5}$ and $\vec{l6}$	53.5
$\vec{l3}$	2525	$\vec{l6}$	2977				

[1] The left columns are from the FFT of experimental image ($\vec{l1}$, $\vec{l2}$ and $\vec{l3}$ in Figure 6.4 (a3)).
[2] The right columns are from the FFT of simulated image ($\vec{l4}$, $\vec{l5}$ and $\vec{l6}$ in Figure 6.4 (a4)).
[3] This value is the pixel length when adding the vector using the software Inkscape [197].

the centre as it has less atoms overlapped (such as $\alpha = 30°, \beta = 20° - 70°$); an example of this pattern can be found in Figure 6.4 brown box. As can been seen in Figure 6.4 (j3), there are two sets of spots, where the first one is nearer to the centre and resulted from the edge region of the cluster and the second is further and resulted from centre of the cluster.

In the case of (3) and (4), the fringes are result from overlapping of the atomic columns, so bright dots do not necessarily correspond to the atomic columns directly any more.

6.2.2 Single twinned FCC

In experiment, due to the formation of stacking faults at the {111} plane, some FCC clusters have parallel twins (so called lamellar twinned particles). It was suggested by Smith and Marks that this type of cluster should be considered as a distinct particle type [196]. In this work, as the structure is identified using single-shot method, the single twinned particles have been categorised as FCC to minimize error in identification, as in some directions that the electron beam is parallel or normal to the twin plane, the single

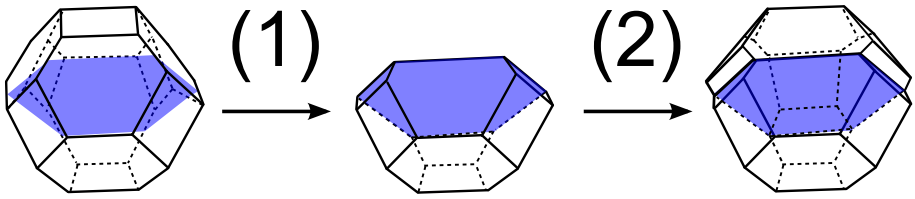

Figure 6.5: The schematics of how to build the single twin FCC from a single crystal FCC. The blue plane is where it cuts the single crystal and where the twin boundary is located.

twinned particles are intrinsically undistinguishable from the single crystal particle. In this study, the single twinning model cluster is built in such way (indicated in Figure 6.5): (1) cutting the single crystal TO model cluster along the central {111} plane, (2) mirror imaging the atom coordinates from one side of the TO against the cutting plane. It gives two FCC subunits in this cluster, divided by a twinning plane.

Figure 6.6 (a) shows single twinned clusters along the $< 111 >$ orientation where the twin plane is parallel to the sitting plane, so that the twin boundary is not visible. The pattern is made of hexagonal units, with the similarity in Figure 6.2 (c1), but with a slightly different outline. The other two directions given in Figure 6.6 (b1) and (c1) also contain this hexagonal pattern ((b1) ($< \bar{1}11 >$) and (c1) ($< \bar{1}1\bar{1} >$)), however only in part of the cluster, with the other exhibiting a different pattern, which show the two twinned segments in the simulation.

In Figure 6.7 (a) and (b) the single twinned FCC model cluster is $< 110 >$ and $< 1\bar{1}0 >$ orientated. A common feature is the appearance of the single crystal $< 110 >$ pattern, which makes it very easy to resolve and identify. Both orientations show two segments. In Figure 6.7 (a1), the other part is featured with fine lines and dots. Experimentally, these features could be blurred as they are smaller than the probe size. In Figure 6.7 (b1),

there is a clear twin boundary dividing the image into two and the pattern is symmetric about the twinning plane. This shows that the orientation is vertical to the sitting plane. In Figure 6.7 (c1) the $< 100 >$ single crystal pattern of square lattice can be seen in one part while the other part features straight lines normal to the boundary line.

Figure 6.8 shows the kinematic simulation atlas for the single twinned model cluster. There are four types of the pattern:

(1) With the model cluster orientated around the $< 1\bar{1}0 >$ direction (Figure 6.9 (b1)) the pattern is divided into two segments by the twin boundary, such as ($\alpha = 10° - 80°, \beta =$

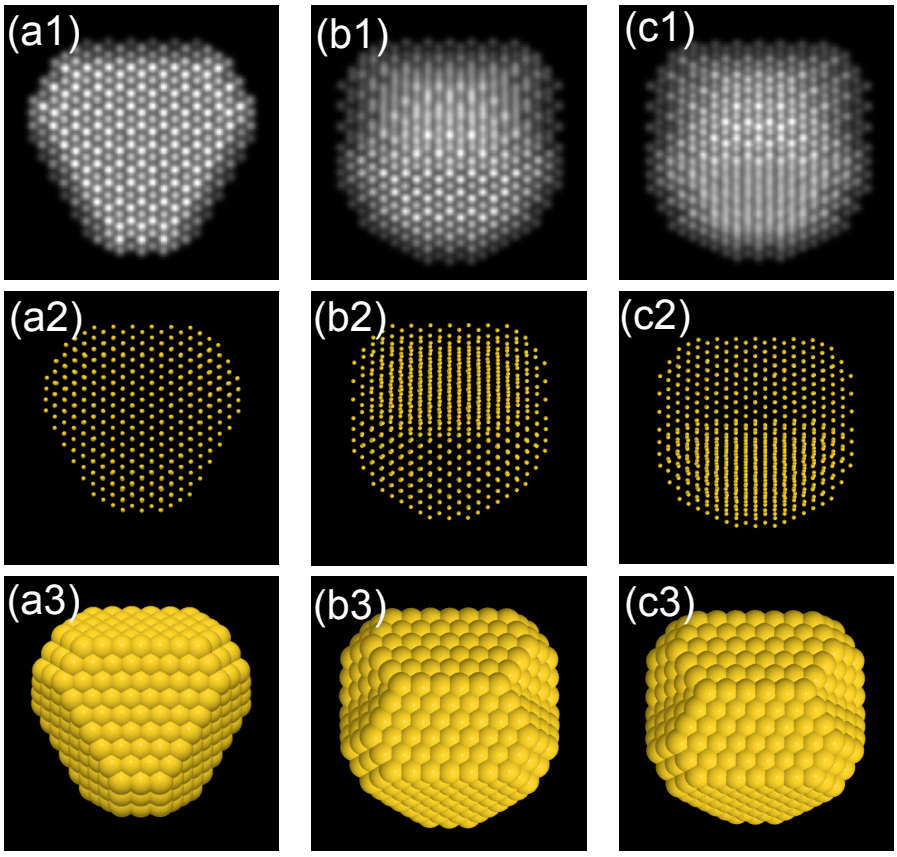

Figure 6.6: (a) $< 111 >$ (b) $< \bar{1}11 >$ and (c)$< \bar{1}1\bar{1} >$ orientated single twinned model cluster. (a1-c1) The kinematic simulation, (a2-c2) hard ball model with 15% van der Waals radius and (a3-c3) hard ball model with 100% van der Waals radius.

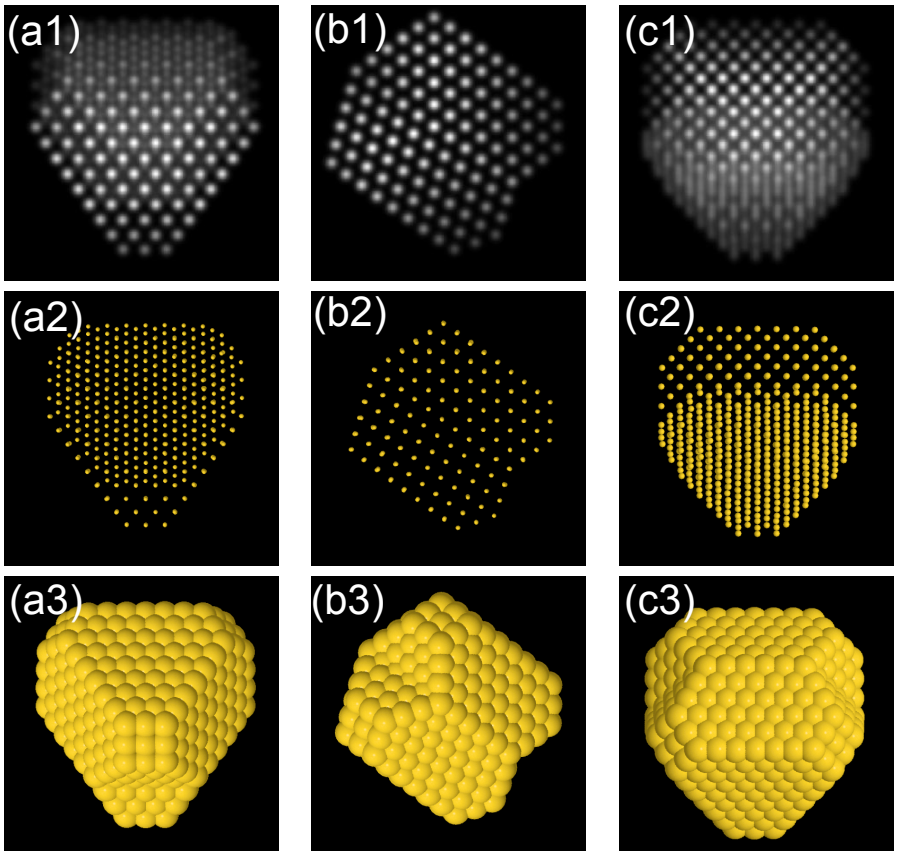

Figure 6.7: (a) < 110 > (b) < $1\bar{1}0$ > and (c)< 100 > orientated single twinned model cluster. (a-c1) The kinematic simulation (a-c2) hard ball model with 15% van der Waals radius (a-c3) hard ball model with 100% van der Waals radius.

90°). Each of the segment shows a FCC pattern with lines or two dimensional atomic lattice, as exemplified in Figure 6.9 by the red box. As the patterns of the two segements have similar inter-lattice distance but tilted to slightly different orientation, a pair of spots shown in the FFC (Figure 6.9 (a3)).

(2) A pattern composed of two crossed lines, which are usually bended and exemplified in Figure 6.9 by the blue box. The FFT patterns normally show 4 spots.

(3) More complicated features appear in the pattern (exemplified in Figure 6.9 black box). However, these complicated features give more information for structural identifi-

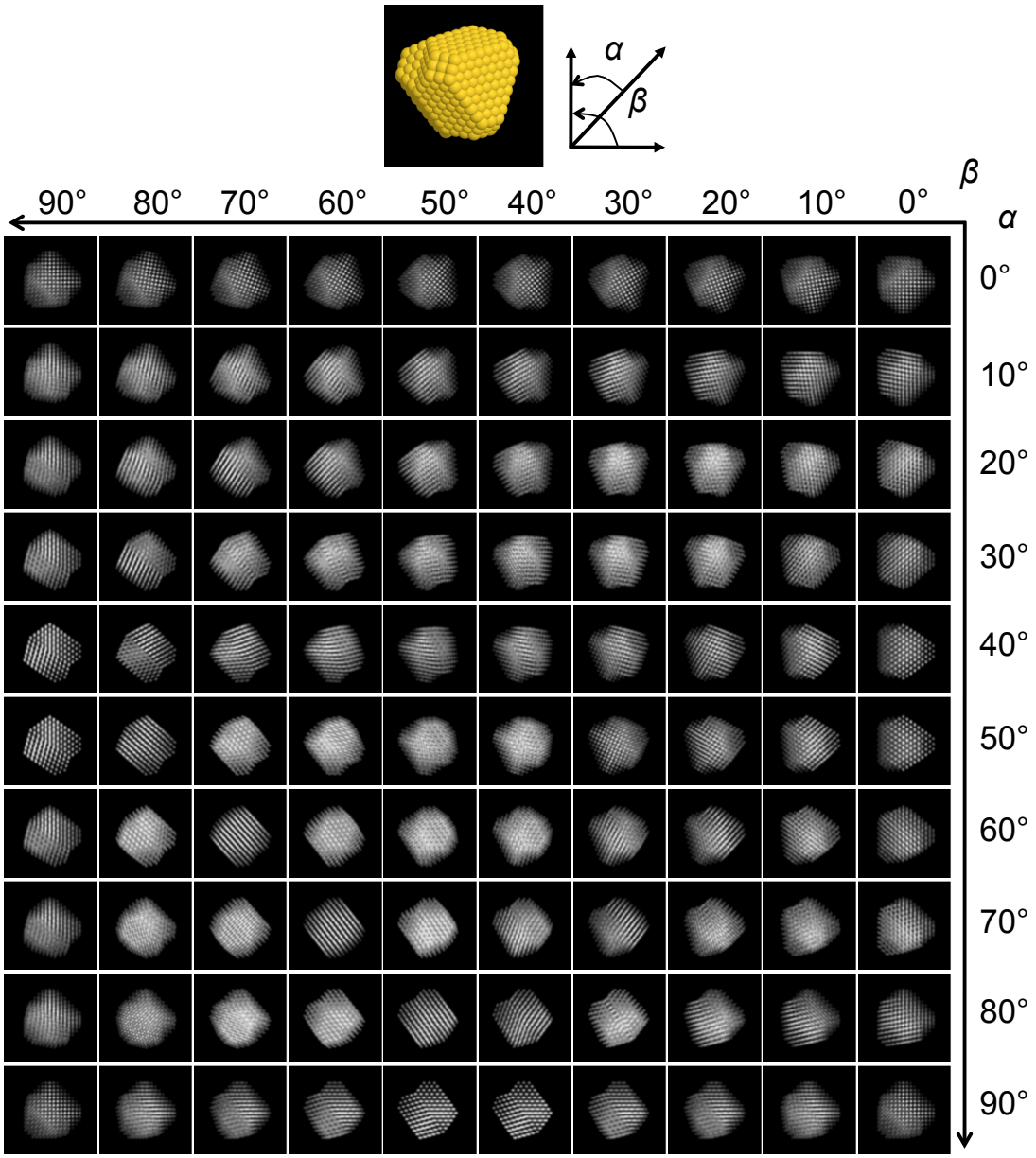

Figure 6.8: Kinematic simulation of single twinned TO_{861}.

cation. At some orientations where the twin boundary appears as a straight line, such as $(\alpha = 70, \beta = 60°)$, the pattern is the same as single crystal pattern $(\alpha = 60, \beta = 70°)$, which makes impossible to distinguish them.

In practice, clusters with multiple (>1) twinning planes can also exist. However, they

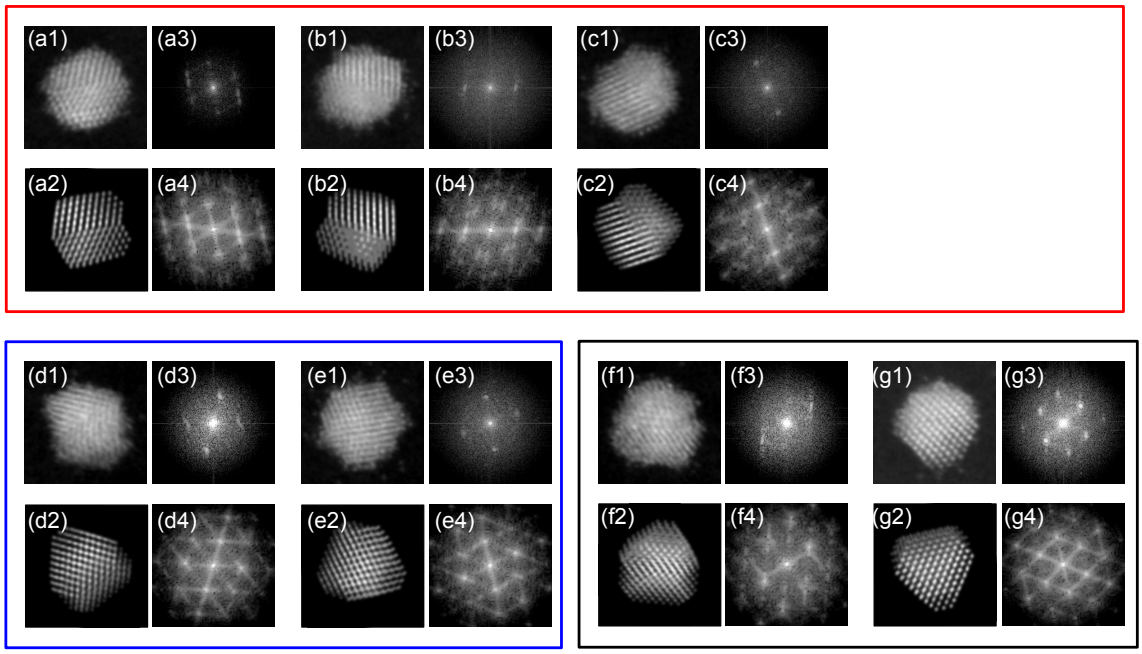

Figure 6.9: The comparison with the experimental image and the simulation of single twinned TO_{861}. (a1-g1) experimental images, (a2-g2) simulated image (a3-g3) FFT of direct images, (a4-g4) FFT of simulated images. The image patterns are placed into three groups boxed with red, blue and black colours.

are not popular for the reasons that the pairs of twinned boundary with a few atomic layers can be easily eliminated by the passage of a partial dislocation [122]. Nevertheless, this study of the single twinned model cluster shows that when the cluster is orientated with twin planes parallel or vertical to the electron beam, they can be identified as FCC in two dimensional projection.

6.3 Decahedron

In the Marks-Dh_{887} model cluster, there are 12 atoms in the central column and 2 atoms truncated at each corner. The Marks-Dh are observed more frequently in experiments than classic and Ino Dh because the truncation angles minimize its energy [122].

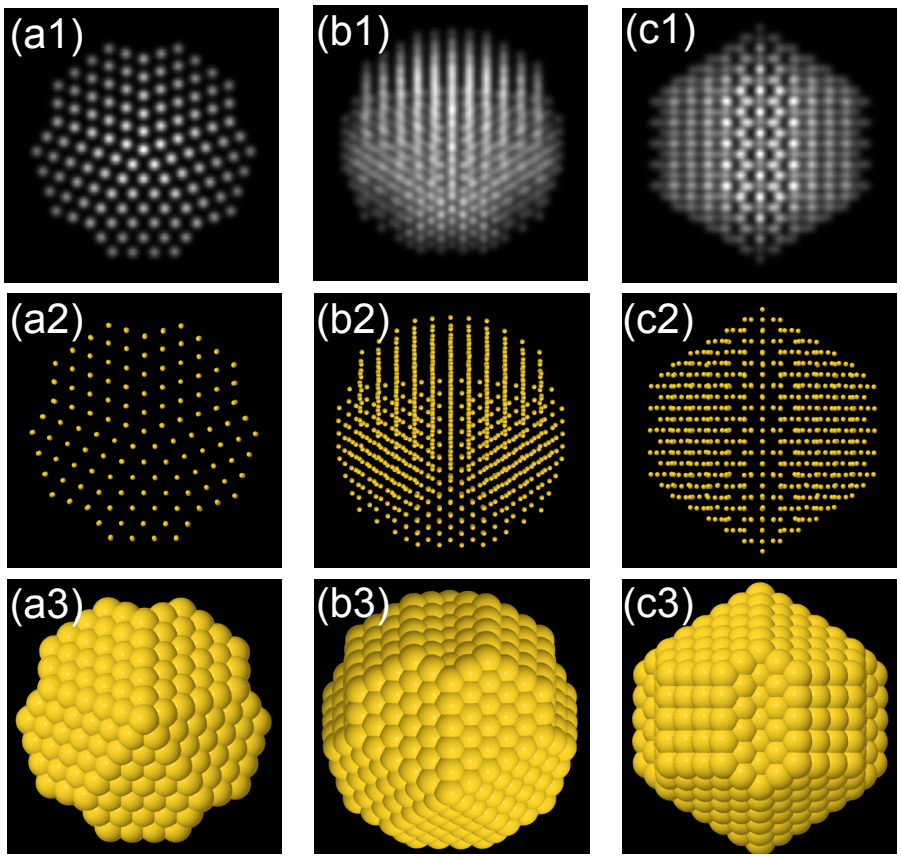

Figure 6.10: (a) < 110 > (b) < 111 > and (c) < 111 > orientated Dh_{887} model cluster. (a-c1) The kinematic simulation (a-c2) hard ball model with 15% van der Waals radius (a-c3) hard ball model with 100% van der Waals radius.

Figure 6.10 shows three main orientations (< 110 >, < 111 > and < 100 >) of the Marks-Dh. Figure 6.10 (a1-3) shows the cluster aligned along the five fold direction, which is the easiest way to identify the Dh. There is a five fold centre and the zone axis is parallel to the twin plane, so that no quasi-FCC subunits overlap. Figure 6.10 (b1-3) shows the < 111 > orientation, where the hexagonal pattern is visible (in the lower part of Figure 6.10 (b1)). This orientation has two fold symmetry, with both the right and left parts showing line-like fringes. Figure 6.10 (c1-3) shows a side view of the model cluster from one of the truncated angles in < 100 > orientation. This orientation has two fold

symmetry, with a hexagonal outline, and is mainly featured with lines.

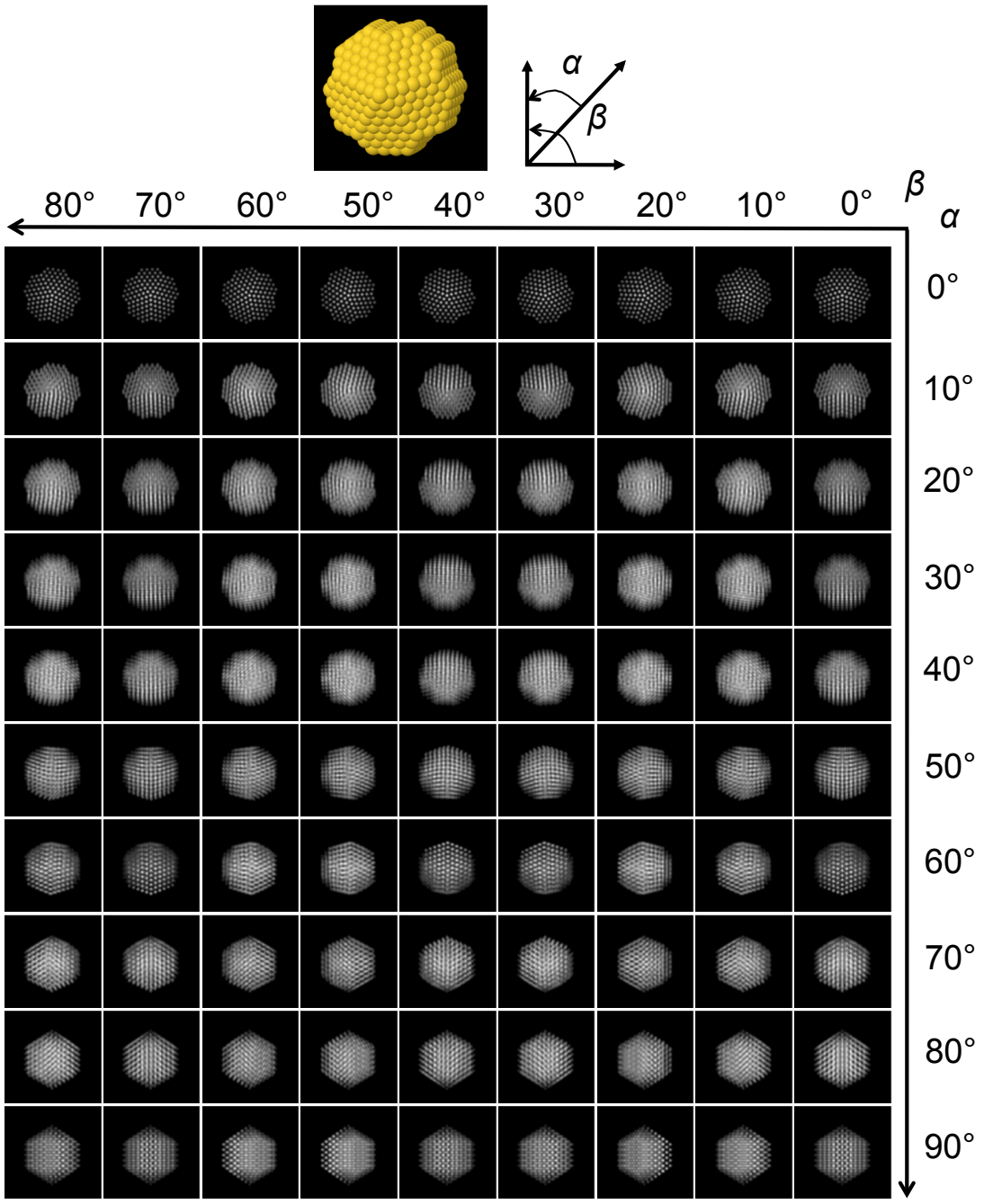

Figure 6.11: Kinematic simulation of Dh_{887}.

The kinematic simulation atlas for Marks-Dh_{887} is shown in Figure 6.11. The patterns can be either five fold, four fold or two fold symmetric, or non symmetric. There are five

types of the pattern:

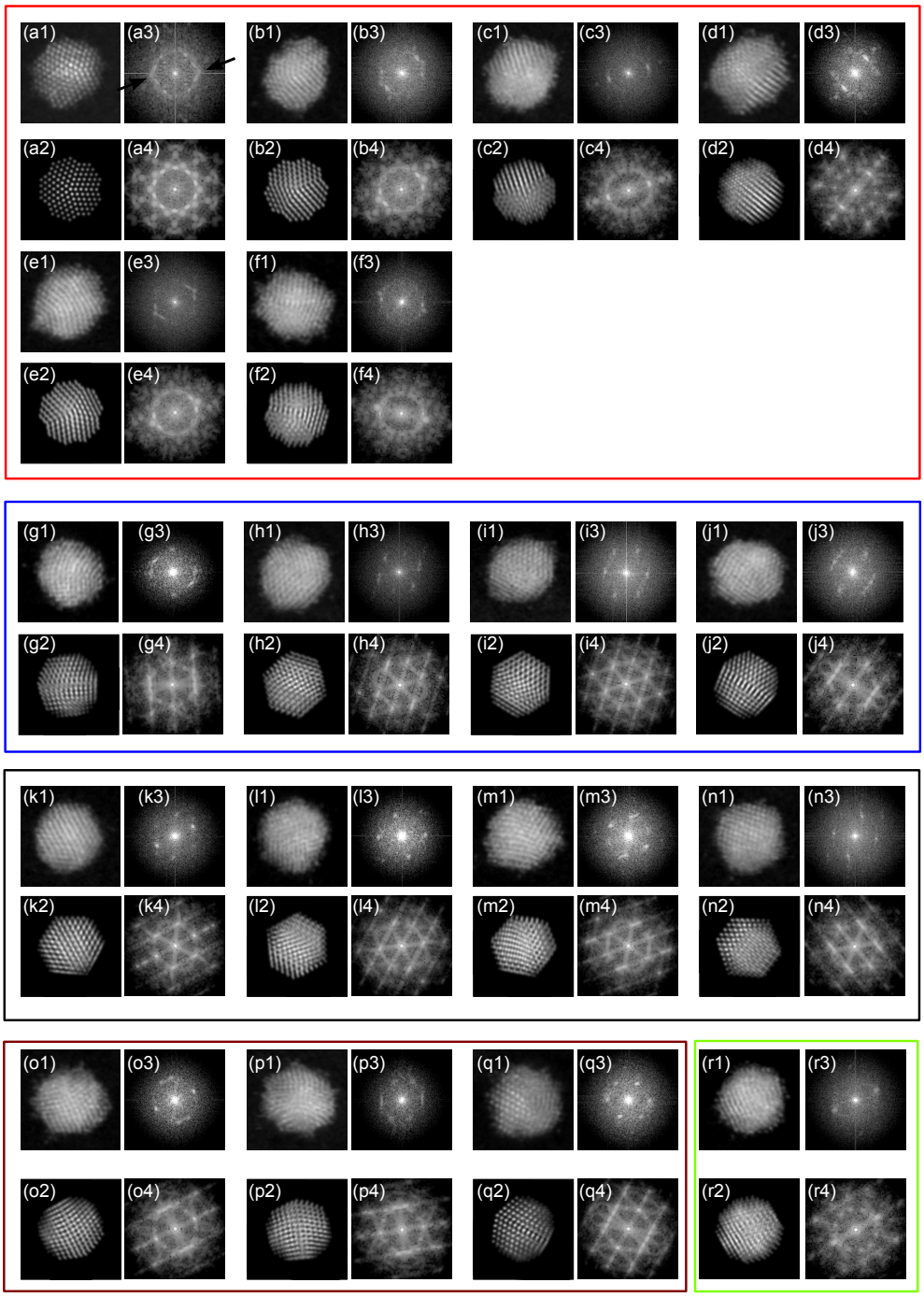

Figure 6.12: The comparison with the experimental image and the simulation Dh_{887}. (a1-r1) experimental images, (a2-r2) simulated image (a3-r3) FFT of direct images, (a4-r4) FFT of simulated images. The image features are placed into five groups labelled with red, blue, black, brown and green colours.

(1) With the model cluster orientated in $< 110 >$ direction or slightly off, such as ($\alpha = 0° - 10°, \beta = 0° - 90°$), the five segments are visible (exemplified in Figure 6.12 by the red box). They usually have triangle-like patterns in the FFT (indicated in Figure 6.12 (a3) by arrows).

(2) The model cluster is tilted between the $< 110 >$ direction and the side view, the simulation shows six sides with different lengths, and the pattern is not symmetric (exemplified in Figure 6.12 by the blue box). The FFT normally shows at least 6 spots.

(3) The side views of the cluster usually have six sides of approximately equal length (exemplified in Figure 6.12 by black box).

(4) The model cluster is tilted between $< 111 >$ to $< 100 >$. This shows a two fold symmetry and is exemplified in Figure 6.12 by the brown box.

(5) Between the orientation tilted from the five fold to the example shown in Figure 6.12 the brown box, the simulation shows a more complicated pattern (exemplified in Figure 6.12 by the green box).

6.4 Icosahedron

Figure 6.13 shows simulation of Ih with 6 shells. In Figure 6.13 (a), the model cluster is $< 110 >$ orientated and the simulation shows a ten fold symmetry with ring-like patterns whereas it is actually along the five fold symmetric axis of the model cluster. Each radial line in the simulation corresponds to a twin boundary. In this orientation, frequently, the centre appears a circular dot with a ring surrounding it, where the dot is an atomic

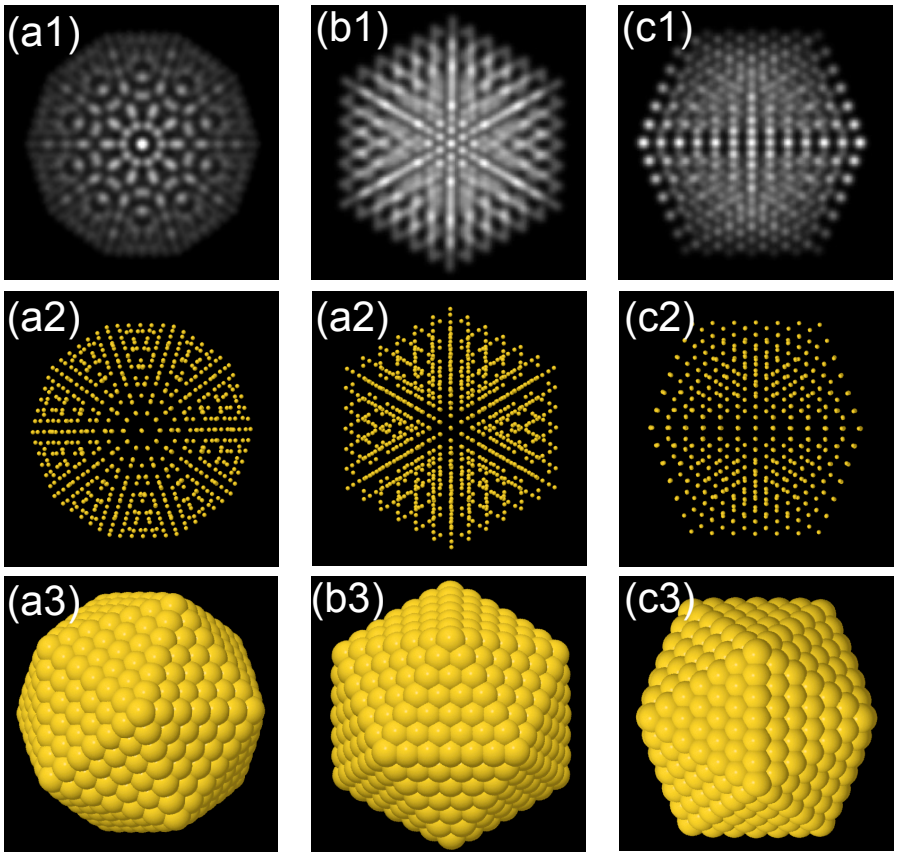

Figure 6.13: (a) < 110 > (b) < 111 > and (c) < 211 > orientated Ih_{923}. (a-c1) The kinematic simulation (a-c2) hard ball model with 15% van der Waals radius (a-c3) hard ball model with 100% van der Waals radius.

column and the ring is the overlapping of ten atoms. In Figure 6.13 (b), the model cluster is < 111 > orientated and the simulation shows a six fold symmetry, with radial lines. In Figure 6.13 (c) the model cluster is < 211 > orientated, and appears with four segments, with the upper and lower parts blurred and the right and left sides, showing {111} fringes (Figure 6.15 (c1)).

Figure 6.14 shows the kinematic simulation atlas for Ih_{923}. The feature is distinctive and relative easier to identify than other structures. It usually shows 2, 6 or 10 fold symmetry, with four types of the pattern. In type (1-3), the model cluster is orientated

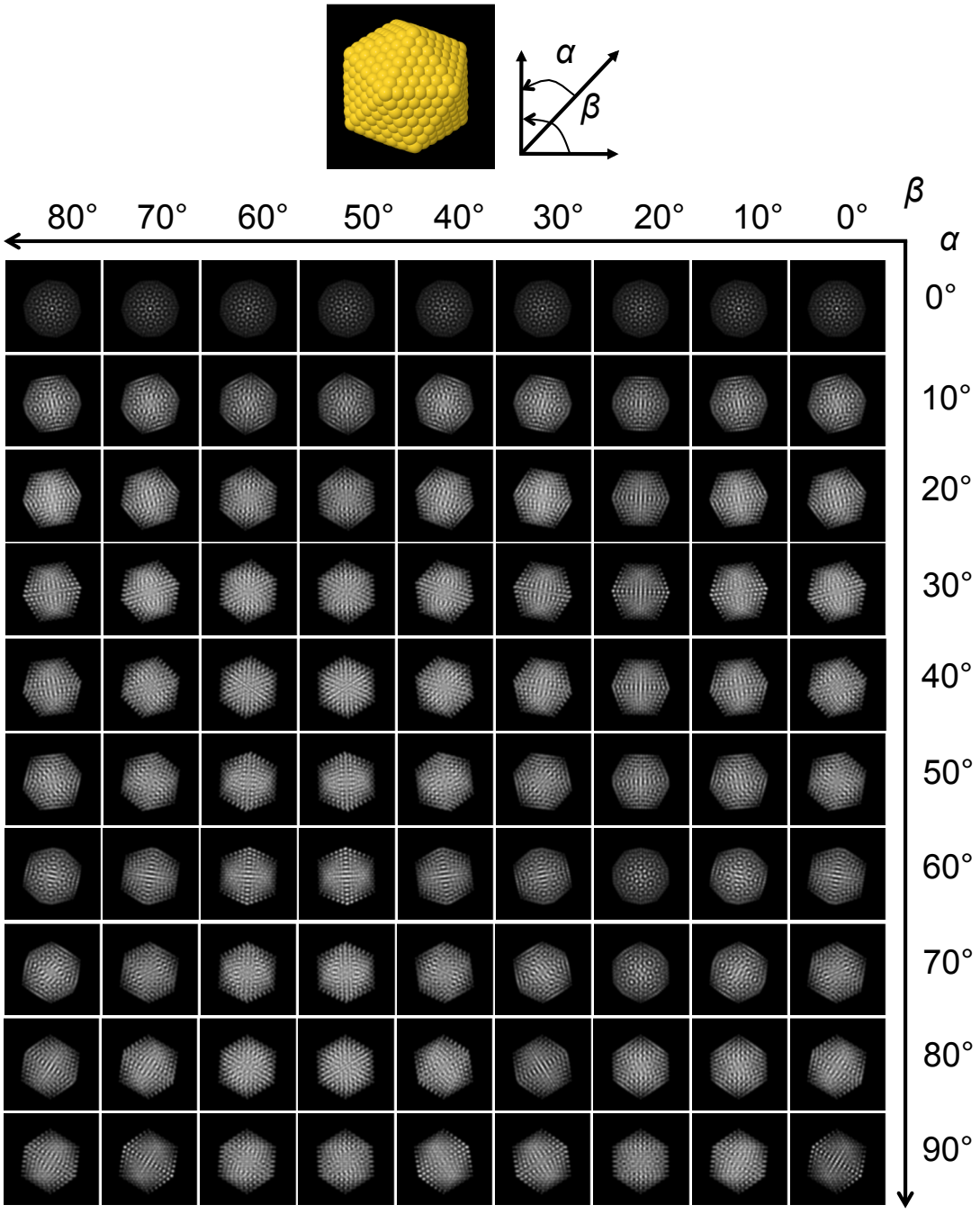

Figure 6.14: Kinematic simulation of Ih_{923}.

around $< 110 >$, $< 111 >$ and $< 211 >$ respectively and are exemplified in Figure 6.15 by red, blue and black boxes. The type (4) pattern is formed between these main

orientations, and usually shows two fold symmetry, as exemplified in Figure 6.15 by the brown box.

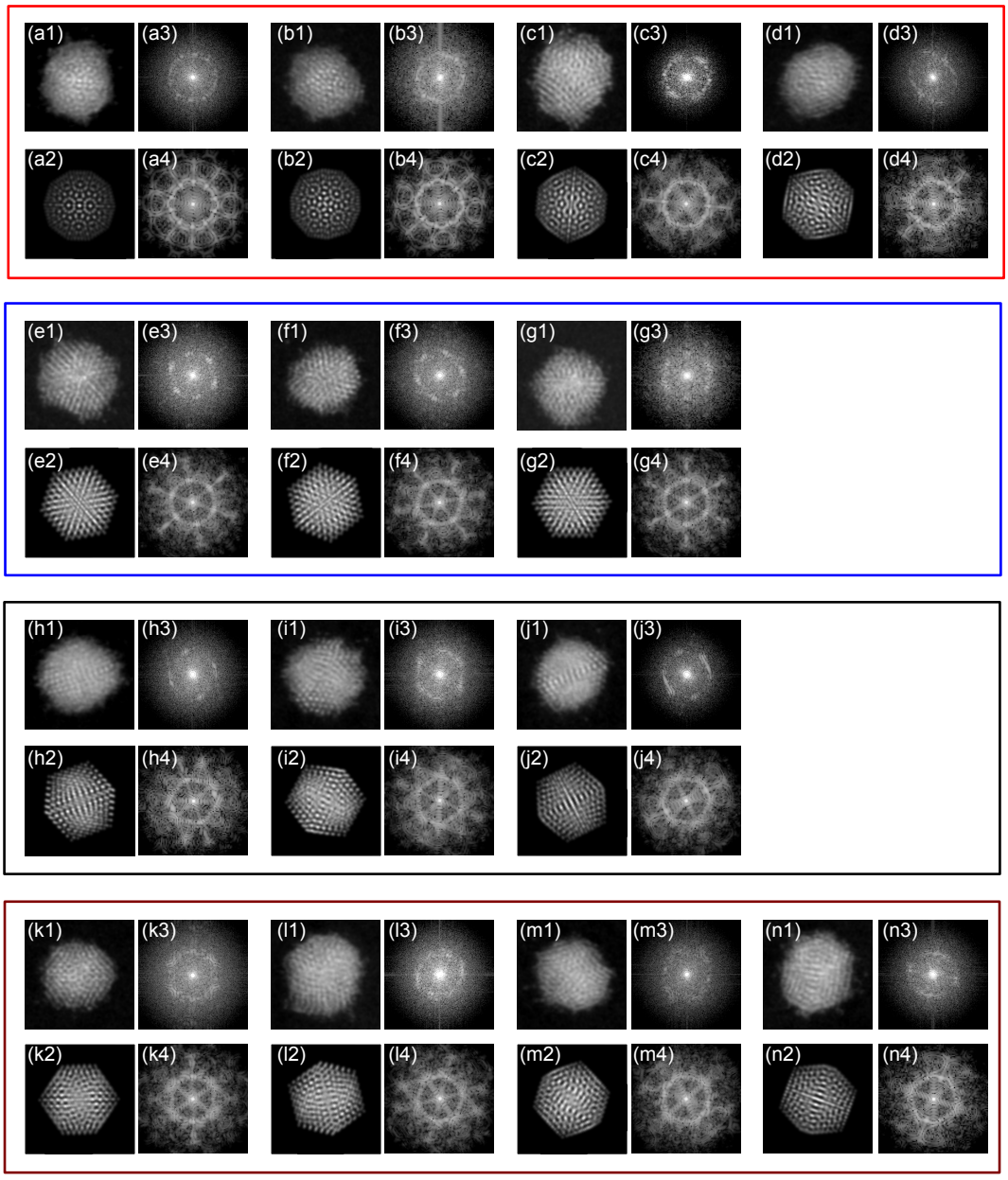

Figure 6.15: The comparison with the experimental image and the simulation Ih_{923}. (a1-n1) experimental images, (a2-n2) simulated image (a3-n3) FFT of direct images, (a4-n4) FFT of simulated images. The image features are placed into four groups labelled with red, blue, black and brown colours.

6.5 Summary

As it can be seen in the simulation, most patterns are quite distinctive. However, in practice, due to experimental noise in STEM images, some patterns can appear similar between structures. It mainly happens between single twinned FCC and Dh, such as $(\alpha = 70°, \beta = 30°))$ in Figure 6.8 and $(\alpha = 30°, \beta = 80°))$ in Figure 6.11. The errorbars included the Due to this issue, these similar clusters are put into the the error bars for both categories. Another source of error is where the patterns are unrecognisable with consideration of only these three categories. However this is very rare, and estimated to affect less than 10% of the experimental images.

Chapter 7

Structure formation mechanism

7.1 Introduction

Unlike their bulk counterpart, with only face-centred cubic (FCC) structure, nano gold can also present with multiply twinned structures such as decahedron (Dh) and icosahedron (Ih). These structures have unique properties in catalysis [58], optics [198], etc. However, with limited systematic experimental data available, to date, the formation mechanism of these structures is still the subject of debate. For instance, relativistic first principles calculations show that the energy crossover for gold Ih and other structures is 4-5 nm (at room temperature) for gold [96], while experimentally Koga et al. used inert gas aggregation method to produce Ih gold nanoparticles prevailing to 15 nm [135].

In this chapter, with a fixed nominal size of 887 atoms, which is deliberately chosen to avoid the geometrical magic numbers ($N = 10/3k^3 + 5k^2 + 11/3k + 1$, where k is the number of shells) where the cluster can form Ih, Dh and FCC with complete shells,

the kinetic behaviours of the structures are studied experimentally, as a function of the experimental conditions in the cluster source. The structural identification is based on visual inspection which is introduced in Chapter 6. In total, 2057 clusters have been investigated.

7.2 Cluster production

In this work, the size-selected Au clusters were generated using an in-house developed cluster source located in University of Birmingham [27]. This method of synthesis is usually referred as "free cluster" production. The clusters were formed via inert gas aggregation and soft-landed on amorphous carbon covered TEM grid with deposition energy 1eV/atom. The samples were supplied by Dr. F. Yin and Prof. R.E. Palmer.

As schematised in Figure 7.1, the cluster source has three parts: sputtering and cluster formation chamber, acceleration and focusing chamber, and mass selection chamber. In the sputtering and cluster formation chamber, which is cooled by the liquid nitrogen,

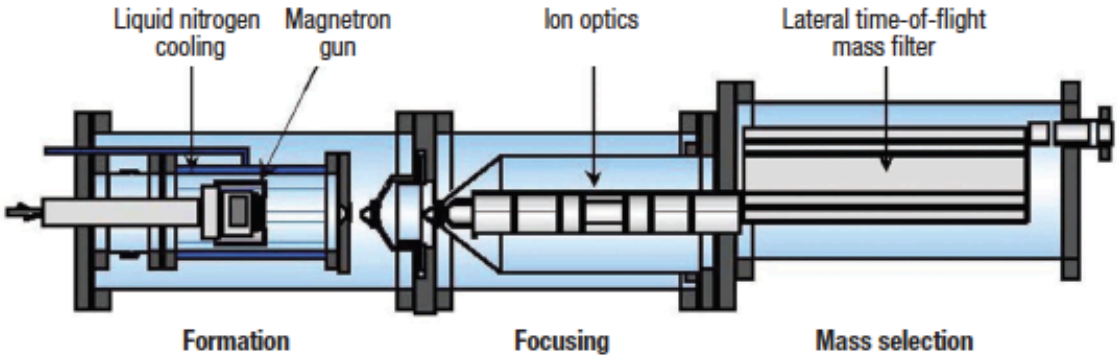

Figure 7.1: Schematic of the cluster source located in University of Birmingham. The drawing is reproduced from [199].

the sputtering gas (Ar) is injected from small orifices, and ignited by a high voltage. It sputters the Au atoms from the target with the help of magnetron and this process creates a dense vapour of atomic ions and small clusters [27]. He gas, which is injected from the back of the chamber, cools the Au atoms [27]. Clusters then start to form through collisions and then grow through the process of condensation [27]. The system is differentially pumped. The pressure in the formation chamber and focusing chamber are ~ 0.1 mbar and $\sim 10^{-7}$ mbar, respectively.

One of the advantages of the sputtering cluster source is that high proportion of the clusters are charged so that they can be accelerated and focused by ion optical components [27]. The clusters investigated in this chapter are positively (most single) charged. A lateral time-of-flight technique is applied to achieve accurate cluster size-selection using two opposite high voltage pulses to accelerate and decelerate the cluster beam perpendicular to its original direction [41]. The time that it takes cluster to travel from the accelerated region to the deceleration region is dependent on its mass/charge ratio, therefore, the time between the two pulses selects the mass of cluster. The beam is focused through an einzel lens. The sample holder is negatively charged, and the magnitude of this bias determines the deposition energy of the clusters on the substrate. Figure 7.2 shows an example of the mass spectrum with arrows showing how to determine the mass resolution of the clusters source experimentally. The current of single atoms is used to illustrate the resolution because this is the smallest unit of the cluster. Figure 7.2 shows the mass selection resolution for single Au atoms is $M/\Delta M=13$. The resolution of the cluster source is controlled by the exit slit opening [200]. The highest resolution of the

cluster source used in this work is up to 200. However, for the purpose of balancing of the yields, the resolution used in this work is 40.

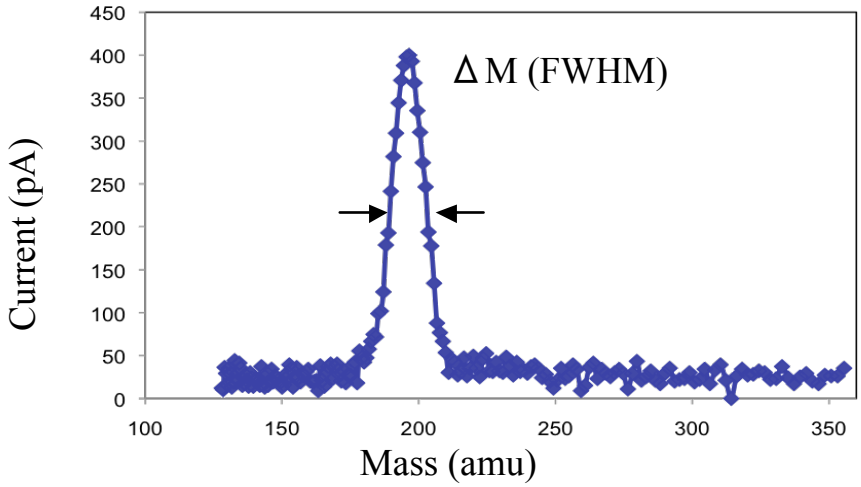

Figure 7.2: An example of mass spectrum of Au (Provided by Dr. Feng Yin). The peak occurs at the atomic mass of one gold atom with a resolution of M/ΔM=13.

7.3 Overview of Au_{887} clusters

Figure 7.3 shows an example of the "as-deposited" clusters on the carbon substrate. As can be seen in Figure 7.3 (a), most of the clusters are uniform in size and round in shape. A few clusters are slightly bigger than the other (one of these big clusters is indicated by an arrow in Figure 7.3 (a)). Figure 7.3 (b) shows a histogram of the integrated intensity of the clusters with two peaks. In the inset, the mean intensity value of the second peak is twice of the first peak, showing that the bigger clusters are dimers of Au_{887}. The formation of these dimers may be due to double-charged clusters, cluster diffusion on the surface or deposition of two clusters at the same place. Nevertheless, more than 95% clusters are

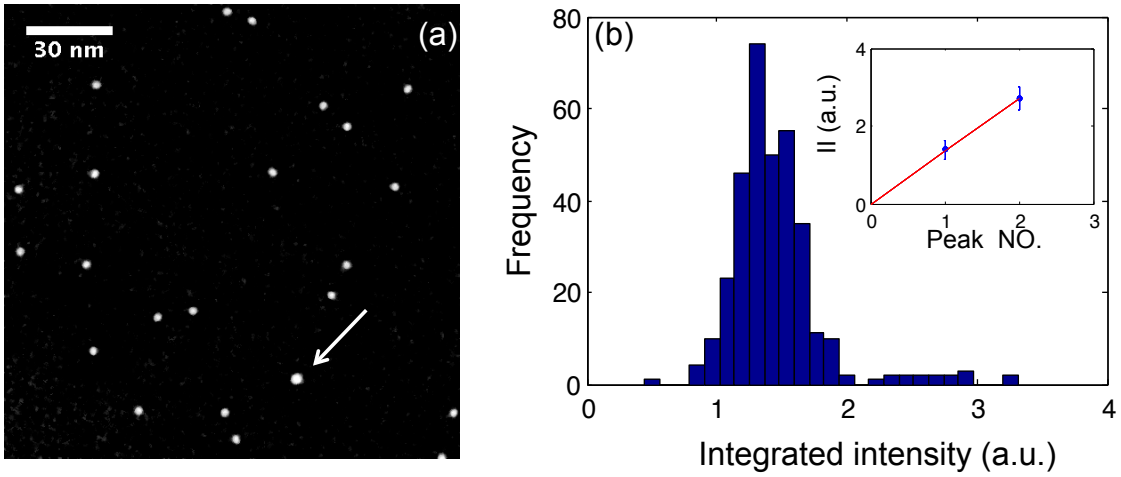

Figure 7.3: (a) An overview of the as-deposited clusters with deposition energy of 1 eV/atom. A dimer Au_{887} is indicated by an arrow. (b) The integrated intensity distribution of the clusters. There are two peaks in the histogram. The inset shows that the mean value of the second peak is twice as the first one (here II stands for integrated intensity).

monomer Au_{887}.

With the help of state-of-the-art aberration corrected microscope, the atomically resolved images of Au_{887} are possible. Figure 7.4 shows some examples of the experimental HAADF-STEM images of the Au_{887}. Instead of being FCC, like the bulk form of gold, these images show more complicated structures: (a-c), (d), (e) and (f) are Ih, Dh, FCC without and with twin boundary, respectively. The identification of these structures is possible using the combination of simulation and FFT approach, as described in Chapter 6.

7.4 Cluster production under different conditions

Unlike the result reported by Koga's group, where Ih dominates the structure at very large size (∼15 nm) [135], in most cases the clusters produced using the inert gas aggregation

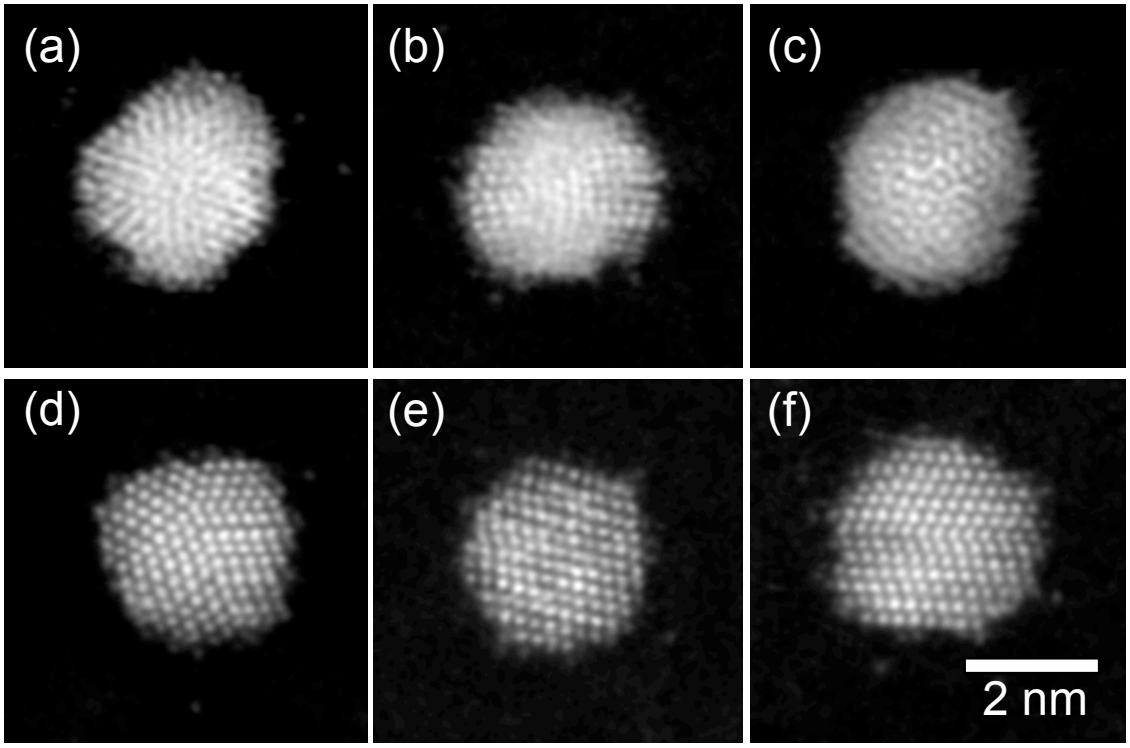

Figure 7.4: Examples of the atomic resolved Au_{887} HAADF-STEM images. (a)-(c) are Ih (d) Dh (e) single crystal FCC and (f) Single twinned FCC. These image are filtered from the original image with 2 pixels Gaussian convolution.

cluster source show a mixture of different structures. This implies that the fraction of different structures can be tuned by varying experimental parameters. In this work, the influence of four parameters in the sputtering and cluster formation chamber are considered: condensation length (CL), sputtering power (SP), argon flow (AF) and helium flow (HF). For each experimental run, more than 100 hundred clusters has been imaged and analysed to achieve statistical validity.

Figure 7.5 shows the fractions of structure as a function of systemically varying the different experiment parameters. As mentioned in Chapter 6, the Ih images are the most distinctive and so that have the smallest error bar. For some orientations, Dh and (mostly

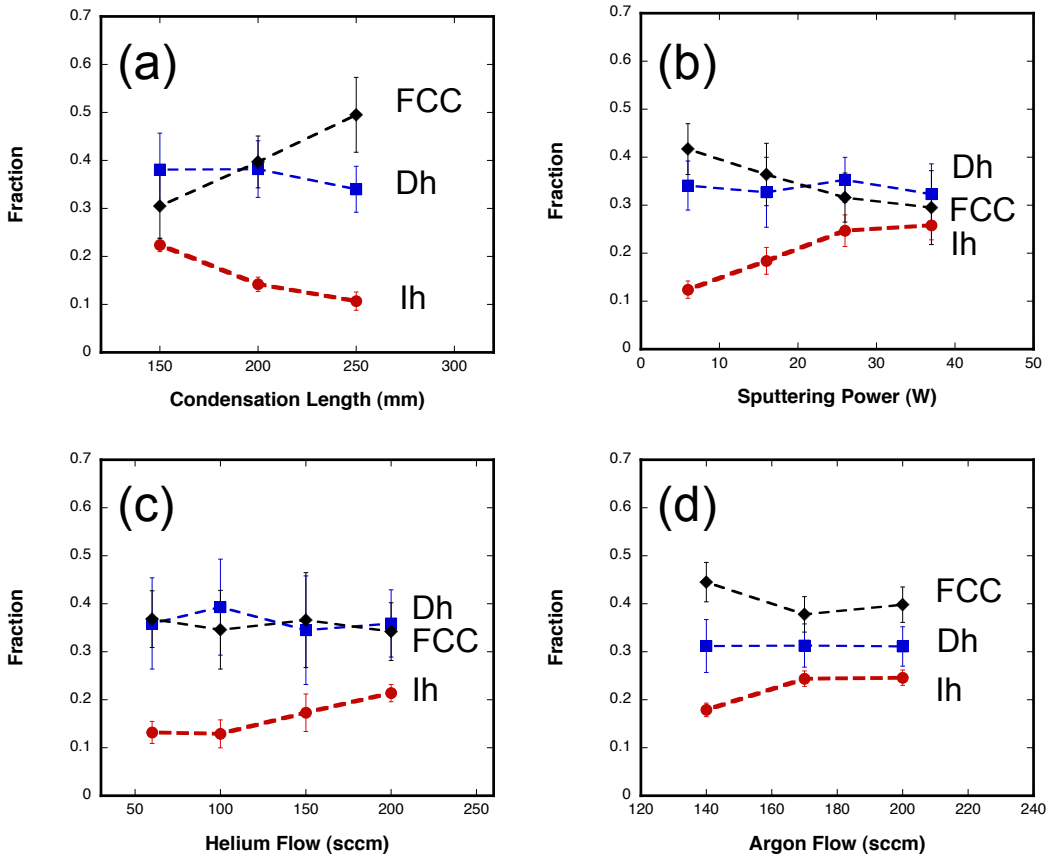

Figure 7.5: (a)The fractions of structure as a function of condensation length. (b) the fraction of structures as a function of sputtering power. (c) The fractions of structures as a function of He flow. (d) The fraction of structures as a function of Ar flow.

single twinned) FCC are very similar, which leads to less than 10% error bar. Table 7.1 summarises the experimental setting parameters. It also lists the reading of Pirani gauge 5, Pirani gauge 4, sputtering voltage (S.V.), nozzle diameter (N.D.) and the deposition beam current (current). The Pirani gauge 5 and 4 measure the pressure inside and outside the sputtering chamber respectively. Even with the same Ar and He flow, these two values are not necessarily the same, as the nozzle size can also play a role, which is adjusted to optimise the yield of the cluster. However, the result presented in this study is comparable as the nozzle size was unchanged within the same experiment run (indicated in Table 7.1).

In Table 7.1, the reversed triangles indicate the experimental parameters that are changed for each particular experimental run.

Table 7.1: Experimental parameters in the sputtering and cluster formation chamber

Expt. Run.	CL (mm)	SP(dc) (W)	AF (sccm)	HF (sccm)	Pirani5 (mbar)	Pirani4 (mbar)	S.V. (V)	N. D. (mm)	Current (pA)
1	▽150	25	180	200	0.20	8.7×10^{-3}	314	1.38	18
	▽200	25	180	200	0.20	8.7×10^{-3}	314	1.38	36
	▽250	25	180	200	0.20	8.7×10^{-3}	314	1.38	40
2	150	▽6	180	200	0.88	8.6×10^{-3}	283	0.68	18
	150	▽16	180	200	0.88	8.6×10^{-3}	307	0.68	57
	150	▽26	180	200	0.88	8.6×10^{-3}	312	0.68	23
	150	▽37	180	200	0.88	8.6×10^{-3}	321	0.68	10
3	200	25	200	▽ 60	0.3	5.5×10^{-3}	411	3.22	8
	200	25	200	▽100	0.44	5.9×10^{-3}	411	3.22	15
	200	25	200	▽150	0.5	7.2×10^{-3}	411	3.22	28
	200	25	200	▽200	0.56	8.7×10^{-3}	411	3.22	28
4	200	25	▽140	200	0.53	7.8×10^{-3}	338	2.09	7
	200	25	▽170	200	0.65	8.2×10^{-3}	335	2.09	14
	200	25	▽200	200	0.79	8.9×10^{-3}	334	2.09	14

7.4.1 Condensation length

The condensation length in the cluster source is the distance between the sputtering target and the nozzle, which can be tuned from 150 mm to 250 mm. Changing the condensation length is realised by moving the sputtering target backwards and forwards. It can greatly influence cluster formation. For example, the peak of the size distribution of Ag clusters was found to be shifted by $\sim 20\%$ towards larger masses when the aggregation distance was increased by $20 - 30$ mm [199]. In this experiment, Experiment Run 1 in Table 7.1 indicates that when the condensation length is increased from 150 to 250 mm with other parameters maintained constant, the current (i.e. the abundance of the Au_{887} cluster is approximately doubled, showing that the size distribution of the cluster has changed. As

increasing the condensation length, the structure distribution can also be changed: the fraction of Ih decreases and the FCC proportion increases (Figure 7.5 (a)).

7.4.2 Sputtering power

The sputtering in this cluster source can be generated by either rf or dc power. In this experiment, the dc sputtering is used. As can be seen, when the sputtering power is increased from 6 W to 37 W, both sputtering voltage and current increase from 283 V to 321 V and from 21 mA to 115 mA respectively. This implies that increasing sputtering power generates more sputtered atoms with each atom having higher kinetic energy. In Figure 7.5 (b) as the sputtering power is increased, the fraction of Ih increases and the fraction of FCC decreases. However, the current increases at the beginning (6 W and 16 W) and later drops (26 W and 37 W) as a function of sputtering power (Table 7.1).

7.4.3 Helium flow

The purpose of injecting He flow is to "cool" the Au atoms sputtered from the target with high kinetic energy. This changes the pressure inside the chamber. In this cluster source the helium flow can be tuned from 0 to 200 sccm. Table 7.1 Experiment Run 3 shows that increasing the He flow also increases both the (total) pressure inside the chamber (Pirani 5) and outside the chamber (Pirani 4). The pressure difference is also increased, which implies that the clusters are pushed out of the chamber quicker. However, the contribution of the He to the yield (Current) of Au_{887} is saturated when the flow exceeds 150 sccm. In Figure 7.5 (c), as increasing the He flow, the fraction of Ih increases and the

fraction of FCC decreases.

7.4.4 Argon flow

Ar is employed to sputter the target. Changing the Ar flow leads to very small variation ($\sim 1\%$) of the sputtering voltage in Table 7.1 experiment No. 4. It indicates that the sputtering current is rather stable (less than $\sim 0.5\%$ variation) and most of the increased Ar atoms is not used to sputter the target. So, in the Table 7.1 Experiment Run 4, increasing the Ar flow increases the pressure inside the chamber. Ar flow can be tuned from 0 sccm to 200 sccm in this cluster source. However, similar to He flow, the effect of Ar flow to the current of the Au_{887} is saturated at 170 sccm. In Figure 7.5 (d), increasing the Ar flow, causes that the fraction of Ih to increases and the fraction of FCC to decreases.

7.5 Discussion

As can be seen in this experiment, there are six points need to note:

(1) As the mass-selector is located behind the cluster formation chamber, when the experimental condition is changed, it affects (the structures of) all the sizes. The size usually follows a long-normal distribution and varies against the experimental conditions. However, in this thesis, only the size of 887 is selected. So when the size distribution is shifted, the abundance, i.e. the current in Table 7.1, of the Au_{887} changes. However, particularly in Experiment Run 2, it can been seen that the current (thus the size distribution and the central size) does not follow the trend of none of Ih, Dh and FCC in Figure

7.5 (b). This experiment demonstrates that the size and the structure of the cluster can be tuned independently.

(2) In this experiment, shortening the condensation length, increasing the sputtering power has the most influence on the structure distribution, i.e. leads to more than 10% change of the Ih fraction. When the condensation length is shorter, to reach the same size (887 atoms in this case) so that they can be selected by the mass filter, the clusters have to grow faster. For higher sputtering power, as the Au atoms have higher kinetic energy, it takes longer distance (from the target) to cool them so that they can nucleate. In this sense, the effective cluster formation distance actually becomes shorter. Therefore increasing the sputtering power is similar to shortening the condensation length. Both of them are fast growth conditions, which lead to more Ih.

(3) Increasing He and Ar flow all have a positive effect on Ih formation. When the He and Ar flow is increased the pressure inside the chamber pushes the clusters through faster and it confirms the point (2). However, as shown in the Figure 7.5 (c) and (d) (particularly for the Ih fractions), it seems the influences of the He and Ar flow on the structure distribution are "saturated" when the flow is high, which is coinciding with their influence on the Current in Table 7.1.

(4) (2) and (3) show that all of these experimental conditions are fast condensation condition for gold cluster. It proves that the Ih prefers non-equilibrium growth condition. This is comparable with another results published using chemical method [144], which shows that the Ih prefers to form in the solution containing higher concentration of the Au precursor. As widely accepted, the Ih structure is the lowest energy structure for

small cluster among Ih, Dh, FCC. However, along the cluster formation, the energy of Ih become not favourable as the strain inside the cluster increase and the Ih structure become a local minimum energy structure. If the growth condition is fast enough, Ih clusters do not have enough time to find their global energy minimum, i.e. transform to another structures and are trapped in the Ih well.

(5) Even though the error bar of the FCC is slightly bigger than Ih, the trends of the Ih and FCC fractions are always opposite. This indicates that some Dh or Ih transforms to FCC during growth when more equilibrium experimental conditions are used. It indicates that the FCC structure is the most favoured structure at this size.

(6) In this experiment, the change of Dh is rather small. However, it does not mean the Dh is independent of the experimental condition. As the Dh is a intermediate structure between Ih and FCC in terms of energetics, it is possible that structural transformations (Ih to Dh and Dh to FCC, or vice versa) between different experimental condition cancel the variation of the Dh fraction.

To conclude, in this chapter, the conditions of producing different structures are explored systemically. The Ih prefers the fast condensation condition while the FCC prefers the opposite. The highest percentage of the structures that can be produced is probably limited by the design of the cluster source.

Chapter 8

The stability of the structures

8.1 Introduction

Studying the relative stability of the structure of the clusters is crucial to understand the potential energy surface of the cluster. It is particularly interesting for multiply twinned particles (MTP) which are considered to be energetically favoured at small size. In the literature, the relative energy difference and the energy minima structures have been calculated in many ways. However, the potential energy surface is much complicated than that because of the existence of the local minima and the energy barriers (valleys and hills on the potential energy surface). On the other hand, experimentally, the stability of clusters can be studied by heating/cooling or electron beam irradiation. Both of them can induce the structural transformation. At the size of 887, Koga's experiment [6] shows that by heating the cluster (to 1173 K) in vacuum, the icosahedron (Ih) transforms to decahedron (Dh). But for Dh to face centred cubic (FCC) transformation, it needs to overcome

the melting temperature. The heating shows an overall structural transformation. Wang and Palmer published another experiment recently to look at individual clusters [147]. In this method, using the electron beam to irradiate the cluster (containing 923 atoms, where 923 is the magic number of Ih, Dh and FCC), Ih to Dh (29 out of 42), Ih to FCC (12 out of 42) and FCC to Dh (1 out of 19) transformations are found. It implies that the ground state is Dh, which is in-consistent with the theoretic calculation which shows that the lowest energy structure is FCC at this size.

In this work, the stability of the cluster is studied by the electron irradiation, taking advantage of the real-time observation in the microscope, with the size of 887, which is a geometric magic number of Marks-Dh. As the structural transformations are induced by the electron beam effect, which is a very complex phenomenon, some possible effects are discussed first. Then three types of the structural transformations are described to understand the mechanisms. All the orientations of cluster hard ball models in this chapter are based on the comparison of the experimental images and simulations, and these models can be put upside down relative to the substrate without affecting the simulation. So for each experimental image, there are at least two possible arrangement of the hard ball model. However, only one model is illustrated in this chapter for the sake of clarity.

8.2 The electron beam effect

In this study, the electron irradiation is to use the electron beam to scan to cluster frame after frame. The electron dose was chosen to be 35.1 pA (1.2×10^5 $e^-/Å^2$/frame), and

the scanning window was 10.5×10.5 nm^2 (512×512 pixels), with 20 μs dwell time at each pixel. Thus the scanning time was 10.2 ms for each line and 5.24 s for the whole scanning window. The time interval between successive images is 6 s. In total, for each cluster, 100 frames were obtained taking 10 mins. However, it is important to note that during the scanning, the probe and the particle are not interacting constantly, as the particle do not fully occupy the scanning window. If for a 3 nm (in diameter) particle, the interaction duration is about 0.37 s for each frame.

Before introducing the experimental result, the order of magnitude of the energy needed to cause the structural transformation should be estimated to consider the possible mechanisms. One important process in the structural transformation is the slip of the subunits, which needs to overcome a energy barrier. For gold, the energy barrier is 3.5×10^{-3} eV/Å^2 [201]. For a twin with area of 300 Å^2, the energy barrier is about 1 eV. Another important parameter is the cohesive energy of gold 3.84 eV/atoms [165].

As the electron beam is focused into a tiny spot, the influence of the electron beam is not negligible for these ultra small clusters. In fact, it is the electron beam that induces this transformation effect. With consideration of the result, four aspects of the radiation of the electron beam are investigated: (1) thermal heating effect, (2) the charging effect, (3) electron beam sputtering and (4) the momentum transfer.

8.2.1 Heating

In the case of STEM, the probe is so fine that the heating of the local region is an issue, especially for small clusters which have lower melting temperature than the bulk

form. Here the model is simplified to estimate the upper boundary of the substrate temperature. The energy input is mainly from the inelastic scattering, where the electron-electron collision efficiently transfers energy [202]. The mean free path of the inelastic scattering d_{mfp}, is estimated to be 120 nm [203]. Using 1000 eV to estimate the mean energy loss per inelastic collision $\bar{E}$ is sufficient enough as the typical energy loss is a few eV up to hundreds of eV [204]. The carbon film has a thickness t_c of about 20 nm. The beam current I_b used is 35.1 pA. Thus the heat generated in the specimen per second is $I_b\bar{E}t_c/ed_{mfp}$.

The heat dissipation are due to both radial conduction and radiation. However, the contribution of radiation is usually small and negligible [202]. Using the equation considering only the thermal conduction [202],

$$I_b\bar{E}t_c/ed_{mfp} = 4\pi\kappa t_c\Delta T/(0.58 + 2\ln(2R_0/d_b)), \tag{8.1}$$

where κ is the thermal conductivity for carbon (0.2 W/m/K [205]). R_0 is the distance that to be considered, d_b is the incident beam diameter. Here only the region of the probe is concerned so that $R_0 = d_b$. The temperature rise rate can be obtained as 0.23 K per second. Considering the dwell time per pixel (20 μs), the maximum temperature rise would not exceed 1 mK. When the probe moves to another place, the heat quickly dissipates.

Another issue is the temperature gradient within the cluster. A calculation conducted by Dundurs shows that for the size of the 25 Å gold particles under TEM, the temperature

difference is about 10^{-6} K in TEM [206]. Under the focused beam condition, this temperature is estimated to be less higher than two orders of magnitude (the size of particle to the size of the focused beam).

Even through the substrate temperature and the temperature variation within the cluster is very small (compared with the room temperature), it is important to note that the conduction between cluster and the substrate is not necessarily good depending on the contact area between the cluster and substrate [207]. With very small contact area, for example the cluster sits on a point defect, the heat is more likely to accumulate.

8.2.2 Charging effect

The charge effect was suspected to be a possible reason for the translational and rotational motion of the cluster in Ijima's experiment [206] . However, in this case, both gold and amorphous carbon are good conductors. For the electrical conductivity, amorphous carbon is 10 $\Omega^{-1}m^{-1}$ [208], which is at least two orders of magnitude higher than silicon used in Ijima's experiment [209, 210]. This reduces the possibility of accumulation of charge. If there is a temporary charge effect, it usually involves the movement of the cluster (such as detaching from the substrate).

8.2.3 Knock on effect

Another concern is that during the image acquisition, if the surface atoms are knocked off by the electron beam. The theoretic calculation shows that 200 keV electron beam can not knock off the atoms from gold bulk material [211]. However, for nanoparticles

this might become possible because the surface atoms have more dangling bonds and are more mobile. Figure 8.1 shows the integrated intensity over the one cluster as a function of the scanning frame number. This indicates that the integrated intensity does not suffer loss with scanning, which indicates that the mass of the cluster remains constant and the knock-on effect as well as atomic evaporation is negligible.

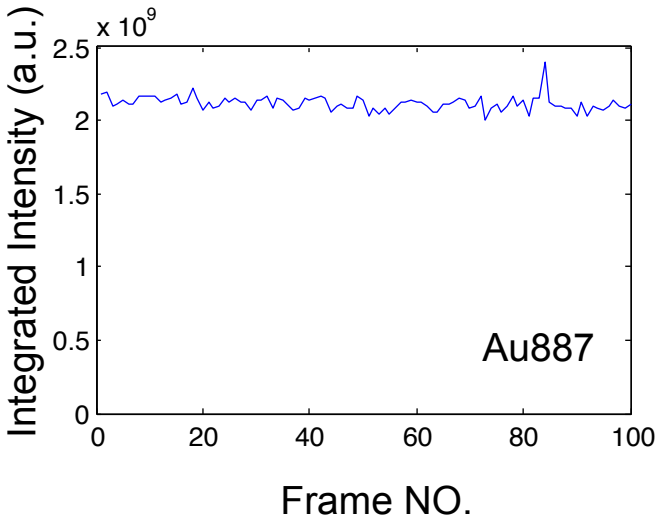

Figure 8.1: The integrated intensity of Au_{887} as a function of the elapsed time with the electron dose of 1.2×10^5 $e^-/Å^2$/frame.

8.2.4 Momentum transfer

Due to the scanning nature of HAADF-STEM, there are two types of the momentum transfer considered: the horizontal and vertical momentum transfer (v_1 and v_2 respectively in Figure 8.2). To make this effect more comparable with other effects, both of them are estimated with the unit of energy (eV).

The horizontal momentum transfer is from the scanning coil shifting the electron beam.

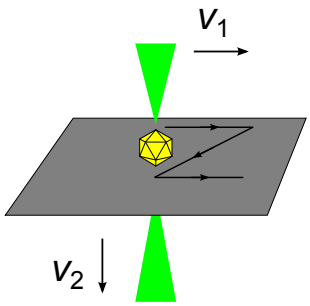

Figure 8.2: Schematic of the horizontal and vertical momentum transfer of the electron beam.

The beam shift velocity is 1×10^{-6} m/s (pixel size/dwell time). The kinetic energy of each electron at the horizontal direction is $(m_e v_1^2)/2$=3×10^{-24} eV. The total transferable kinetic energy rate is 5.5×10^{-16} eV/s, which is extremely small and can be neglected.

The vertical speed, v_2, of the electron beam is due to the acceleration, which is 2.1×10^{8} m/s. The maximum energy that can transfer to the atomic nucleus is [202]

$$E_{max} = E_0(1.02 + E_0/10^6)/(465.7A), \tag{8.2}$$

where E_0 and A are the incident beam energy (E_0 = 200 keV), and atomic mass number (197) respectively. It gives E_{max} =2.7 eV. This energy is considerably high and possibly sufficient to move atoms, especially in the case of backscattering [202].

8.3 The structural transformation

The structural fluctuation of nanoparticles under electron microscopy was firstly reported by Ijima [7]. In the work presented in this study, the cluster structural transformation has been systematically studied for 144 different clusters (50 Ih, 48 Dh, and 46 FCC

in their initial structure). During 10 min scanning of cluster, it is found that Ih can transform to either Dh (42 out of 50) or FCC (8 out of 50), while Dh can only transform to FCC (17 out of 48). Because of the drift and defocusing of the probe or even quasi-melting/melting of cluster, not all of the images show recognizable structure. Here the final structure means the last recognisable structure. Figure 8.3 shows examples of the structural transformation observed in experiment.

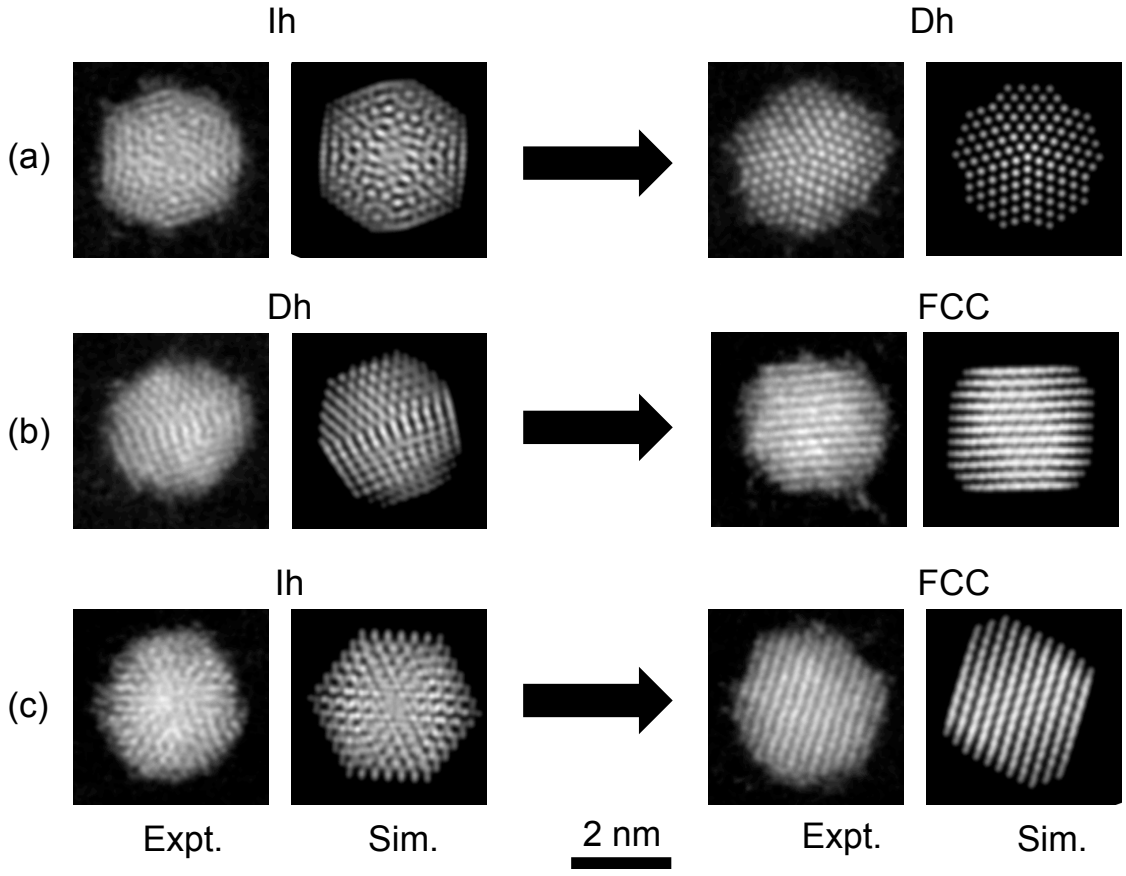

Figure 8.3: Experimentally observed structural transformation of Au_{887}. The left column is the experimental images with 2 pixel Gaussian blurred and the right column is the kinematic simulation. The experimental images share the same scale bar at the bottom. (a) Ih to Dh (b) Dh to FCC (c) Ih to FCC.

8.3.1 Ih to Dh structural transformation

Figure 8.4 shows the structural transformation from Ih to Dh. Figure 8.4 (a) are the successive images during structural transformation. Figure 8.4 (b1-b2) are the magnified experimental images. Figure 8.4 (c1-c2) are the simulated HAADF-STEM images of corresponding experimental frames. Using the simulation, the orientation of the cluster can be found, these are shown with hard ball models in Figures 8.4 (d1-2) and (e1-2) for around $< 110 >$ orientation. Frame 16 and 18 show similar features indicating that the cluster does not undergo significant rotation. This may be due to the cluster being stabilised by sitting on a defect of the substrate. After being under the electron beam for 1 min 48 s, the structure transforms from Ih to Dh. The transformation occurs in less than 6 s.

The red arrows in the Figure 8.4 (e2) indicated two of the vertexes of the Ih and the red lines show the corresponding twin planes before structural transformation. In Figure 8.4 (e3), after the structural transformation, these two twin planes disappear and a new twin plane forms in between.

The mechanism of the Ih to Dh structural transformation has been proposed by Koga et al. [6] and illustrated in Figure 8.5. This mechanism involves a cooperative solid-solid slip-dislocation. The total number of twin planes is 30 in Ih and reduced to 5 in Dh. 15 out of 30 twined planes emerge to 5 (3 to 1 each, O'OD, O'CD, O"OC in Figure 8.5 (a) into O"O'OCD in Figure 8.5 (b) for example). The other 15 of them disappear by slip (OAD, OBC, OAC for example). In Figure 8.5 (c) and (d) the middle subunits

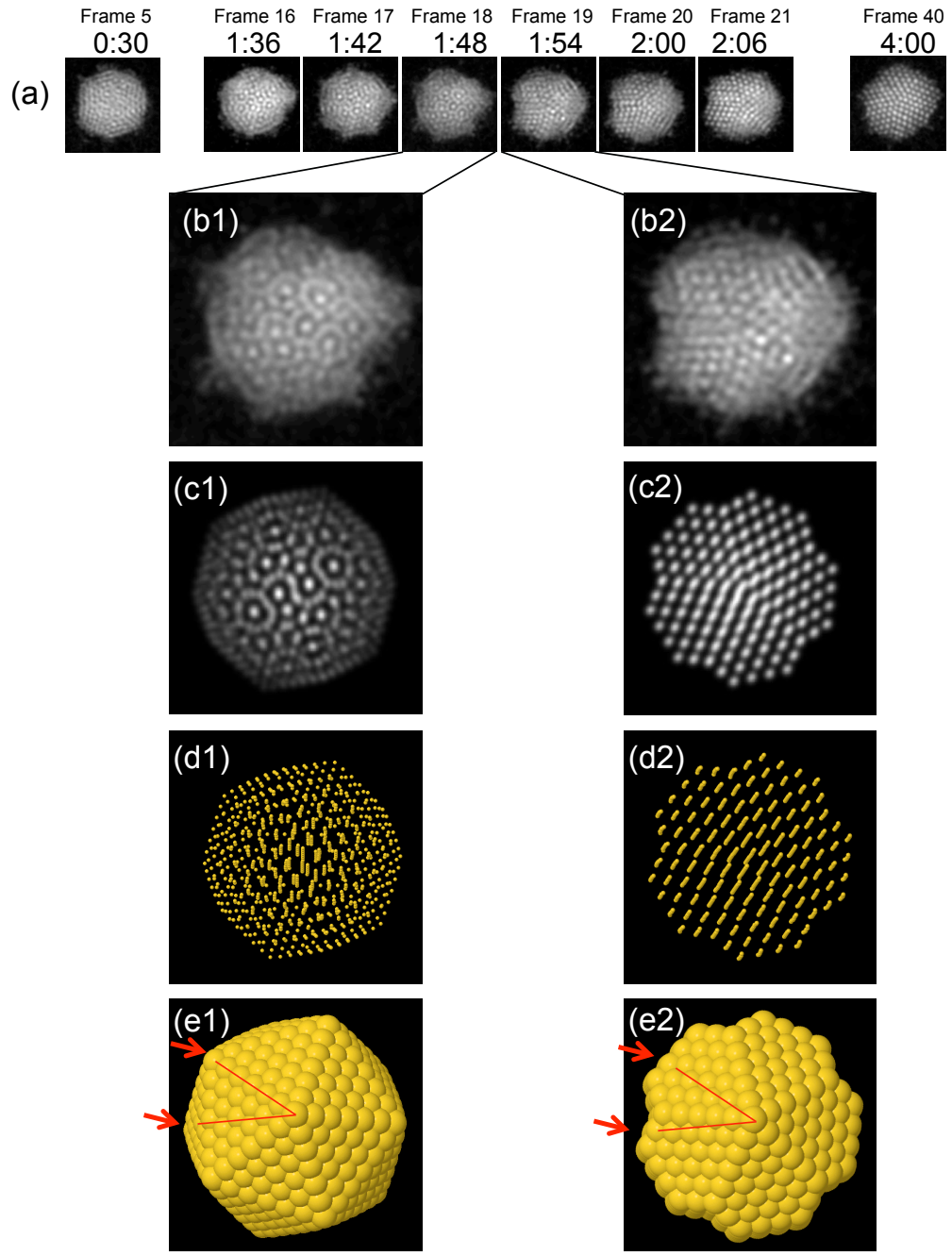

Figure 8.4: (a) The successive (except the first and the last one frame) frames of the structural transformation from Ih to Dh. The upper row indicates the frame numbers while the lower row indicates the time (MM:SS). (b1-2) The magnified experimental images of frame18 and 19 respectively. (c1-2) kinematic simulation of the cluster. (d1-3) the hard ball model with 15% van der Waals radius and (e1-3) the hard ball model with 100% van der Waals radius.

are put into a common axis to show the relative rotation. The boundary are colored to show the shape change. It can be seen that the plane OBC rotates 18° anti-clockwise and the plane AOD rotates 18° clockwise (in fact, it also could be that OBC rotates 18° clockwise and the plane AOD rotates 18° anti-clockwise). This makes the newly formed twin planes located between them. Each of {111} plane labelled with blue and purple slips with a Burger vector $\mathbf{b} = a/6 < 211 >$. The number of atoms in both of the two units are unchanged before and after the structural transformation, which is 91. The number of atoms on each surface is also unchanged (21 for ABO, ODC, AOD and BOC, 36 for ABCD). It shows that there is no need for atomic diffusion during this process. An important feature of this structural transformation mechanism is that the complete shell Ih to Ino Dh. However, as shown in Figure 8.4 (b3), the transformed structure is a Marks-Dh with truncated angles. It implies that the {111} facets of the initial Ih were not complete shells, but island-like, i.e. the side lines such as AB in Figure 8.5 are not occupied with atoms (so called "Chui icosahedron").

What triggers the structural transformation? Koga et al. shows that it can be due to heating [6]. However, it is not the case here. This is supported by a phenomenon that the frames before and after the structural transformation, the experimental images show complete cluster images (Figure 8.4 (b1-b2) and Figure 8.6 (a-d) for example), which means that the cluster does not transform during electron beam scanning. As estimated above, the temperature of the substrate is very low (room temperature), the electron beam induced heating can only be limited to the cluster which is due to small thermal conduction area. So, if it is due to heating, which only happens when the electron beam

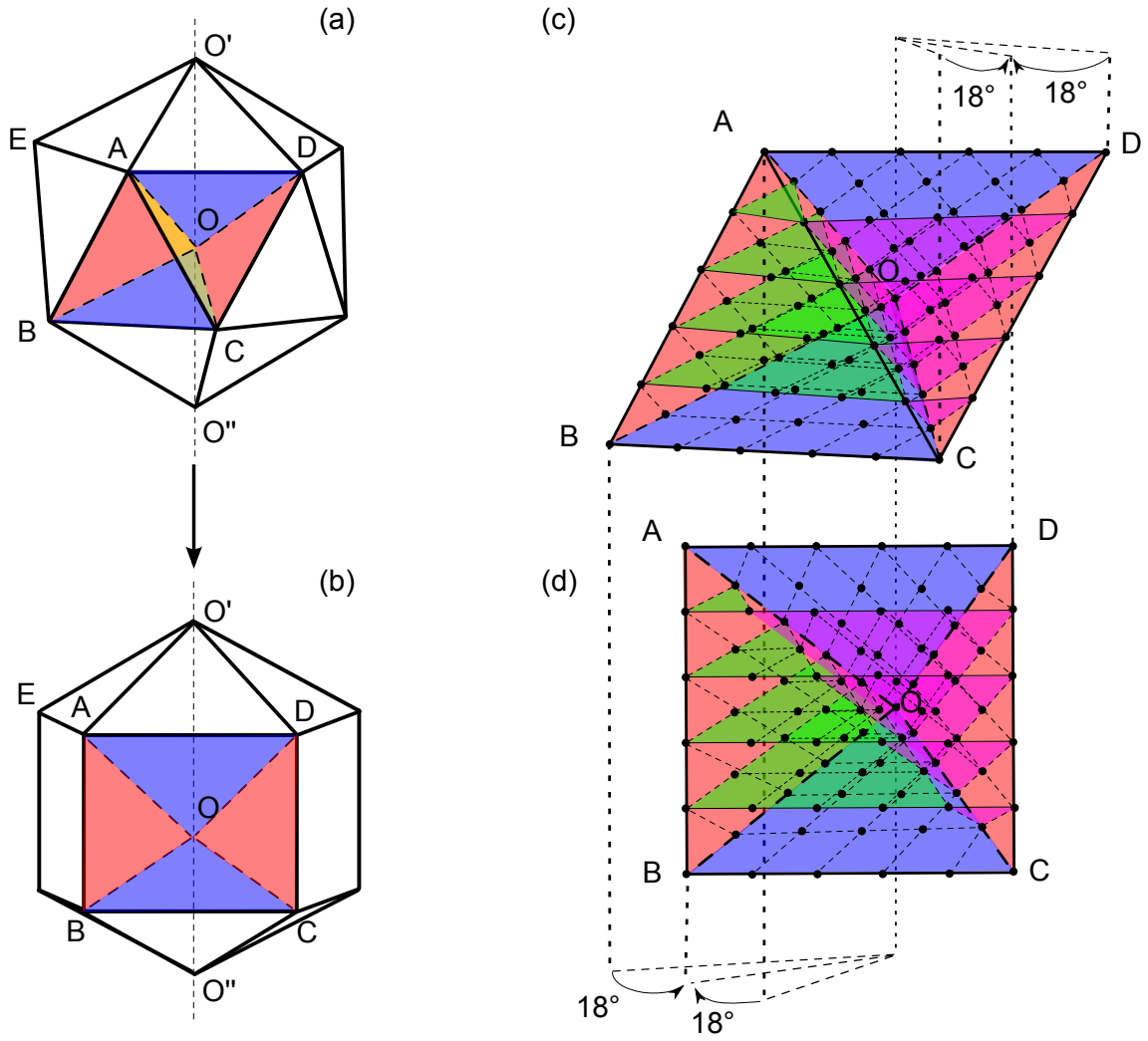

Figure 8.5: Schematics of the Ih-Dh structural transformation. (a) the initial Ih (b) the transformed Dh. The middle subunits before (c) and after (d) the structural transformation.

hits the cluster, the structural transformation should occur during scanning and the image (during transformation) should show top half Ih and bottom half Dh.

Here, another mechanism is proposed, which is based on the vertical "pushing force", originated from vertical momentum transfer. The Ih is strongly strained and each tetrahedral subunit tends to expand outwards to release the strain. However, the electron beam "pushing force" makes the situation worse and squashes the cluster. The transferred

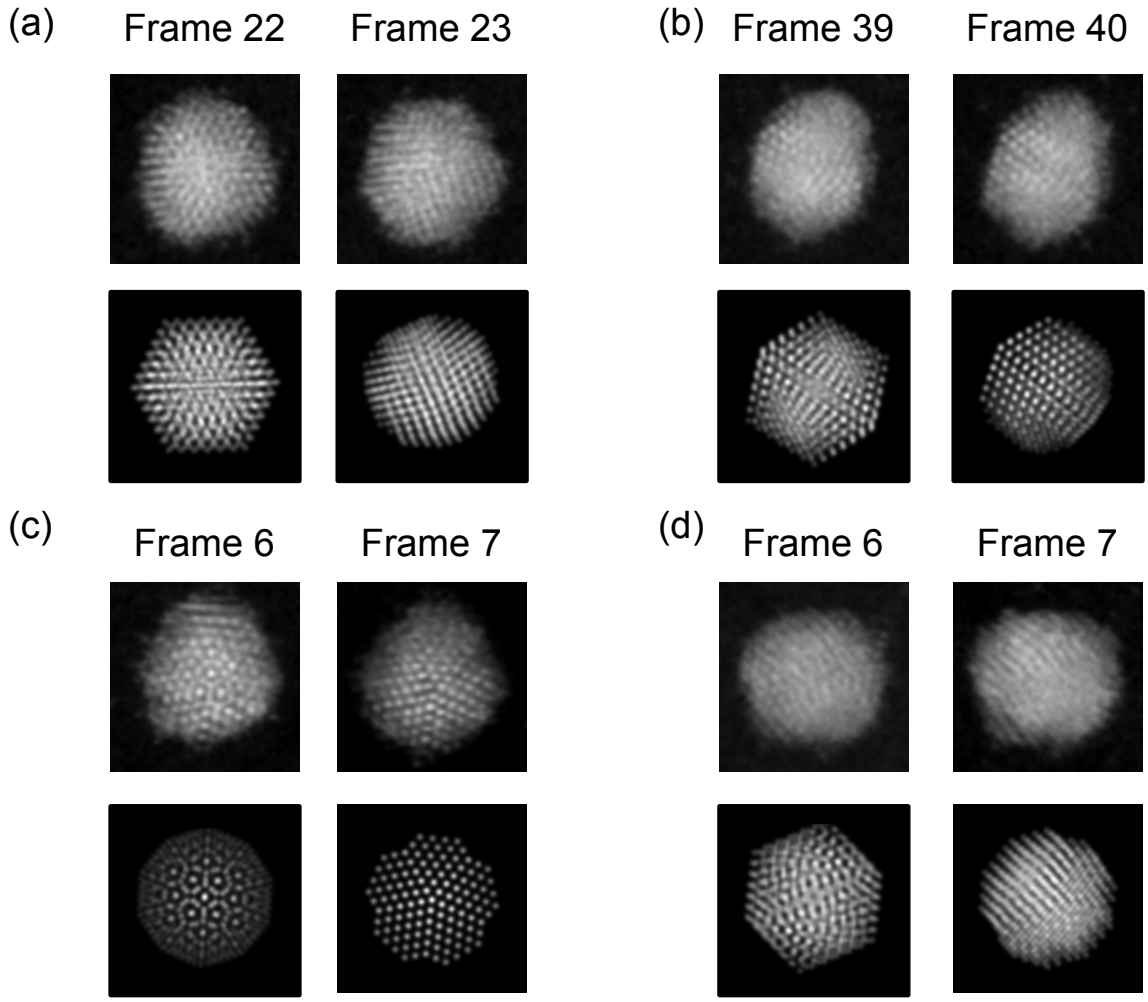

Figure 8.6: Example of successive frames of Ih to Dh transformation. The left columns are experimental images and the right columes are simulated images.

energy is stored as inter-atom potential energy in the cluster. After the electron beam moves away, the cluster starts to expand outwards, and then it induces the twisting of the subunits. The transformation time is estimated between 10 ms to 4 s, which are the time taken for the probe to scan one line and scan from the bottom of the cluster to the top of the cluster (in the next frame) respectively. This is consistent with the structural fluctuation reported by Iijima and Ichihashi, which has the rate of few tens of a second. Here, the direction of the electron beam relative to the cluster is so important that it is possible

for cluster to wait such a long time (comparing with the actual transformation time which is less than 6 s) to rotate to an appropriate orientation. This direction-dependence does not contradict the experimental observation that the transformation has been observed to happen at near all of the $< 111 >$, $< 110 >$ and $< 211 >$ directions (Figure 8.6), because the Ih is such a highly symmetric structure that some of the positions and directions are identical.

8.3.2 Dh to FCC structural transformation

Another important structural transformation, Dh-FCC, where the energy barrier is thought to be "insurmountable" [6], has been observed experimentally. Figure 8.7 shows an example of the structural transformation from Dh to FCC. Before the structural transformation, it can been seen that the cluster maintains the Dh structure with its side sitting on the carbon substrate for 56 frames (5 min 36 s) (Figure 8.7 (a-d)), implying that the cluster does not rotate significantly. The structural transformation for Dh to FCC took 12 frames. From the fringes only it is very hard to work out what the intermediate structures are, however, in general they have shape angles and crystalline fringes (Figure 8.7 (e-p)) showing that it still maintains the solid structure. After the transformation the cluster maintains a hexagonal shape (Figure 8.7 (m-s)) for a long time (16 frames, 1 min 36 s), which shows the FCC structure is stable.

As the Dh to FCC structural transformation can not be achieved by heating, which usually promote the atomic diffusion, it probably involves the subunit slip in the structure shown in Figure 8.8. Figure 8.8 (a) is an example of a Marks-Dh with a subunit missing

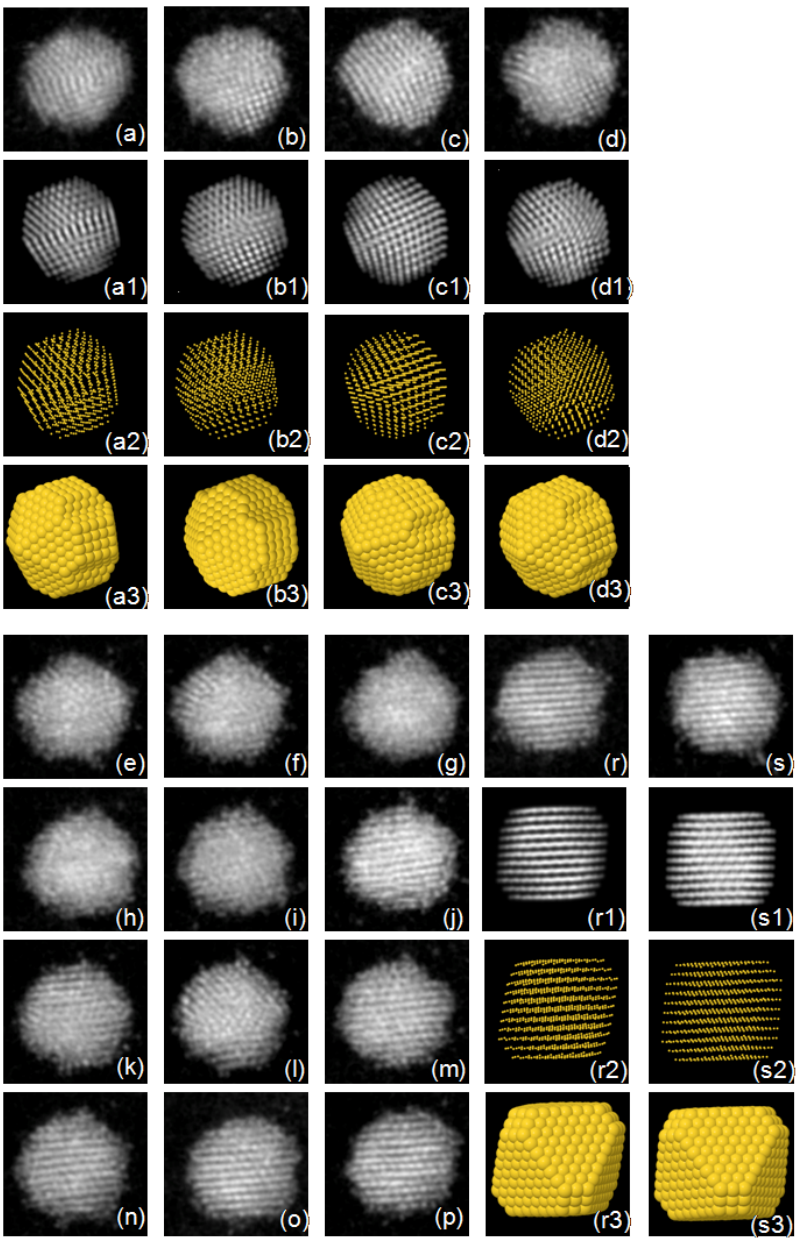

Figure 8.7: The structural transformation from Dh to FCC. (a-d) Frame 2,25,32,56 corresponding the elasped time 0:12, 2:30, 3:12, 5:36 respectively. (a1-d1), (a1-d2) and (a1-d3) are the kinematic simulations, hard ball model with 15% van der Waals radius and hard ball model with 100% van der Waals radius for these orientation. (e-p) Successive images (frame 57-68) of cluster during structural transformation. (r-s) Frame 69 and 80 corresponding the elapsed time 6:54 and 8:00 respectively. (r1-s1), (r1-s2), and (r3-s3) are the kinematic simulations, hard ball model with 15% Van der Waals radius and hard ball model with 100% Van der Waals radius for these orientation.

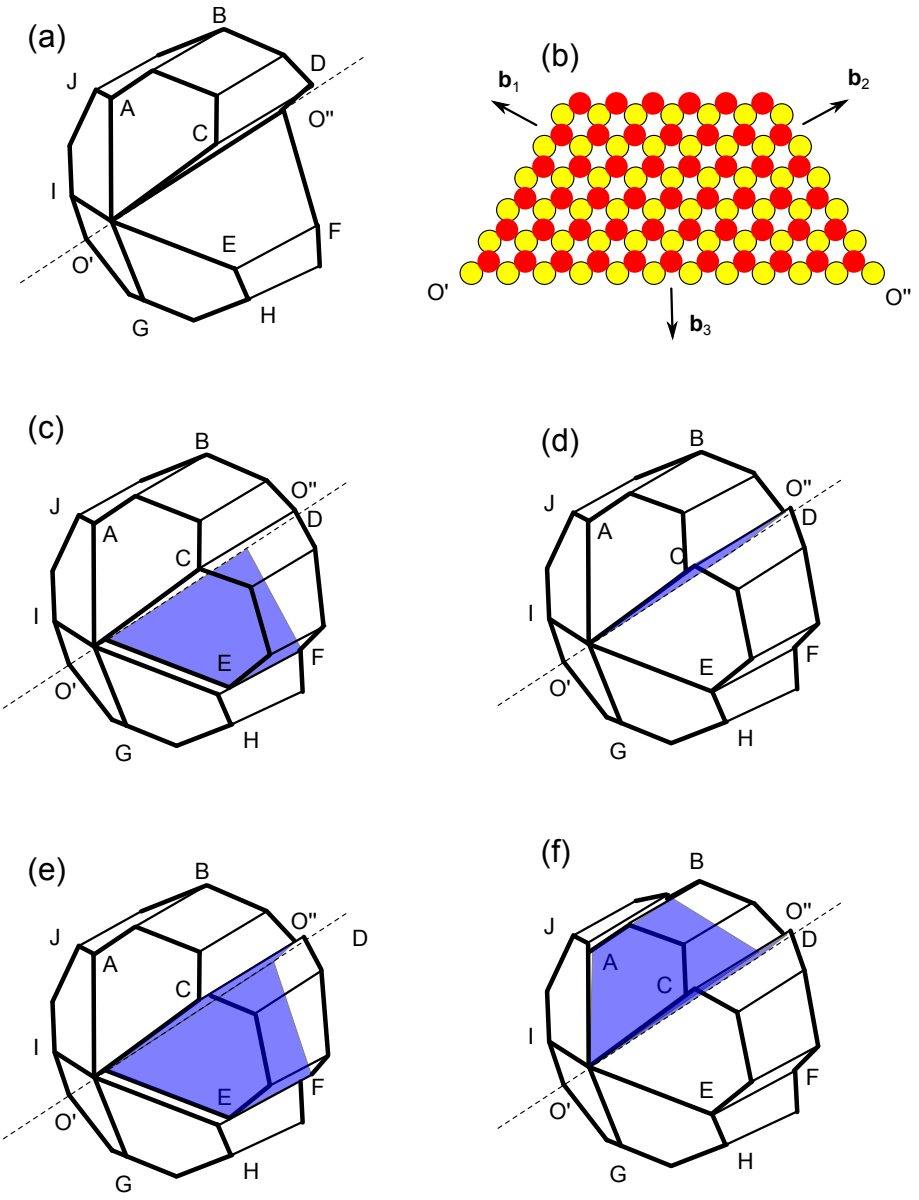

Figure 8.8: (a) A model of a Mark-Dh. (b) The cross section of the twin plane. (c-d) The sliding of a twin plane (e-f) The sliding of two planes of a subunit. The sliding plane is blue.

to show the internal structure. In Figure 8.8 (b) the yellow balls represent one of its twin plane and the red balls are atoms on top of the twin plane of either subunit (as they occupy the same staking position). There are three directions that the red ball (in fact, the whole subunit) can slide, $\mathbf{b}_1$, $\mathbf{b}_2$ and $\mathbf{b}_3$. Figure 8.8 (c) shows a plane (O'O"FE) glide

backwards with $\mathbf{b}_2$. It is also possible to glide forwards with $\mathbf{b}_1$. Another type of the gliding is illustrated in Figure 8.8 (d), where the plane O'O"DC slides downwards with $\mathbf{b}_3$. All of the slip mechanisms mentioned above result in the disappearance of a twin plane. If two sides of a subunit move at the same time, it can eliminate two twin planes at the same time, for example in Figure 8.8 (e) and (f).

The structural transformation is speculated to involve a combination of these steps (Figure 8.7 (c-f)), which is induced by the electron beam momentum transfer. The gliding does not have to happen at the same time. This is probably why that Dh to FCC transformation usually takes longer than the Ih to Dh transformation. From the potential energy surface point of view, the cluster is trapped in the local minima during the transformation (such as Figure 8.7 (i)). Because of the gliding, some new edges are created, on which the atoms are not stable (for example, atoms on edge O'H in Figure 8.8 (c)). Thus, during/after the sliding, some atoms diffuse on the surface to rearrange them to find a stable position, which can explain the image is blurred but still shows shape angles (for example, Figure 8.6 (h) (i)).

An important difference between the electron beam momentum transfer and the heating is that the electron beam momentum transfer is direction dependent and the heating is an isotropy effect. Because the gliding of the subunit (during Dh-FCC structural transformation) can only happen at certain directions (the "pathways" on the potential energy surface), the heating does not help too much. This is believed to be the reason that Dh-FCC structural transformation has not been observed in the heating experiment. In addition, a feature of this proposed mechanism is that at some directions, for example,

the five fold orientation (< 110 >), the "pushing force" is less efficient. In this experiment, the Dh-FCC structural transformation has not been observed at this direction experimentally. This direction-dependence is less important for small clusters, because the activation energy barrier decreases a function of size [206].

8.3.3 Ih to FCC structural transformation

Another type of the structural transformation, Ih-FCC, in fact is a combination of the Ih-Dh and Dh-FCC transformation. Experimentally all (8 out of 8) of the Ih-FCC structural transformation is found to have to go through Dh and neither FCC-Dh or Dh-Ih structural transformation has been found. Thus it shows a sequence Ih-Dh-FCC. Figure 8.9 shows an example, where (a1), (b1-c1) and (d1) are Ih, Dh from two directions and FCC, respectively. This demonstrates that the cluster can hop on the potential energy surface from one structure to another.

Why the structural transformation has certain sequence? For Ih-Dh transformation, an obvious reason is that there is some energy difference between these two structures ($\sim$ 7 eV, estimated using the parameters from [65]), so that the when the cluster wants to transform from Dh to Ih, it needs to overcome higher energy barrier than Ih to Dh. However, it becomes less eloquent for the Dh-FCC transformation as the energy difference between these two structures is very small ($\sim$ 1 eV, estimated using the parameters from [65]) comparing to the thermal energy ($\sim$ 70 eV). In principle, if the Dh can transform to FCC, the FCC should be able to transform to Dh by overcoming similar energy barrier just as the inversed process of Dh to FCC transformation. The possible explanation is

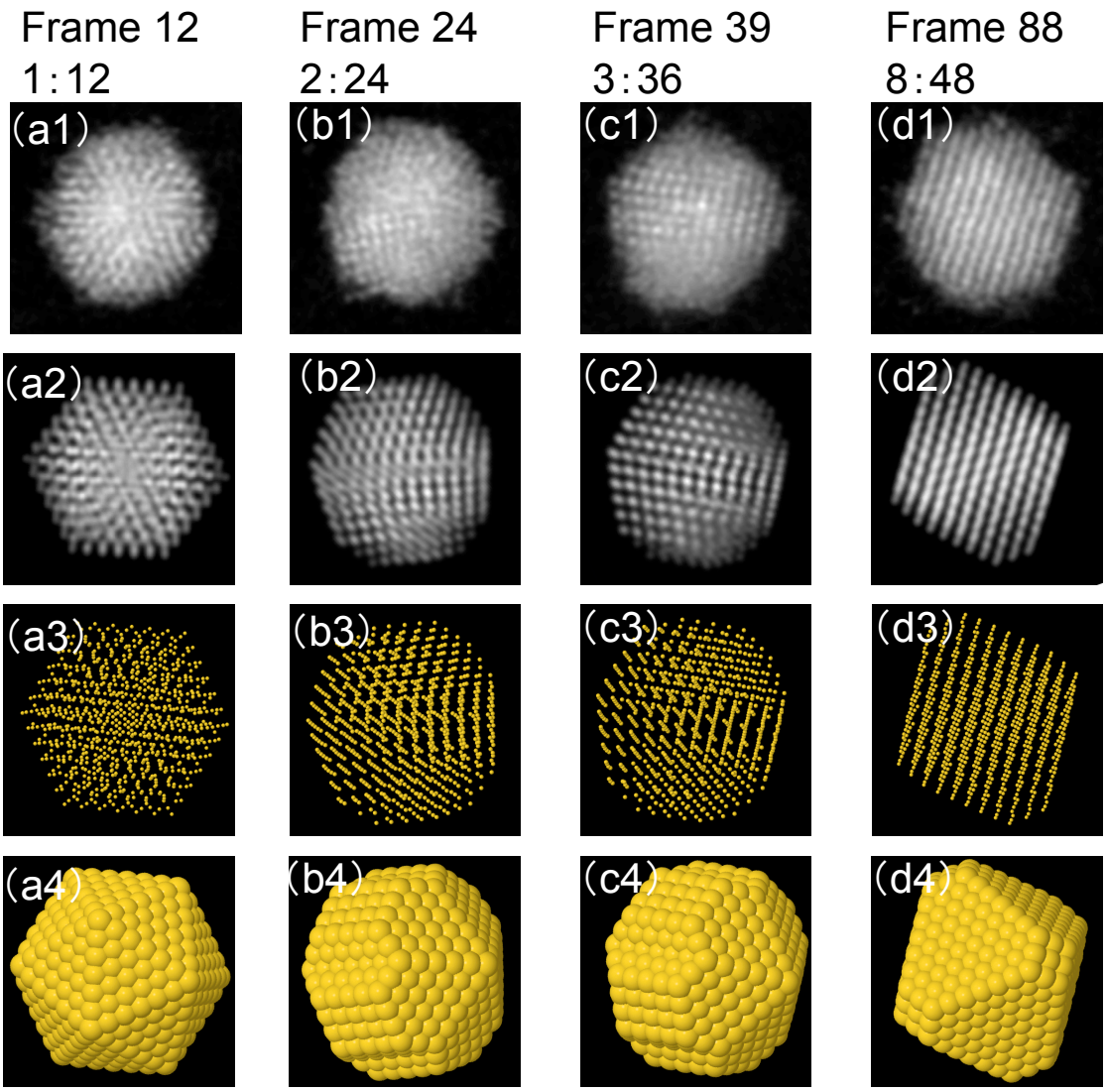

Figure 8.9: (a-d1), (a-d2), (a-d3) and (a-d4) correspond the experimental image, kinematic simulation, hard ball with 15% van der Waals radius and hard ball with 100 % van der Waals radius. The top row indicates the frame NO. and the elapsed time (MM:SS).

that at this size, the five fold twin is not that easy to create. From the potential energy surface point of view, the "pathways" of FCC-Dh transformation is too narrow so that the transformation probability is very low but sometimes it can happen [147].

8.4 Summary

To summarize, in this chapter, it has been experimentally observed the structural transformations induced by electron beam irradiation. The structural transformation follows a sequence, which is Ih-Dh-FCC. The mechanism of Ih to Dh structural transformation proposed by Koga has been observed directly and the Dh to FCC transformation mechanism has been proposed. The energy difference between structures are not very high, which cannot fully explain the "sequence". This probably involves the transformation probability of the structural trap on the potential energy surface, showing that the n-dimensional energy surface is more complicated than only considering the energy difference and the energy barrier.

Chapter 9

Conclusions

This thesis has achieved two goals: (1) developing a single-shot imaging method for identifying structure in small nanoclusters; (2) applying it to the study of formation mechanism and stability of Au_{887} structures.

In developing the methodology, this work has involved the experimental quantification of the microscope and mathematical modelling of high angle annular dark field-scanning transmission electron microscopy (HAADF-STEM) images. In the experimental quantification of the microscope, this work has focussed on the ADF detector. Detector response has been investigated as a function of the beam current, taking into account of the brightness and contrast setting of the pre-amplifier. For each region of the detector, the response was found to be linear as a function of the electron dose. However, the efficiency mapping was not uniform across the detector. The mathematical modelling part of the work has shown that for cluster at small size, the signal collected by the detector is dominated by the kinematic scattering. The intensity contributed by kinematic scattering is

approximately linear as a function of the number of atoms within atomic columns and within whole clusters, implying that the intensity contribution of each atom is equal in monometallic clusters, i.e., kinematic scattering assumption.

The kinematic scattering assumption simplifies the mathematical description of the HAADF-STEM images, which enables image simulation with fast computational speed. It brings the convinience for studying the ultrasmall nanoclusters. The intrinsic instability of the ultrasmall cluster prevents the systematic tilting of the sample, but systematic tilting of image simulations allows atomic structure identification of nanoclusters from one experimental image. This is the single-shot imaging method of structural identification.

This single-shot method is extremely useful in studying statistically significant cluster structure distribution, which requires large amount data to identify trends. In this thesis this method was applied to studying the cluster structure distribution as a function of experimental conditions for Au cluster formed in gas phase and filtered by a time-of-flight mass selector. These clusters contain a nominal size of 887 atoms. The result shows that the cluster prefers to form icosahedron (Ih) in fast condensation experimental conditions, i.e. shorter condensation length, higher sputtering power, higher He and Ar flow, but prefers to form face centred cubic (FCC) structure in slow condensation experiment conditions. This indicates that the Ih is a non-equilibrium structure.

Furthermore, the stability of the structures has been investigated in this study by using electron beam irradiation. These results show that within 10 minutes irradiation the cluster can transform from one structure to another. The structural transformation sequence found was Ih to decahedron (Dh) to FCC. During the two types of structure

transformation, i.e. Ih to Dh and Dh to FCC, the clusters show sharp angles, implying that the structural transformation is via solid-solid transformation.

The work done in this thesis not only gives insights useful to manufacturing clusters with different internal crystallographic structure, but also, more importantly, demonstrates that the single-shot imaging method with help of fast kinematic simulation, is very effective in studying the atomic structure of clusters. This method providing a quick way of structural identification and paves the way to study structure distribution requiring statistically significant data sets.

For the future work, there are two directions suggested in this study. The first one is to apply this method to more complicated and dynamic systems, such as the bimetallic systems or to investigate temperature dependent behaviour of nanoclusters. The greater number of free parameters in these systems such as composition ratio and orientation require a large number of simulations to form conclusions. The kinematic simulation developed in this work gives a comparison of experimental image and simulation from which some parameters, such as orientation can be identified and then used as the initial parameter for multi-slice simulations. Incorporating the efficiency map of the detector, which was also obtained in this thesis, into the multi-slice simulation, would enable the comparison of the absolute intensity of the simulation and the HAADF-STEM images, and thus potentially reveal the three dimensional information within the cluster quantitatively.

The second line of future work suggested by this thesis is in producing clusters with desired structure and size. The key to this is to improve the fraction of Ih clusters, which is a metastable structure and can be easily transformed into other structures. This

needs the modification of the cluster source such as increasing the sputtering power and the inert gas flows. The geometry of nanoclusters, such as the number of the corner and edge atoms, the coordinations of these atoms, and the numbers of {111} facets and {100} facets, as well as the internal strains can potentially affect their catalytic behaviour. Thus it would be extremely interesting to explore the correlation between the catalytic reactivity performance and the proportions of the structures, i.e. structure-dependence.

List of papers

[1] **D.S. He** and Z.Y. Li, A practical approach to quantify the ADF detector in STEM, *Jounal of Physics*: *Conference Series*, EMAG, 2013.

[2] Y. Han, **D.S. He**, and Z.Y. Li, Direct observation of dynamic events of Au clusters on MgO(100) by HAADF-STEM, *Journal of Nanoparticle Research*, 15,1941, (2013).

[3] J. Fennell, **D. He**, A. M. Tanyi, A.J. Logsdail, R.L. Johnston, Z.Y. Li, and S.L. Horswell, A selective blocking method to control the overgrowth of Pt on Au nanorods, *Journal of the American Chemical Society*, 135, 6554, (2013).

[4] **D. S. He**, Y. Han, J. Fennell, S. L. Horswell and Z. Y. Li, Growth and stability of Pt on Au nanorods, *Applied Physics Letters*, 101, 113102, (2012).

[5] Y. Han, **D.S. He**, Y. Liu, S. Xie, T. Tsukuda and Z.Y. Li, Size and shape of nanoclusters: single-shot imaging approach, *Small*, 8, No. 15, 2361 , (2012)

References

[1] R. Meyer, C. Lemire, S. K. Shaikhutdinov, and H. J. Freund. Surface chemistry of catalysis by gold. *Gold Bulletin*, 37(1):72–124, 2004. 1

[2] J. Gong. Structure and surface chemistry of gold-based model catalysts. *Chemical Reviews*, 112(5):2987–3054, 2012. 1

[3] Y. D. Kim, M. Fischer, and G. Ganteför. Origin of unusual catalytic activities of Au-based catalysts. *Chemical Physics Letters*, 377(1):170–176, 2003. 1

[4] B. Hvolbæk, T. V. W. Janssens, B. S. Clausen, H. Falsig, C. H Christensen, and J. K. Nørskov. Catalytic activity of Au nanoparticles. *Nano Today*, 2(4):14–18, 2007. 1

[5] H. Hofmeister. Fivefold twinned nanoparticles. *Encyclopedia of Nanoscience and Nanotechnology*, 3:431, 2004. 1

[6] K. Koga, T. Ikeshoji, and K. Sugawara. Size-and temperature-dependent structural transitions in gold nanoparticles. *Physical Review Letters*, 92(11):115507, 2004. 1, 16, 26, 27, 28, 127, 135, 137, 140

[7] S. Iijima and T. Ichihashi. Structural instability of ultrafine particles of metals. *Physical Review Letters*, 56(6):616–619, 1986. 1, 24, 25, 133

[8] Z. Y. Li, J. P. Wilcoxon, F. Yin, Y. Chen, R. E. Palmer, and R. L. Johnston. Structures and optical properties of 4–5 nm bimetallic AgAu nanoparticles. *Faraday Discussions*, 138:363–373, 2008. 1

[9] Z. Y. Li, N. P. Young, M. Di Vece, R. E. Palomba, S .and Palmer, A. L. Bleloch, B. C. Curley, R. L. Johnston, J. Jiang, and J. Yuan. Three-dimensional atomic-scale structure of size-selected gold nanoclusters. *Nature*, 451(7174):46–48, 2007. 2, 24, 72, 76, 90

[10] B. C. Curley, R. L. Johnston, N. P. Young, Z. Y. Li, M. Di Vece, R. E. Palmer, and A. L. Bleloch. Combining theory and experiment to characterise the atomic structures of surface-deposited Au_{309} clusters. *The Journal of Physical Chemistry C*, 111(48):17846–17851, 2007. 2, 91, 94

[11] I. M. Goldby. *Dynamics of molecules and clusters at surfaces*. University of Cambridge, 1996. 5, 6, 7, 8, 9

[12] W. A. De Heer. The physics of simple metal clusters: experimental aspects and simple models. *Reviews of Modern Physics*, 65(3):611, 1993. 5, 6, 7

[13] K. Wegner, P. Piseri, H. V. Tafreshi, and P. Milani. Cluster beam deposition: a tool for nanoscale science and technology. *Journal of Physics D: Applied Physics*, 39(22):R439, 2006. 5, 8, 9

[14] R. Uyeda. Studies of ultrafine particles in japan: Crystallography, methods of preparation and technological applications. *Progress in Materials Science*, 35(1): 1–96, 1991. 5, 9

[15] O. F. Hagena. Nucleation and growth of clusters in expanding nozzle flows. *Surface Science*, 106(1):101–116, 1981. 5

[16] W. Knauer. Formation of large metal clusters by surface nucleation. *Journal of Applied Physics*, 62(3):841–851, 1987. 5

[17] S. H. Baker, S. C. Thornton, K. W. Edmonds, M. J. Maher, C. Norris, and C. Binns. The construction of a gas aggregation source for the preparation of size-selected nanoscale transition metal clusters. *Review of Scientific Instruments*, 71(8):3178–3183, 2000. 5

[18] M. Arnold, J. Kowalski, G. Zu Ptlitz, T. Stehlin, and F. Träger. Methods for generating neutral, mass-selected cluster beams. *Surface Science*, 156:149–156, 1985. 5

[19] S. J. Riley, E. K. Parks, C. R. Mao, L. G. Pobo, and S. Wexler. Generation of continuous beams of refractory metal clusters. *The Journal of Physical Chemistry*, 86(20):3911–3913, 1982. 5

[20] R. E. Smalley. Laser studies of metal cluster beams. *Laser Chemstry*, 1983. 5

[21] T.G. Dietz, M.A. Duncan, D.E. Powers, and R.E. Smalley. Laser production of supersonic metal cluster beams. *The Journal of Chemical Physics*, 74(11):6511–6512, 1981. 5

[22] P. Milani and W.A. Deheer. Improved pulsed laser vaporization source for production of intense beams of neutral and ionized clusters. *Review of Scientific Instruments*, 61(7):1835–1838, 1990. 5

[23] P. Milani and W. A. de Heer. Relative thermometer for neutral clusters produced in laser-vaporization sources. *Physical Review B*, 44:8346–8348, 1991. 5

[24] E. C. Honea, M. L. Homer, J. L. Persson, and R. L. Whetten. Generation and photoionization of cold Na_n clusters;n to 200. *Chemical Physics Letters*, 171(3): 147–154, 1990. 5

[25] H. R. Siekmann, C. Lüder, J. Faehrmann, H. O. Lutz, and K. H. Meiwes-Broer. The pulsed arc cluster ion source (PACIS). *Zeitschrift für Physik D Atoms, Molecules and Clusters*, 20(1):417–420, 1991. 5, 7

[26] G. Ganteför, H. R. Siekmann, H. O. Lutz, and K. H. Meiwes-Broer. Pure metal and metal-doped rare-gas clusters grown in a pulsed arc cluster ion source. *Chemical Physics Letters*, 165(4):293–296, 1990. 5

[27] S. Pratontep, S. J. Carroll, C. Xirouchaki, M. Streun, and R. E. Palmer. Size-selected cluster beam source based on radio frequency magnetron plasma sputtering and gas condensation. *Review of Scientific Instruments*, 76(4):045103–045103, 2005. 5, 116, 117

[28] S. G. Hall, M. B. Nielsen, A. W. Robinson, and R. E. Palmer. Compact sputter source for deposition of small size-selected clusters. *Review of Scientific Instruments*, 68(9):3335–3339, 1997. 5

[29] L. S. Wang, R. T. Wen, Y. Chen, G. H. Yue, D. L. Peng, and T. Hihara. Gas-phase preparation and size control of Fe nanoparticles. *Applied Physics A: Materials Science & Processing*, 103(4):1015–1020, 2011. 5

[30] T. Hihara and K. Sumiyama. Formation and size control of a Ni cluster by plasma gas condensation. *Journal of Applied Physics*, 84(9):5270–5276, 1998. 5, 9

[31] A. I. Ayesh, S. Thaker, N. Qamhieh, and H. Ghamlouche. Size-controlled Pd nanocluster grown by plasma gas-condensation method. *Journal of Nanoparticle Research*, 13(3):1125–1131, 2011. 5

[32] S. B. DiCenzo, S. D. Berry, and E. H. Hartford Jr. Photoelectron spectroscopy of single-size Au clusters collected on a substrate. *Physical Review B*, 38:8465–8468, 1988. 5, 8

[33] S. J. Carroll, S. Pratontep, M. Streun, R. E. Palmer, S. Hobday, and R. Smith. Pinning of size-selected Ag clusters on graphite surfaces. *The Journal of Chemical Physics*, 113(18):7723, 2000. 5

[34] S. Pratontep. *Production and Characterisation of Size-Selected Nanoclusters on Surfaces*. PhD thesis, University of Birmingham, 2003. 7, 9

[35] V. N. Popok, I. Barke, E. E. B. Campbell, and K. H. Meiwes-Broer. Cluster–surface interaction: From soft landing to implantation. *Surface Science Reports*, 66 (10):347–377, 2011. 7

[36] C. Xirouchaki and R. E. Palmer. Deposition of size-selected metal clusters generated by magnetron sputtering and gas condensation: a progress review. *Philosophical Transactions of the Royal Society of London. Series A: Mathematical, Physical and Engineering Sciences*, 362(1814):117–124, 2004. 7

[37] H. Haberland, M. Karrais, M. Mall, and Y. Thurner. Thin films from energetic cluster impact: A feasibility study. *Journal of Vacuum Science & Technology A: Vacuum, Surfaces, and Films*, 10(5):3266–3271, 1992. 7

[38] G. I. Taylor and A. D. McEwan. The stability of a horizontal fluid interface in a vertical electric field. *Journal of Fluid Mechanics*, 22(1):1–15, 1965. 7

[39] K. E. J. Lehtinen and M. R. Zachariah. Self-preserving theory for the volume distribution of particles undergoing brownian coagulation. *Journal of colloid and interface science*, 242(2):314–318, 2001. 9

[40] N. P. Young, Z. Y. Li, Y. Chen, S. Palomba, M. Di Vece, and R. E. Palmer. Weighing supported nanoparticles: size-selected clusters as mass standards in nanometrology. *Physical Review Letters*, 101(24):246103, 2008. 10

[41] D. Pearmain. *Electron microscopy characterisation of size-selected Pd clusters and industrial Pd catalysts*. PhD thesis, University of Birmingham, 2011. 10, 12, 117

[42] A. R. Tao, S. Habas, and P. Yang. Shape control of colloidal metal nanocrystals. *Small*, 4(3):310–325, 2008. 11

[43] U. S. Mohanty. Electrodeposition: a versatile and inexpensive tool for the synthesis of nanoparticles, nanorods, nanowires, and nanoclusters of metals. *Journal of Applied Electrochemistry*, 41(3):257–270, 2011. 11

[44] C. Lofton and W. Sigmund. Mechanisms controlling crystal habits of gold and silver colloids. *Advanced Functional Materials*, 15(7):1197–1208, 2005. 11

[45] W. Niu and G. Xu. Crystallographic control of noble metal nanocrystals. *Nano Today*, 6(3):265–285, 2011. 11

[46] P. Moriarty. Nanostructured materials. *Reports on Progress in Physics*, 64(3):297, 2001. 11

[47] M. Faraday. The bakerian lecture: experimental relations of gold (and other metals) to light. *Philosophical Transactions of the Royal Society of London*, 147:145–181, 1857. 11

[48] Y. Xia, Y. Xiong, B. Lim, and S. E. Skrabalak. Shape-controlled synthesis of metal nanocrystals: Simple chemistry meets complex physics? *Angewandte Chemie International Edition*, 48(1):60–103, 2009. 11

[49] J. Fennell, D. He, A. M. Tanyi, A. J. Logsdail, R. L. Johnston, Z. Y. Li, and S. L. Horswell. A selective blocking method to control the overgrowth of Pt on Au nanorods. *Journal of the American Chemical Society*, 2013. 11

[50] G. M. Whitesides, J. P. Mathias, and C. T. Seto. Molecular self-assembly and nanochemistry: a chemical strategy for the synthesis of nanostructures. Technical report, DTIC Document, 1991. 12

[51] G. M. Whitesides and M. Boncheva. Beyond molecules: Self-assembly of mesoscopic and macroscopic components. *Proceedings of the National Academy of Sciences*, 99 (8):4769–4774, 2002. 12

[52] Q. Zhang, J. Xie, J. Yang, and J. Y. Lee. Monodisperse icosahedral Ag, Au, and Pd nanoparticles: size control strategy and superlattice formation. *ACS Nano*, 3 (1):139–148, 2008. 12

[53] S. Mann. Self-assembly and transformation of hybrid nano-objects and nanostructures under equilibrium and non-equilibrium conditions. *Nature Materials*, 8(10): 781–792, 2009. 12

[54] J. V. Barth, G. Costantini, and K. Kern. Engineering atomic and molecular nanostructures at surfaces. *Nature*, 437(7059):671–679, 2005. 12, 13

[55] A. Kühnle. Self-assembly of organic molecules at metal surfaces. *Current Opinion in Colloid & Interface Science*, 14(2):157–168, 2009. 12

[56] H. Hofmeister. Fivefold twinned nanoparticles'. *Encyclopedia of Nanoscience and Nanotechnology*, 10:1–22, 2003. 13, 14, 25

[57] H. Hofmeister. Shape variations and anisotropic growth of multiply twinned nanoparticles. *Zeitschrift für Kristallographie*, 224(11):528–538, 2009. 14

[58] M. J. Walsh, K. Yoshida, A. Kuwabara, M. L. Pay, P. L. Gai, and E. D. Boyes. On the structural origin of the catalytic properties of inherently strained ultrasmall decahedral gold nanoparticles. *Nano Letters*, 12(4):2027–2031, 2012. 14, 115

[59] C. Mohr, H. Hofmeister, and P. Claus. The influence of real structure of gold catalysts in the partial hydrogenation of acrolein. *Journal of Catalysis*, 213(1): 86–94, 2003. 14, 24

[60] K. Koga. Novel bidecahedral morphology in gold nanoparticles frozen from liquid. *Physical review letters*, 96(11):115501, 2006. 14

[61] G. Rossi and R. Ferrando. Freezing of gold nanoclusters into poly-decahedral structures. *Nanotechnology*, 18(22):225706, 2007. 14

[62] A. L. Mackay. A dense non-crystallographic packing of equal spheres. *Acta Crystallographica*, 15(9):916–918, 1962. 15

[63] K. H. Kuo. Mackay, anti-mackay, double-mackay, pseudo-mackay, and related icosahedral shell clusters. *Structural Chemistry*, 13(3):221–230, 2002. 15

[64] T. P. Martin. Shells of atoms. *Physics Reports*, 273(4):199–241, 1996. 15

[65] F. Baletto, R. Ferrando, A. Fortunelli, F. Montalenti, and C. Mottet. Crossover among structural motifs in transition and noble-metal clusters. *The Journal of Chemical Physics*, 116:3856, 2002. 15, 20, 23, 144

[66] H. S. Nam, N. M. Hwang, B. D. Yu, and J. K. Yoon. Formation of an icosahedral structure during the freezing of gold nanoclusters: Surface-induced mechanism. *Physical Review Letters*, 89(27):275502, 2002. 15, 23

[67] Y. G. Chushak and L. S. Bartell. Melting and freezing of gold nanoclusters. *The Journal of Physical Chemistry B*, 105(47):11605–11614, 2001. 15

[68] C. L. Cleveland, W. D. Luedtke, and U. Landman. Melting of gold clusters: Icosahedral precursors. *Physical Review Letters*, 81(10):2036–2039, 1998. 15

[69] F. Baletto, C. Mottet, and R. Ferrando. Microscopic mechanisms of the growth of metastable silver icosahedra. *Physical Review B*, 63(15):155408, 2001. 15, 22

[70] A. S. Barnard, G. Opletal, I. K. Snook, and S. P. Russo. Ideality versus reality: Emergence of the chui icosahedron. *The Journal of Physical Chemistry C*, 112(38): 14848–14852, 2008. 16

[71] Y. H. Chui, R. J. Rees, I. K. Snook, B. O'Malley, and S. P. Russo. Topological characterization of crystallization of gold nanoclusters. *The Journal of Chemical Physics*, 125:114703, 2006. 16

[72] Y. H. Chui, G. Grochola, I. K. Snook, and S. P. Russo. Molecular dynamics investigation of the structural and thermodynamic properties of gold nanoclusters of different morphologies. *Physical Review B*, 75(3):033404, 2007. 16, 23

[73] C.L. Cleveland and U. Landman. The energetics and structure of nickel clusters: Size dependence. *The Journal of Chemical Physics*, 94:7376, 1991. 16, 23

[74] J. A. Ascencio, C. Gutiérrez-Wing, ME Espinosa, M. Marin, S. Tehuacanero, C. Zorrilla, and M. José-Yacamán. Structure determination of small particles by hrem imaging: theory and experiment. *Surface Science*, 396(1):349–368, 1998. 16

[75] C. L. Cleveland, U. Landman, T. G. Schaaff, M. N. Shafigullin, P. W. Stephens, and R. L. Whetten. Structural evolution of smaller gold nanocrystals: The truncated decahedral motif. *Physical Review Letters*, 79(10):1873–1876, 1997. 17

[76] V. G. Gryaznov, J. Heydenreich, A. M. Kaprelov, S. A. Nepijko, A. E. Romanov, and J. Urban. Pentagonal symmetry and disclinations in small particles. *Crystal Research and Technology*, 34(9):1091–1119, 1999. 17, 26, 27

[77] L. D. Marks. Experimental studies of small particle structures. *Reports on Progress in Physics*, 57(6):603, 1999. 17

[78] F. Baletto and R. Ferrando. Structural properties of nanoclusters: Energetic, thermodynamic, and kinetic effects. *Reviews of Modern Physics*, 77(1):371, 2005. 17, 18, 19, 95

[79] K. M. Ho, A. A. Shvartsburg, B. Pan, Z. Y. Lu, C. Z. Wang, J. G. Wacker, J. L. Fye, and M. F. Jarrold. Structures of medium-sized silicon clusters. *Nature*, 392 (6676):582–585, 1998. 19

[80] C. Barreteau, R. Guirado-López, D. Spanjaard, M. C. Desjonqueres, and A. M. Oleś. spd tight-binding model of magnetism in transition metals: Application to Rh and Pd clusters and slabs. *Physical Review B*, 61(11):7781, 2000. 19

[81] R. Ferrando, J. Jellinek, R. L. Johnston, et al. Nanoalloys: from theory to applications of alloy clusters and nanoparticles. *Chemical reviews*, 108(3):845, 2008. 19

[82] A. N. Patil, D. Y. Paithankar, N. Otsuka, and R. P. Andres. The minimum-energy structure of nanometer-scale gold clusters. *Zeitschrift für Physik D Atoms, Molecules and Clusters*, 26(1):135–137, 1993. 20

[83] C. G. Granqvist and R. A. Buhrman. Ultrafine metal particles. *Journal of Applied Physics*, 47(5):2200–2219, 1976. 20

[84] A. L. Gonzalez, C. Noguez, and A. S. Barnard. Map of the structural and optical properties of gold nanoparticles at thermal equilibrium. *The Journal of Physical Chemistry C*, 116(26):14170–14175, 2012. 20

[85] J. J. Mock, M. Barbic, D. R. Smith, D. A. Schultz, and S. Schultz. Shape effects in plasmon resonance of individual colloidal silver nanoparticles. *The Journal of Chemical Physics*, 116:6755, 2002. 20

[86] R. Narayanan and M. A. El-Sayed. Changing catalytic activity during colloidal platinum nanocatalysis due to shape changes: electron-transfer reaction. *Journal of the American Chemical Society*, 126(23):7194–7195, 2004. 20

[87] R. A. Roy, R. Messier, and J. M. Cowley. Fine structure of gold particles in thin films prepared by metal-insulator co-sputtering. *Thin Solid Films*, 79(3):207–215, 1981. 21

[88] A. Pinto, A. R. Pennisi, G. Faraci, G. D'agostino, S. Mobilio, and F. Boscherini. Evidence for truncated octahedral structures in supported gold clusters. *Physical Review B*, 51(8):5315, 1995. 21

[89] F. Silly and M. R. Castell. Temperature-dependent stability of supported five-fold twinned copper nanocrystals. *ACS Nano*, 3(4):901–906, 2009. 21

[90] G. Grochola, S. P. Russo, and I. K. Snook. On morphologies of gold nanoparticles grown from molecular dynamics simulation. *The Journal of Chemical Physics*, 126: 164707, 2007. 21

[91] C. Feigl, G. Grochola, G. Opletal, I. K. Snook, and S. P. Russo. A theoretical study of size and temperature dependent morphology transformations in gold nanoparticles. *Chemical Physics Letters*, 474(1):115–118, 2009. 21

[92] C. Desgranges and J. Delhommelle. Molecular simulation of the nucleation and growth of gold nanoparticles. *The Journal of Physical Chemistry C*, 113(9):3607–3611, 2009. 21

[93] A. S. Barnard. Direct comparison of kinetic and thermodynamic influences on gold nanomorphology. *Accounts of Chemical Research*, 45(10):1688–1697, 2012. 21

[94] F. Baletto, C. Mottet, and R. Ferrando. Reentrant morphology transition in the growth of free silver nanoclusters. *Physical Review Letters*, 84(24):5544–5547, 2000. 22

[95] G. Grochola, I. Snook, D. Chui, and S. P. Russo. Exploring the effects of different immersion environments on the growth of gold nanostructures. *Molecular Simulation*, 32(15):1255–1260, 2006. 22

[96] A. S. Barnard, N. P. Young, A. I. Kirkland, M. A. van Huis, and H. Xu. Nanogold: a quantitative phase map. *ACS Nano*, 3(6):1431–1436, 2009. 22, 23, 115

[97] S. Ino. Stability of multiply-twinned particles. *Journal of the Physical Society of Japan*, 27(4):941–953, 1969. 22

[98] G. Grochola, I. K. Snook, and S. P. Russo. Influence of substrate morphology on the growth of gold nanoparticles. *The Journal of Chemical Physics*, 129:154708, 2008. 23

[99] C. L. Kuo and P. Clancy. Melting and freezing characteristics and structural properties of supported and unsupported gold nanoclusters. *The Journal of Physical Chemistry B*, 109(28):13743–13754, 2005. 23

[100] Y. Wang, S. Teitel, and C. Dellago. Melting of icosahedral gold nanoclusters from molecular dynamics simulations. *The Journal of Chemical Physics*, 122:214722, 2005. 23

[101] F. Chen, Z. Y. Li, and R. L. Johnston. Surface reconstruction precursor to melting in Au_{309} clusters. *AIP Advances*, 1(3):032105–032105, 2011. 23

[102] J. P. K. Doye and D. J. Wales. Thermally-induced surface reconstructions of mackay icosahedra. *Zeitschrift für Physik D Atoms, Molecules and Clusters*, 40(1):466–468, 1997. 23

[103] F. Ercolessi, W. Andreoni, and E. Tosatti. Melting of small gold particles: Mechanism and size effects. *Physical Review Letters*, 66(7):911–914, 1991. 23

[104] D. Schebarchov and S. C. Hendy. Thermal instability of decahedral structures in platinum nanoparticles. *The European Physical Journal D-Atomic, Molecular, Optical and Plasma Physics*, 43(1):11–14, 2007. 23

[105] D. Schebarchov, S. C. Hendy, and W. Polak. Molecular dynamics study of the melting of a supported 887-atom Pd decahedron. *Journal of Physics: Condensed Matter*, 21(14):144204, 2009. 23

[106] Y. Chushak and L. S. Bartell. Molecular dynamics simulations of the freezing of gold nanoparticles. *The European Physical Journal D-Atomic, Molecular, Optical and Plasma Physics*, 16(1):43–46, 2001. 23

[107] G. Opletal, C. A. Feigl, G. Grochola, I. K. Snook, and S. P. Russo. Elucidation of surface driven crystallization of icosahedral clusters. *Chemical Physics Letters*, 482 (4):281–286, 2009. 23

[108] F. Delogu. A numerical study of the freezing behavior of an unsupported nanometer-sized Au droplet. *Nanotechnology*, 18(48):485710, 2007. 23

[109] Y. H. Chui, I. K. Snook, and S. P. Russo. Visualization and analysis of structural ordering during crystallization of a gold nanoparticle. *Physical Review B*, 76(19): 195427, 2007. 23

[110] R. L. Schwoebel. Condensation of gold on gold single crystals. *Surface Science*, 2: 356–366, 1964. 24

[111] S. Ino. Epitaxial growth of metals on rocksalt faces cleaved in vacuum. II. Orientation and structure of gold particles formed in ultrahigh vacuum. *Journal of the Physical Society of Japan*, 21:346–362, 1966. 24

[112] S. Ino and S. Ogawa. Multiply twinned particles at earlier stages of gold film formation on alkalihalide crystals. *Journal of the Physical Society of Japan*, 22(6): 1365–1374, 1967. 24

[113] J. G. Allpress and J. V. Sanders. The structure and orientation of crystals in deposits of metals on mica. *Surface Science*, 7(1):1–25, 1967. 24

[114] Tsutomu K. Study on the structure of evaporated gold particles by means of a high resolution electron microscope. *Japanese Journal of Applied Physics*, 7(1):27–30, 1968. 24

[115] S. Ogawa and S. Ino. Formation of multiply-twinned particles in the nucleation stage of film growth. *Journal of Vacuum Science and Technology*, 6(4):527–534, 1969. 24

[116] S. Ogawa and S. Ino. Formation of multiply-twinned particles on alkali halide crystals by vacuum evaporation and their structures. *Journal of Crystal Growth*, 13:48–56, 1972. 24

[117] N. Uyeda, M. Nishino, and E. Suito. Nucleus interaction and fine structures of colloidal gold particles. *Journal of Colloid and Interface Science*, 43(2):264–276, 1973. 24

[118] C. Wayman. Nucleation and growth of gold films on graphite II. The effect of substrate temperature. *Journal of Crystal Growth*, 28:53–67, 1975. 24

[119] M. Gillet. Structure of small metallic particles. *Surface Science*, 67(1):139–157, 1977. 24

[120] K. Heinemann, M. J. Yacaman, C. Y. Yang, and H. Poppa. The structure of small, vapor-deposited particles: I. Experimental study of single crystals and particles with pentagonal profiles. *Journal of Crystal Growth*, 47(2):177–186, 1979. 24

[121] A. Renou and M. Gillet. Growth of Au, Pt and Pd particles in a flowing argon system: Observations of decahedral and icosahedral structures. *Surface Science*, 106(1):27–34, 1981. 24

[122] L. D. Marks. Modified wulff constructions for twinned particles. *Journal of Crystal Growth*, 61(3):556–566, 1983. 24, 106

[123] H. Hofmeister. Habit and internal structure of multiply twinned gold particles on silver bromide films. *Thin Solid Films*, 116(1):151–162, 1984. 24

[124] J. G. Pérez-Ramírez, M. Jose-Yacaman, A. Díaz-Pérez, and R. Berriel-Valdós. On the equilibrium shape of multiple-twinned particles. *Super Lattices and Microstructures*, 1(6):485–487, 1985. 24

[125] M. Flüeli, R. Spycher, P. A. Stadelmann, P. A. Buffat, and J. P. Borel. High-resolution electron microscopy (HREM) on icosahedral gold small particles: image simulation and observations. *EPL (Europhysics Letters)*, 6(4):349, 1988. 24

[126] P. Y. Gao, W. Kunath, H. Gleiter, and K. Weiss. *The structure of small penta-twinned gold particles*. Springer, 1989. 24

[127] M. Jose-Yacaman, R. Herrera, A. Gómez, S. Tehuacanero, and P. Schabes-Retchkiman. Decagonal and hexagonal structures in small gold particles. *Surface Science*, 237(1):248–256, 1990. 24

[128] A. R. Thölén. Electron microscope investigation of small particles. *Phase Transitions: A Multinational Journal*, 24(1):375–406, 1990. 24

[129] D. L. Lu, Y. Okawa, K. Suzuki, and K. Tanaka. The shape and structure of gold particles grown at different electrode potentials. *Surface Science*, 325(1):L397–L405, 1995. 24

[130] C. H. Gammons. Hydrothermal synthesis of gold grains with apparent five-fold symmetry. *Journal of the Mineralogical Association of Canada*, 34(3):1–8, 1996. 24

[131] D. L. Lu and K. Tanaka. Crystal habit of fcc metal particles controlled by electrode potential in solution. *Journal of Solid State Electrochemistry*, 1(3):187–193, 1997. 24, 25

[132] D. Zanchet, B. D. Hall, and D. Ugarte. Structure population in thiol-passivated gold nanoparticles. *The Journal of Physical Chemistry B*, 104(47):11013–11018, 2000. 24

[133] T. Oku and K. Hiraga. Atomic structures and stability of hexagonal BN, diamond and Au multiply-twinned nanoparticles with five-fold symmetry. *Diamond and Related Materials*, 10(3):1398–1403, 2001. 24

[134] S. A. Nepijko, H. Hofmeister, H. Sack-Kongehl, and R. Schlögl. Multiply twinned particles beyond the icosahedron. *Journal of Crystal Growth*, 213(1):129–134, 2000. 24

[135] K. Koga and K. Sugawara. Population statistics of gold nanoparticle morphologies: direct determination by HREM observations. *Surface Science*, 529(1):23–35, 2003. 24, 115, 119

[136] M. R Hormozi Nezhad, M. Aizawa, L. A. Porter, A. E. Ribbe, and J. M. Buriak. Synthesis and patterning of gold nanostructures on InP and GaAs via galvanic displacement. *Small*, 1(11):1076–1081, 2005. 24

[137] P. Jiang, J. J. Zhou, R. Li, Z. L. Wang, and S. S. Xie. Poly (vinyl pyrrolidone)-capped five-fold twinned gold particles with sizes from nanometres to micrometres. *Nanotechnology*, 17(14):3533, 2006. 24

[138] R. Esparza, G. Rosas, E. Valenzuela, S. Gamboa, U. Pal, and R. Pérez. Structural analysis and shape-dependent catalytic activity of Au, Pt and Au/Pt nanoparticles. *Revista Matéria*, 13(4):579–586, 2008. 24

[139] K. Kwon, K. Y. Lee, Y. W. Lee, M. Kim, J. Heo, S. J. Ahn, and S. W. Han. Controlled synthesis of icosahedral gold nanoparticles and their surface-enhanced raman scattering property. *The Journal of Physical Chemistry C*, 111(3):1161–1165, 2007. 24

[140] D. Seo, C. I. Yoo, I. S. Chung, S. M. Park, S. Ryu, and H. Song. Shape adjustment between multiply twinned and single-crystalline polyhedral gold nanocrystals: decahedra, icosahedra, and truncated tetrahedra. *The Journal of Physical Chemistry C*, 112(7):2469–2475, 2008. 24

[141] J. Xu, S. Li, J. Weng, X. Wang, Z. Zhou, K. Yang, M. Liu, X. Chen, Q. Cui, M. Cao, et al. Hydrothermal syntheses of gold nanocrystals: from icosahedral to its truncated form. *Advanced Functional Materials*, 18(2):277–284, 2008. 24

[142] Y. Q. Wang, W. S. Liang, and C. Y. Geng. Coalescence behavior of gold nanoparticles. *Nanoscale Research Letters*, 4(7):684–688, 2009. 24

[143] T. H. Lim, D. McCarthy, S. C. Hendy, K. J. Stevens, S. A. Brown, and R. D. Tilley. Real-time TEM and kinetic monte carlo studies of the coalescence of decahedral gold nanoparticles. *ACS Nano*, 3(11):3809–3813, 2009. 24

[144] Q. Zhang, J. Xie, Y. Yu, J. Yang, and J. Y. Lee. Tuning the crystallinity of Au nanoparticles. *Small*, 6(4):523–527, 2010. 24, 25, 125

[145] N. P. Young, M. A. van Huis, H. W. Zandbergen, H. Xu, and A. I. Kirkland. Transformations of gold nanoparticles investigated using variable temperature high-resolution transmission electron microscopy. *Ultramicroscopy*, 110(5):506–516, 2010. 24, 25, 26

[146] G. Casillas, J. J. Velázquez-Salazar, and M. Jose-Yacaman. A new mechanism of stabilisation of large decahedral nanoparticles. *The Journal of Physical Chemistry C*, 116(15):8844–8848, 2012. 24

[147] Z. W. Wang and R. E. Palmer. Determination of the ground-state atomic structures of size-selected Au nanoclusters by electron-beam-induced transformation. *Physical Review Letters*, 108(24):245502, 2012. 24, 25, 128, 145

[148] J. Smit, F. Ogburn, and C. J. Bechtoldt. Multiple twin structures in electrodeposited silver dendrites. *Journal of The Electrochemical Society*, 115(4):371–374, 1968. 23

[149] J. A. Ascencio, M. Mendoza, T. Santamaria, M. Perez, I. Nava, C. Gutierrez-Wing, and M. Jose-Yacaman. Structural instabilities in passivated gold nanoclusters induced by electron irradiation. *Journal of Cluster Science*, 13(2):189–197, 2002. 26

[150] Z. W. Wang and R. E. Palmer. Experimental evidence for fluctuating, chiral-type Au_{55} clusters by direct atomic imaging. *Nano Letters*, 12(11):5510–5514, 2012. 26

[151] Z. W. Wang and R. E. Palmer. Direct atomic imaging and dynamical fluctuations of the tetrahedral au20 cluster. *Nanoscale*, 2012. 26, 94

[152] D. B. Willliams and C. B. Carter. *Transmission Electron Microscopy*. Springer, 2009. 29, 31, 32, 33, 35, 36, 37, 40, 41, 42

[153] URL http://www.nobelprize.org/nobel_prizes/physics/laureates/1986/index.html. 30

[154] M. Von Ardenne. Das elektronen-rastermikroskop. *Zeitschrift für Physik A Hadrons and Nuclei*, 109(9):553–572, 1938. 30

[155] P. D. Nellist and S. J. Pennycook. Incoherent imaging using dynamically scattered coherent electrons. *Ultramicroscopy*, 78(1):111–124, 1999. 30

[156] J. C. Yang, M. W. Small, R. V. Grieshaber, and R. G. Nuzzo. Recent developments and applications of electron microscopy to heterogeneous catalysis. *Chemical Society Reviews*, 2012. 31

[157] O. Scherzer. Über einige fehler von elektronenlinsen. *Zeitschrift für Physik A Hadrons and Nuclei*, 101(9):593–603, 1936. 30

[158] O. Scherzer. Spharische und chromatische korrektur von elektronen-linsen. *Optik*, 2:114–132, 1947. 30

[159] A. R. Lupini, A. Y. Borisevich, J. C. Idrobo, H. M. Christen, M. Biegalski, and S. J. Pennycook. Characterizing the two-and three-dimensional resolution of an improved aberration-corrected STEM. *Microscopy and Microanalysis*, 15(5):441, 2009. 30

[160] M. Haider, S. Uhlemann, E. Schwan, H. Rose, B. Kabius, and K. Urban. Electron microscopy image enhanced. *Nature*, 392:768–769, 1998. 30

[161] A. Y. Borisevich, A. R. Lupini, and S. J. Pennycook. Depth sectioning with the aberration-corrected scanning transmission electron microscope. *Proceedings of the National Academy of Sciences of the United States of America*, 103(9):3044–3048, 2006. 30

[162] M. Haider, S. Uhlemann, and J. Zach. Upper limits for the residual aberrations of a high-resolution aberration-corrected STEM. *Ultramicroscopy*, 81(3):163–175, 2000. 39

[163] H. H. Rose. Optics of high-performance electron microscopes. *Science and Technology of Advanced Materials*, 9(1):014107, 2008. 39

[164] M. Haider, H. Rose, S. Uhlemann, E. Schwan, B. Kabius, and K. Urban. A spherical-aberration-corrected 200kv transmission electron microscope. *Ultramicroscopy*, 75 (1):53–60, 1998. 39

[165] D. S. He, Y. Han, J. Fennell, S. L. Horswell, and Z. Y. Li. Growth and stability of Pt on Au nanorods. *Applied Physics Letters*, 101(11):113102–113102, 2012. 41, 42, 129

[166] L. Reimer and M. Wächter. Contribution to the contamination problem in transmission electron microscopy. *Ultramicroscopy*, 3:169–174, 1978. 42

[167] M. Wendt. The role of contamination layers in electron probe microanalysis. *Kristall und Technik*, 15(12):1367–1375, 1980. 42

[168] N. Yoshimura, H. Hirano, and T. Etoh. Mechanism of contamination build-up induced by fine electron probe irradiation. *Vacuum*, 33(7):391–395, 1983. 42

[169] Z. L. Wang. Transmission electron microscopy of shape-controlled nanocrystals and their assemblies. *The Journal of Physical Chemistry B*, 104(6):1153–1175, 2000. 43, 44, 45, 46

[170] Z. L. Wang and J. Wiley. *Characterization of nanophase materials*. Wiley Online Library, 2000. 45

[171] D. Klenov and S. Stemmer. Contributions to the contrast in experimental high-angle annular dark-field images. *Ultramicroscopy*, 106(10):889–901, 2006. 48

[172] Z. W. Wang, Z. Y. Li, S. J. Park, A. Abdela, D. Tang, and R. E. Palmer. Quantitative z-contrast imaging in the scanning transmission electron microscope with size-selected clusters. *Physical Review B*, 84(7):073408, 2011. 48, 76

[173] P. D. Nellist and S. J. Pennycook. The principles and interpretation of annular dark-field z-contrast imaging. *Advances in Imaging and Electron Physics*, 113:147–203, 2000. 48, 49, 77

[174] D. E. Jesson and S. J. Pennycook. Incoherent imaging of crystals using thermally scattered electrons. *Proceedings of the Royal Society of London. Series A: Mathematical and Physical Sciences*, 449(1936):273–293, 1995. 48, 49

[175] P. Hartel, H. Rose, and C. Dinges. Conditions and reasons for incoherent imaging in STEM. *Ultramicroscopy*, 63(2):93–114, 1996. 49

[176] S. Kaneko, T. Nagano, K. Akiyama, T. Ito, M. Yasui, Y. Hirabayashi, H. Funakubo, and M. Yoshimoto. Large constriction of lattice constant in epitaxial magnesium oxide thin film: Effect of point defects on lattice constant. *Journal of Applied Physics*, 107(7):073523–073523, 2010. 54

[177] J. M. LeBeau and S. Stemmer. Experimental quantification of annular dark-field images in scanning transmission electron microscopy. *Ultramicroscopy*, 108(12): 1653–1658, 2008. 61

[178] S. D. Findlay and J. M. LeBeau. Detector non-uniformity in scanning transmission electron microscopy. *Ultramicroscopy*, 2012. 69

[179] S. Van Aert, A. De Backer, G. T. Martinez, B. Goris, S. Bals, G. Van Tendeloo, and A. Rosenauer. Procedure to count atoms with trustworthy single-atom sensitivity. *Physical Review B*, 87(6):064107, 2013. 72, 76, 85

[180] J. M. LeBeau, S. D. Findlay, L. J. Allen, and S. Stemmer. Standardless atom counting in scanning transmission electron microscopy. *Nano Letters*, 10(11):4405–4408, 2010. 72, 75, 76

[181] S. Van Aert, K. J. Batenburg, M. D. Rossell, R. Erni, and G. Van Tendeloo. Three-dimensional atomic imaging of crystalline nanoparticles. *Nature*, 470(7334):374–377, 2011. 73, 75

[182] Y. Han, D. S. He, and Z. Y. Li. Direct observation of dynamic events of Au clusters on mgo (100) by HAADF-STEM. *Journal of Nanoparticle Research*, 15(9):1–7, 2013. 73, 82, 87, 88

[183] Y. Han, D. S. He, Y. Liu, S. Xie, T. Tsukuda, and Z. Y. Li. Size and shape of nanoclusters: Single-shot imaging approach. *Small*, 8(15):2361–2364, 2012. 73, 90

[184] URL `rsb.info.nih.gov/ij/`. 74, 96

[185] J. M. LeBeau, S. D. Findlay, L. J. Allen, and S. Stemmer. Quantitative atomic resolution scanning transmission electron microscopy. *Physical Review Letters*, 100 (20):206101, 2008. 75

[186] S. Van Aert, J. Verbeeck, R. Erni, S. Bals, M. Luysberg, D. V. Dyck, and G. V. Tendeloo. Quantitative atomic resolution mapping using high-angle annular dark field scanning transmission electron microscopy. *Ultramicroscopy*, 109(10):1236–1244, 2009. 76, 77, 81, 85

[187] P. D. Nellist. Scanning transmission electron microscopy. In *Science of microscopy*, pages 65–132. Springer, 2007. 77

[188] M. Born and E. Wolf. *Principles of optics: electromagnetic theory of propagation, interference and diffraction of light*. CUP Archive, 1999. 77

[189] M. C. Scott, C. C. Chen, M. Mecklenburg, C. Zhu, R. Xu, P. Ercius, U. Dahmen, B. C. Regan, and J. Miao. Electron tomography at 2.4-angstrom resolution. *Nature*, 483(7390):444–447, 2012. 79

[190] C. Biernacki, G. Celeux, and G. Govaert. Assessing a mixture model for clustering with the integrated completed likelihood. *Pattern Analysis and Machine Intelligence, IEEE Transactions on*, 22(7):719–725, 2000. 84

[191] A. De Backer, G. T. Martinez, A. Rosenauer, and S. Van Aert. Atom counting in HAADF STEM using a statistical model-based approach: Methodology, possibilities, and inherent limitations. *Ultramicroscopy*, 134(0):23–33, 2013. 86

[192] E. J. Kirkland. *Advanced computing in electron microscopy*. Springer, 2010. 93

[193] C. Dwyer. Simulation of scanning transmission electron microscope images on desktop computers. *Ultramicroscopy*, 110(3):195–198, 2010. 93

[194] A. J. Logsdail, Z. Y. Li, and R. L. Johnston. Faceting preferences for Au_n and Pd_n nanoclusters with high-symmetry motifs. *Physical Chemistry Chemical Physics*, 15 (21):8392–8400, 2013. 95

[195] URL `http://jmol.sourceforge.net/`. 96

[196] D. J. Smith and L. D. Marks. High resolution studies of small particles of gold and silver: II. Single crystals, lamellar twins and polyparticles. *Journal of Crystal Growth*, 54(3):433–438, 1981. 96, 101

[197] URL http://inkscape.org/. 101

[198] A. Sánchez-Iglesias, I. Pastoriza-Santos, J. Pérez-Juste, B. Rodríguez-González, F. J. García de Abajo, and L. M. Liz-Marzán. Synthesis and optical properties of gold nanodecahedra with size control. *Advanced Materials*, 18(19):2529–2534, 2006. 115

[199] R. E. Palmer, S. Pratontep, and H.G. Boyen. Nanostructured surfaces from size-selected clusters. *Nature Materials*, 2(7):443–448, 2003. 116, 122

[200] B. Von Issendorff and R. E. Palmer. A new high transmission infinite range mass selector for cluster and nanoparticle beams. *Review of Scientific Instruments*, 70 (12):4497–4501, 1999. 117

[201] Z. H. Jin, S. T. Dunham, H. Gleiter, H. Hahn, and P. Gumbsch. A universal scaling of planar fault energy barriers in face-centered cubic metals. *Scripta Materialia*, 64 (7):605–608, 2011. 129

[202] R. F. Egerton, P. Li, and M. Malac. Radiation damage in the TEM and SEM. *Micron*, 35(6):399–409, 2004. 130, 133

[203] K. Iakoubovskii, K. Mitsuishi, Y. Nakayama, and K. Furuya. Mean free path of inelastic electron scattering in elemental solids and oxides using transmission electron microscopy: Atomic number dependent oscillatory behavior. *Physical Review B*, 77 (10):104102, 2008. 130

[204] R. F. Egerton. Electron energy-loss spectroscopy in the TEM. *Reports on Progress in Physics*, 72(1):016502, 2009. 130

[205] A. J. Bullen, K. E. Ohara, D. G. Cahill, O. Monteiro, and A. von Keudell. Thermal conductivity of amorphous carbon thin films. *Journal of Applied Physics*, 88(11): 6317–6320, 2000. 130

[206] J. Dundurs, L. D. Marks, and P. M. Ajayan. Structural fluctuations in small particles. *Philosophical Magazine A*, 57(4):605–620, 1988. 131, 144

[207] V. G. Gryaznov, A. M. Kaprelov, and A. Yu. Belov. Real temperature of nanoparticles in electron microscope beams. *Philosophical Magazine Letters*, 63(5):275–279, 1991. 131

[208] M. Morgan. Electrical conduction in amorphous carbon films. *Thin Solid Films*, 7 (5):313–323, 1971. 131

[209] S. Veprek, Z. Iqbal, R. Kuhne, P. Capezzuto, F. A. Sarott, and J. K. Gimzewski. Properties of microcrystalline silicon. IV. Electrical conductivity, electron spin resonance and the effect of gas adsorption. *Journal of Physics C: Solid State Physics*, 16(32):6241, 1983. 131

[210] URL http://www.ioffe.ru/SVA/NSM/Semicond/Si/. 131

[211] R. F. Egerton, R. McLeod, F. Wang, and M. Malac. Basic questions related to electron-induced sputtering in the TEM. *Ultramicroscopy*, 110(8):991–997, 2010. 131